Università degli studi di Genova

Doctoral thesis in Science and Technologies of Chemistry and Materials

Curriculum: Chemical Science and Technologies

Cycle XXXI

Nickel and Cobalt based catalysts in processes for production of useful compounds from renewables

Tullio Cavattoni

Tutor: Prof. Paola Riani

CoTutor Prof. Fabio Canepa

Index

Chapter 1

Materials and processes for Hydrogen production and CO_2 reuse

1.1 Introduction

The population increase and the consequent increased demand for energy and processes with high sustainability and efficiency occurred in the last decade are key factors for developing new energy production systems. In fact, according to the international Energy outlook 2016 (IEA2016[1]), the energy demand will increase for a 48% between 2012 and 2040, most of it produced through fossil fuels combustion (about 78% in 2014), similar trend will be followed from increase of greenhouse gases and pollutant emissions. With this in mind, researching for renewable energy sources is considered necessary.

Hydrogen is recognized among most as a promising energy vector, in fact H_2 has a high energy storage capacity (120.7 kJ/mol [2]), no environment impact factor for its use, since its combustion product is only water, and the possibility to be used in fuel cells for electricity production. Nowadays hydrogen plays a very important role in industrial chemistry: it is involved in the 48% of industry production, in particular in ammonia and methanol synthesis. H_2 is further used in fuel hydrotreating units in refinery processes (hydrodesulfurisation, hydrocracking). Pure H_2 is required for hydrogenation of oils, hydrocarbons, aldehydes, ketones and production of cosmetics, soaps and vitamins. Beside the industrial demand, since the interest in use hydrogen for automotive and stationary purpose, an increased volume of hydrogen production will be required. According to this, it is needed to consider the safety issues related to its use. A solution to this kind of problem could be the use of hydromethane, a mixture of hydrogen and methane, that reduces safety issues almost to the same as the methane, and allows the use of the same engines with just little modifications. Otherwise hydrogen can be used to prepare methane itself, starting from stored CO_2, obtaining clean methane and reducing the amount of CO_2 emission. Currently, hydrogen is mainly produced through catalytic steam reforming of hydrocarbon: natural gas is the preferred source, due to its abundance and low price. Catalytic steam reforming of natural gas giving rise to about 48% of the hydrogen production. The rest of technologies based on non-renewable sources for the production of hydrogen, includes the partial oxidation, steam reforming of oil fractions (30%), and coal gasification (18%). The only technique using a renewable source is water electrolysis, amounting to

only 4% of hydrogen production and yet, being an expensive process, and only 20% of it is actually renewable [3, 4].

The development of technologies for renewable hydrogen production starting from biomasses would allow a series of evident advantages such as the development of carbon neutral processes and the use of widespread available source both as virgin (grass, trees, shrubs, algae and aquatic plants) or residuals (forest residuals, agricultural, municipal and industrial wastes) [5, 6].

To increase the production of hydrogen from renewable sources, biohydrogen or renewable hydrogen, different approaches are under investigation, in order to reduce GHG (greenhouse gases) production and decrease the energy production from fossil fuels. A summary of those technologies will be shown below [7, 8]:

1) Thermochemical technologies: i.e. all the processes involving thermal production of hydrogen from different renewable sources. Most important processes belonging to this category are: steam reforming, partial oxidation, gasification and pyrolysis of biomass or biomass derived intermediates [9].
2) Electrochemical technologies: production of hydrogen due to electrochemical splitting of the water

$$2H_2O = 2H_2 + O_2$$

This reaction takes place at the two electrodes of a electrolysis cell, and its limit is due to the energy required for the system, so it is convenient only if low price electricity is available.

3) Photo-biological technologies: one of the latest and less developed techniques is to use bacteria and green algae in order to exploit their photosynthesis for the hydrogen production, bio-photolysis, photo-fermentation and dark-fermentation are the most worthy to be mentioned among these technologies.
4) Photo-electrochemical technologies: similar to the electrochemical techniques, but in this case the energy for the water splitting is due to the sunlight; also these techniques are immature and require an improvement in H_2 yield.

In the following part, I will give a deeper explanation of the processes that are important for this thesis.

1.2) steam reforming of renewables

Steam reforming is an endothermic catalytic process in which a carbon feedstock reacts with steam, over a base metal or noble one, producing gas containing mainly CO, CO_2 and H_2 (Syngas), following this reaction stoichiometry

$$C_nH_mO_y + (n-y)H_2O \rightleftarrows nCO + (n-y+m/2)H_2$$

coupled with water gas shift reaction (WGS):

$$CO + H_2O \rightleftarrows CO_2 + H_2$$

and with dry reforming:

$$C_nH_mO_y + (n-y)CO_2 \rightleftarrows (2n-y)CO + (m/2)H_2$$

Today, Steam Reforming processes are well-established technologies for the production of H_2 from fossil fuels at industrial scale.

Methane and natural gas steam reforming, nowadays the most used process, are based on Ni catalysts supported on alumina based carrier, stabilized by alkali or alkali earth cations, performing the reaction at a process temperature comprised between 1000 and 1200K. These processes present a good H_2/CO product ratio that makes it the best technology available among the thermochemical processes (Fig. 1.1).

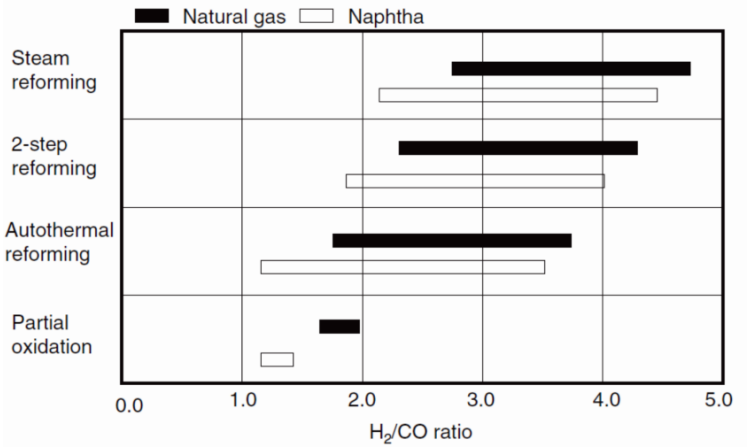

Fig.1.1: H_2/CO ratio achievable by different technologies starting by naphtha and Natural gases carbon feedstocks [10]

In order to find the best catalytic composition for the Steam Reforming process, many studies have been carried out on different carbon feedstocks, methanol, bioethanol, acetic acid, glycerol, C_2-C_4 hydrocarbons, bio-oil.

For each mentioned feedstock, there is a proper catalytic active phase, which preparation and testing inspired several studies, increasing the literature on this field during the last decades.

There are still many undergoing studies in order to offer the best H_2/CO ratio, enhance the process condition and diminish the costs; in fact the best catalytic formulations and conditions are not yet achieved.

The development of high performance catalysts, increasing their resistance to deactivation, poisoning and sintering is another topic of interest in this field.

The most interesting process for this thesis is the Ethanol Steam Reforming (ESR).

Ethanol, in fact, is very attractive for hydrogen production starting from a renewable source thanks to the following features. It has a good hydrogen content, it is widely available, it is non toxic, easy to carry, storage and handle, it can be produced renewably by fermentation of biomasses, it is a clean fuel and, lately, it doesn't contain hard abatement pollutants, like Sulphur and heavy metals.

In this process, the catalyst needs to be able to cleave the C-C bonding in presence of steam, forming syngas.

This reaction is endothermic and occurs at a temperature above 573K. At this temperature the main reaction is:

$$C_2H_5OH_g + H_2O_g \rightleftarrows 2CO_g + 4H_{2g} \qquad \Delta H_0^{298K} = +255.5 \text{ kJ/mol}$$

Also in this case, the WGS reaction may occur:

$$CO_g + H_2O_g \rightleftarrows CO_{2g} + H_{2g} \qquad \Delta H_0^{298K} = -41.6 \text{ kJ/mol}$$

Producing a syngas containing CO, CO_2 and H_2.

If the WGS equilibrium is shifted to right, i.e. completing this slightly exothermic reaction at low temperature the complete conversion of ethanol to CO_2 could be obtained:

$$C_2H_5OH_g + 3H_2O_g \rightleftarrows 2CO_{2g} + 6H_{2g} \qquad \Delta H_0^{298K} = +173{,}3 \text{ kJ/mol.}$$

Following strictly the stoichiometry, at least 3 moles of water/mole of ethanol are required, which corresponds to a steam to carbon ratio of 1.5. However, to reduce carbon formation and to push

the equilibrium to right, a water excess is usually used such as e.g. a steam to carbon ratio of 6. The syngas obtained needs a series of purification steps, due the presence of different contaminants [11].

The reaction pathway of ethanol steam reforming, widely studied in the last decades, is complex, several secondary reactions could occur, depending on reaction conditions, among which: ethanol dehydrogenation to acetaldehyde, ethanol dehydration to ethylene, ethanol conversion to acetone; all of these are possible byproducts. The reactions are reported in the following Table 1.1 [12].

Reaction	Equation
Sufficient steam supply	$C_2H_5OH + 3H_2O \rightarrow 2CO_2 + 6H_2$
Insufficient steam supply	$C_2H_5OH + H_2O \rightarrow 2CO + 4H_2$
	$C_2H_5OH + 2H_2 \rightarrow 2CH_4 + H_2O$
Dehydrogenation	$C_2H_5OH \rightarrow C_2H_4O + H_2$
Acetaldehyde decomposition	$C_2H_4O \rightarrow CH_4 + CO$
Acetaldehyde steam reforming	$C_2H_4O + H_2O \rightarrow 3H_2 + 2CO$
Dehydration	$C_2H_5OH \rightarrow C_2H_4 + H_2O$
Coke formation	$C_2H_4 \rightarrow$ polymeric deposits (coke)
Decomposition	$C_2H_5OH \rightarrow CO + CH_4 + H_2$
	$2C_2H_5OH \rightarrow C_3H_6O + CO + 3H_2$
	$C_2H_5OH \rightarrow 0.5CO_2 + 1.5CH_4$
Reaction of decomposition products	
Methanation	$CO + 3H_2 \rightarrow CH_4 + H_2O$
	$CO_2 + 4H_2 \rightarrow CH_4 + 2H_2O$
Methane decomposition	$CH_4 \rightarrow 2H_2 + C$
Boudouard reaction	$2CO \rightarrow CO_2 + C$
Water gas shift reaction (WGSR)	$CO + H_2O \rightarrow CO_2 + H_2$

Table 1.1

Nowadays a high number of investigations are currently being undertaken to discover effective catalysts, to understand the reaction mechanism, and to develop industrial or pilot scale processes for ethanol steam reforming. As said, the best composition for catalysts for ESR, as well as the best conditions to perform the process, have not been reached yet. Nowadays the most used catalysts for the processes discussed above are the Pt group elements. Noble metals are well known for their high activity and have been extensively studied. The catalytic performance of supported noble metals (Ru, Rh, Pd, Pt, Ir, Au) catalysts for the ESR has been investigated in the temperature range of 600-850°C depending on the metal, support (usually Al_2O_3, MgO, TiO_2) and metal loading. Many

authors used Rh, Pd and Pt with different supports such as alumina and ceria or zirconia. The noble metal activity decreases following this order, using the same support: Rh > Pt > Pd. Also the catalyst stability was monitored. Rhodium supported on alumina is actually used in many industrial processes. The reaction is carried out at temperatures between 50 and 650°C with water /ethanol ratio of 4.2-8.4, with or without the addition of O_2 for autothermal process. Methane in this case is one of the main products whose selectivity decrease with contact time. Compared to other noble metals, with this support, Rh appears to be the most active one, and a further increase in activity is obtained doping the catalyst with Ni or Ru. Moreover, the catalytic performance of MgO-supported Pd, Rh, Ni and Co for ESR t has been widely evaluated.

Rh/MgO showed the best conversion and stability at 650°C, while Ni exhibited the best selectivity to H_2 (>95%). The other metals, Pd, Ru and Ir, even if active for this process are not studied as much as Ru, due to their lower activity in ESR. Moreover, the high cost of noble metals is the major limiting factor in their use for hydrogen production via steam reforming. Therefore, many studies are ongoing on non-noble metals. Transition metals represent a main family of heterogeneous catalysts, largely applied for both hydrogenations and oxidations processes [13]. Most of the metallic catalysts are supported [14]: in fact, carriers such as high-surface area metal oxides or carbon materials allow stabilizing metals in the form of very active and stable nanoparticles [15]. Unsupported metals are used, such as iron for ammonia synthesis and for the Fischer Trøpsch reaction, Nickel Raney for hydrogenations, etc. These materials are in the form of relatively large porous particles and contain impurities that actually activate and stabilize them. Recent studies report on the application in catalysis of metal nanoparticles [16], i.e. unsupported metal particles with a size of 1-100 nm [17], predominantly based on noble metals [18, 19, 20]. Even more recently, bimetallic nanoparticles have also been investigated for catalysis: most of these studies are devoted again to bimetallic alloys of noble metals [21, 22], usually applied in low temperature applications and in particular to liquid phase reactions [23]. Bimetallic nanoparticles are frequently reported to be more active than monometallic ones [24].

1.3 CO_2 hydrogenation

The hydrogenation of CO_2 to methane is a possible way to reuse captured CO_2, thus reducing the emission of greenhouse gases by recycling carbon dioxide [25, 26]. The use of hydrogen produced by water electrolysis using photovoltaic electricity production, or in any case the use of “renewable”

hydrogen allows one to realize the "Power-to-Gas" (PtG) technology in a sustainable way [27, 28]. The produced methane, sometimes denominated as Synthetic or Substitute Natural Gas (SNG) [29], can be used as a green fuel and injected into existing natural gas pipeline networks. Through CO_2 methanation, "hydromethane", that is a H_2-CH_4 mixture, a potentially interesting fuel for automotive purposes [30], can be synthesized.

CO produced by the reverse water gas shift reaction (r-WGS) is an unwanted by-product from CO_2 methanation. Taking into account that methanation is an exothermic equilibrium reaction, catalysts for an efficient process must be active at low temperature, very selective and stable in practical conditions. Most of transition metals (such as nickel, cobalt and iron), and platinum group metals are active for both CO and CO_2 methanation reaction. However, the catalysts choice, for both CO_2 and CO methanation reaction, is usually restricted to ruthenium and nickel.

Ruthenium is more active, especially at low temperatures, and very selective to CH_4 starting from CO_2 [31, 32, 33].

Nickel is usually less active than Ruthenium, but can also give rise to high selectivities to CH_4, depending on nickel loading [34]. Moreover, nickel is much cheaper than Ru, allowing using much higher metal loadings.

As for the supports, γ-Al_2O_3 is a widely produced and used material [35, 36], with high dispersing properties towards metals, thus giving rise to active and stable metal hydrogenation catalysts [37, 38]. In fact, commercial catalysts for the already well-established CO methanation process in the purification of hydrogen (that is for low concentration CO_x feeds) are based on either 0.3% Ru/γ-Al_2O_3 (low temperature catalysts) or $\sim$ 20% Ni/γ-Al_2O_3 (high temperature catalysts) [39]. However, catalysts for SNG production, thus using concentrated feeds, may work at high temperatures. The use of a 22wt% Ni catalyst on a stabilized support, with a surface area decreasing from 50 m^2/g (fresh) to 30 m^2/g (used) has been reported [40]. In spite of the higher activity of Ru catalysts, according to Fechete and Vedrine [41], Ni/Al_2O_3 is the best known catalyst for industrial CO_2 methanation applications worldwide and it has been commercialized by Evonik, Johnson Matthey, Topsøe, and Clariant-Süd Chemie.

1.4 Supported, unsupported and mechanically supported catalysts

Transition metals find large application as heterogeneous catalysts for a number of reactions such as hydrogenations, partial and total oxidations [26]. In most cases, metals are supported on, metal

oxides [42]. Supported metal catalysts are mostly produced by impregnation or deposition/precipitation processes; this process includes: the metal precursor salts addiction to the preformed support, then their decomposition to an oxide, followed by its reduction to obtain the metal. Supporting metals might allow to produce very active nanoparticles stabilized towards sintering and somehow activated by the interaction with the support [43] and, maybe, to reduce the amount of the metal used (an important effect in using precious metals).

However, unsupported transition metal based nanoparticles, i.e. unsupported metal particles with a size of 1-100 nm [44], have also been found to act as promising materials for heterogeneous catalytic processes [45, 46]. Most of these works have been devoted to precious metal nanoparticles such as gold [47], palladium [48] and platinum [49], which display very high activity. Although unsupported Cobalt nanoparticles (CoNPs) are of interest in several fields [50, 51], few studies are reported concerning the potential application of CoNPs in catalysis, mostly applied in low-temperature liquid-phase reactions [52, 53, 54]. In fact, the thermal stability of unsupported metal nanoparticles is generally poor, their applicability being usually limited to liquid-phase reactions performed at low temperature; alternatively, they may be essentially regarded as model catalysts, whose activity is limited to short time-on-stream experiments. On the other hand, the application of unsupported metal nanoparticles as catalysts in gas-phase reactions may also arise technical and engineering issues (e.g. stability of the bed).

Few attempts have been reported on the stabilization of pre-synthesized metal nanoparticles without losing their strong activity by mechanically supporting them [55, 56]. This procedure could result in materials whose behaviour is different from that of conventionally prepared supported metal catalysts.

On the other hand, the nature of the interactions of nanoparticles with the support are not fully clear, and they are still object of investigation [57, 58]. The real structure of the interface between the nanoparticle surface and the support surface may even strongly depend on the preparation method.

1.5 Objective of this thesis

As said before, the best formulations of both catalysts and reaction conditions are not yet known for the two described processes. In fact, there are many factors that can be enhanced, for the

process itself: lowering process temperature, increasing conversion and selectivity to the desired product; for the catalysts: decreasing the production cost, the environmental impact and the risk of poisoning, due to coke deposition or sintering, enhancing its stability exposed to the reaction conditions. With these targets in mind, this thesis is focused on the study of Nickel and Cobalt catalysts, in different formulations, for the production of renewable hydrogen and for hydrogenation of CO_2.

In particular:

- (Co,Ni) nanoparticles catalysts for ESR
- Cobalt nanoparticles catalysts for ESR and CO_2 hydrogenation
- Cobalt supported on Silica catalysts for ESR and CO_2 hydrogenation
- Nickel doped with La_2O_3 supported on different supports catalysts for CO_2 hydrogenation

All the synthesis and morphological and structural characterization of all the samples that will be described in this thesis have been performed at the Dipartimento di Chimica e Chimica Industriale (DCCI) of the Università degli studi di Genova, under the supervision of prof. Paola Riani and prof. Fabio Canepa. The corresponding catalytic tests and the spectroscopic characterization have been carried out at Dipartimento di Ingegneria Civile, Chimica e Ambientale (DICCA) of the Università degli studi di Genova, under the supervision of prof. Guido Busca and Dr. Ing. Gabriella Garbarino.

1.6 References

[1] International Energy Outlook (2016), web site: https://www.eia.gov/forecasts/ieo/pdf/0484(2016).pdf (accessed on 20/09/2016).

[2] Haryanto A, Fernando S, Murali N, Adhikari S (2005) Current status of hydrogen production techniques by steam reforming of ethanol: a review. Energy Fuels 19:2098–2106.

[3] Energy Technology Perspectives (2012), web site: https://www.iea.org/publications/freepublications/publication/ETP2012_free.pdf.

[4] Armaroli N, Balzani V (2011) The hydrogen issue. ChemSusChem. 4:21-38.

[5] Kirkels AF, Verbong GPJ (2011) Biomass gasification: still promising? A 30-year global overview. Renew Sustain Energy Rev 15:471–481.

[6] Kumar A, Jones DD, Milford A. Hanna MA (2009) Energies Thermochemical Biomass Gasification: A Review of the Current Status of the Technology 2:556-581; doi:10.3390/en20300556

[7] E.Kırtay, Energy Conv. Manag. 2011, 52, 1778–1789

[8] M. Balat, Int. Journal of .Hydr. En., 2008, 33, 4013-4029

[9] G.W. Huber, S. Iborra, and A. Corma Chem. Rev., 2006, 106, 4044-4098

[10] J.R. Røstrup-Nielsen, J. Sehested, J.K. Norskov, Advan. Catal., 2002, 47,66–139

[11] Cavattoni ,T.; Garbarino, G.; Catalytic abatement of biomass tar: a technological perspective of Ni-based catalysts, Rendiconti Lincei 2017, 28; 68-85;

[12] M. Ni, D.Y.C Leung, M.K.H Leung., Int. J. Hydrogen Energy, 2007,32, 3238-3247.

[13] G. Busca, 2014, Heterogeneous Catalytic Materials, Elsevier, 297-344.

[14] J.A. Anderson, M. Fernández García eds., Supported Metals in Catalysis, 2nd Edition, 2011 World Scientific.

[15] M. Ahmadi, H. Mistry, B. Roldan Cuenya, Tailoring the Catalytic Properties of Metal Nanoparticles via Support Interactions, Phys. Chem. Lett. 7 (2016) 3519-3533.

[16] F. Tao, Metal Nanoparticles for Catalysis: Advances and Applications, ed. Royal Society of Chemistry, 2014

[17] European commission, Commission Recommendation of 18 October 2011 on the definition of nanomaterial, http://eur-lex.europa.eu/LexUriServ/LexUriServ.do?uri=OJ:L:2011:275:0038:0040:en:PDF

[18] Y. Mikami, A. Dhakshinamoorthy, M. Alvaro, H. García, Catal. Sci. Technol. 3 (2013) 58-69.

[19] B.C. Ranu, K. Chattopadhyay, L. Adak, A. Saha, S. Bhadra, R. Dey, D. Saha, Pure Appl. Chem. 81 (2009) 2337-2354.

[20] S. Alayoglu, C. Aliaga, C. Sprung, G.A. Samorjai, Catal. Lett. 141 (2011) 914-924.

[21] S. Alayoglu, A. U. Nilekar, M. Mavrikakis, B. Eichhorn, Nat. Mater. 7 (2008) 333–338.

[22] K. D. Gilroy, A. Ruditskiy, H. -C. Peng, D. Qin, Y. Xia, Chem. Rev. 116 (2016) 10414–10472.

[23] T. Dang-Bao, D. Pla, I. Favier, M. Gómez, Catalysts 7 (2017) 207.

[24] H. Lee, J. Lim, C. Lee, S. Back, K. An, J. Won Shin, R. Ryoo, Y. Jung, J. Young Park, Nat. Commun. 9 (2018) 2235.

[25] W. Wang, J. Gong, Front. Chem. Sci. Eng. 5 (2011) 2-10.

[26] G. Centi, S. Perathoner, Catal. Today 148 (2009)191–205.

[27] M. Götz, J. Lefebvre, F. Mörs, A. McDaniel Koch, F. Graf, S. Bajohr, et al., Renew. Energy. 85 (2016) 1371–1390.

[28] M. Bailera, P. Lisbona, L. M. Romeo, S. Espatolero, Renew. Sust. Energy Rev. 69 (2017) 292–312.

[29] T.J. Schildhauer, S.M.A. Biolla, eds., Synthetic Natural Gas: From Coal, Dry Biomass, and Power-to-Gas Applications, Wiley, 2016.

[30] D. Bellotti, M. Rivarolo, L. Magistri, A. F. Massardo, Int. J. Hydrogen Energy, 40 (2015) 2433-2444.

[31] M. S.Duyar, A. Ramachandran, C. Wang, R. J. Farrauto, J. CO_2 Utilization 12 (2015) 27-33.

[32] X. Wang, Y.Hong, H. Shi, J. Szanyi, J. Catal. 343 (2016) 185–195.

[33] L. Falbo, M. Martinelli, C. G.Visconti, L. Lietti, C. Bassano, P. Deiana, Appl. Catal. B: Environ. 225 (2018) 354-363.

[34] G. Garbarino, P. Riani, L. Magistri, G. Busca, Int. J. Hydrogen Energy 39 (2014) 11557-11565.

[35] G. Busca, Catal. Today 226 (2014) 2-13.

[36] G. Busca, Advan. Catal. 57 (2014) 319-404.

[37] G. Busca, Heterogeneous Catalytic Materials, Elsevier, 2014, pp. 318-321.

[38] S. Qi, X. Yong Wei, Z. Zong, Y. Wang, RSC Adv., 3 (2013) 14219–14232.

[39] Clariant, Catalysts for syngas, available on internet.

[40] Røstrup-Nielsen JR, Pedersen K, Sehested J, , Appl. Catal. A: Gen. (2007) 330 134-138.

[41] I. Fechete, J.C. Vedrine, B. Sels, M. Van de Voorde, eds., in Nanotechnology in Catalysis: Applications in the Chemical Industry, Energy Development and Environmental protection, Wiley, 2017, pp. 57-90.

[42] Anderson JA, Fernández García M eds., Supported Metals in Catalysis, 2nd Edition, 2011 World Scientific.

[43] Ahmadi M, Mistry H, Roldan Cuenya B, Tailoring the Catalytic Properties of Metal Nanoparticles via Support Interactions, *Phys Chem Lett* **7**:3519-3533 (2016).

[44] European Commission, Commission Recommendation of 18 October 2011 on the definition of nanomaterial; web site: http://eur-lex.europa.eu/LexUriServ/LexUriServ.do?uri=OJ:L:2011:275:0038:0040:en:PDF

[45] Burda C, Chen X, Narayanan R, El-Sayed ME, Chemistry and Properties of Nanocrystals of Different Shapes, *Chem Rev* **105**:1025-1102 (2005).

[46] Tao F, Metal Nanoparticles for Catalysis: Advances and Applications, ed. Royal Society of Chemistry 2014.

[47] Mikami Y, Dhakshinamoorthy A, Alvaro M, García H, Catalytic activity of unsupported gold nanoparticles, *Catal Sci Technol* **3**:58-69 (2013).

[48] Ranu BC, Chattopadhyay K, Adak L, Saha A, Bhadra S, Dey R, Saha D, Metal nanoparticles as efficient catalysts for organic reactions, *Pure Appl Chem* **81**:2337-2354 (2009).

[49] Alayoglu S, Aliaga C, Sprung C, Samorjai GA, Size and shape dependence on Pt nanoparticles for the methylcyclopentane/hydrogen ring opening/ring enlargement reaction, *Catal Lett* **141**:914-924 (2011).

[50] Yang, HT, Su, YK, Shen, CM, Yang TZ, Gao HJ, Synthesis and magnetic properties of e-Cobalt nanoparticles, *Surf Interface Anal* **36**:155-160 (2004).

[51] Ansari SM, Bhor RD, Pai KR, Sen D, Mazumder S, Ghosh K, Kolekar YD, Raman CV, Cobalt nanoparticles for biomedical applications: Facile synthesis, physiochemical characterization, cytotoxicity behavior and biocompatibility, *Appl Surf Sci* **414**:171-87 (2017).

[52] Muller JL, Klankermayer J, Leitner W, Poly(ethylene glycol) stabilized Co nanoparticles as highly active and selective catalysts for the Pauson–Khand reaction, *Chem Commun* **19**:1939-1941 (2007).

[53] Mondal A, Adhikary B, Mukherjee DK, Room-temperature synthesis of air stable Cobalt nanoparticles and their use as catalyst for methyl orange dye degradation, *Coll Surf A Physicochem Eng Asp* **482**:248–256 (2015).

[54] Mondal A, Mukherjee DK, Adhikary B, Ahmed MA, Cobalt nanoparticles as recyclable catalyst for aerobic oxidation of alcohols in liquid phase, *J Nanopart Res* **18**:117 (2016).

[55] Ribeiro RU, Liberatori JWC, Winnishofer H, Bueno JMC, Zanchet D, Colloidal Co nanoparticles supported on SiO2: synthesis, characterization and catalytic properties for steam reforming of ethanol, *Appl Catal B Environ* **91**:670–678 (2009).

[56] Jia CJ, Schüth F, Colloidal metal nanoparticles as a component of designed catalyst, *Phys Chem Chem Phys* **13**:2457-2487 (2011).

[57] Matsubu JC, Zhang S, DeRita L, Marinkovic NS, Chen JG, Graham GW, Pan X, Christopher P, Adsorbate-mediated strong metal-support interactions in oxide-supported Rh catalysts, *Nature Chem* **9**:120-127 (2017).

[58] Tang H, Su Y, Zhang B, Lee AF, Isaacs MA, Wilson K, Li L, Ren Y, Huang J, Haruta M, Qiao B, Liu X, Jin C, Su D, Wang J, Zhang T, Classical strong metal-support interactions between gold nanoparticles and titanium dioxide, *Science Adv* **3**:e1700231 (2017).

Chapter 2

Materials and Methodologies

2.1 Catalysts Preparation

The catalysts used for this thesis were prepared following different methods well known in literature.

Wet impregnation and incipient wet impregnation have been used for the supported catalysts, metal nanoparticles catalysts were instead prepared via reduction method in aqueous solution or by thermal decomposition of an appropriate precursor.

Some other catalysts used were commercial.

The choice of the support had a relevant importance in the preparation and on the behavior of the different catalysts. The supports used, commercially available, all produced by Sasol, are: different types of Siralox, an alumina with different percentage of Silica, and Puralox (pure γ-Al_2O_3). Further details on catalysts preparation will be given in the following paragraphs.

2.2 Supported Catalysts

2.2.1 Wet impregnation technique

Wet impregnation is one of the most used techniques for the preparation of supported metals oxides.

A solution of salts of the chosen metal precursor is placed in contact with the support, and then it is dried, in order to eliminate water and allow the crystallization of the precursor on and inside the support.

Finally a calcination step is required in order to oxidize the metal precursor in the final structure.

Supported Co-based catalysts have been prepared following this way using $Co(CH_3COO)_2 \cdot 4H_2O$, $CoCl_2 \cdot 6H_2O$ and $Co(NO_3)_3 \cdot 6H_2O$ as precursor salts. Siralox 5/170, previously calcined at 773 K for 5h, produced by Sasol, containing 95% Alumina and 5% SiO_2 has been used as support for this catalysts.

Solution of the salts were prepared and added to the support, then dried for 24h at 363 K. After this step, the mixtures were calcined for 5 hours at 773 K.

2.2.2 Incipient wet impregnation technique

Incipient wet impregnation has a different approach respect to the wet impregnation technique. In this case, in fact, the solution containing the precursor salt has the same volume, or slightly less, than the pore volume of the support. With this technique different Ni-and Co- based catalysts with different La_2O_3 loadings and on different supports have been prepared. The chosen supports have been calcined at 1023 K for 5h. Then a solution of the salt have been prepared and added dropwise to the support. The so obtained mixture were then dried 12h at 363 K, and calcined at 1023K for 5h.

2.3 Unsupported metal nanoparticles

Co and (Co,Ni) nanoparticles were prepared via reduction in aqueous solution, using different precursor salts. Co nanoparticles were also prepared by thermal decomposition of $Co_2(CO)_8$. For the monometallic particles, $CoCl_2 \cdot 6H_2O$ and $Co(NO_3)_3 \cdot 6H_2O$, were used as different precursor salts, while for bimetallic nanoparticles both $CoCl_2 \cdot 6H_2O$ and $NiCl_2 \cdot 6H_2O$ were used as precursor salts; in all cases $NaBH_4$ have been used as reducing agent. Different procedures were followed to separate and purify the nanoparticles. This step have a key role for the morphology and the activity of the nanoparticles and will be discussed with more details in the experimental paragraphs of the related chapters.

2.4 Material Characterization

Different techniques were used to characterize both fresh and after catalysis samples. In this section the adopted conditions, will be briefly listed, while the techniques used will be briefly described in the Appendix.

Before crystallographic investigation, unsupported Me NPs samples were usually annealed at 500°C for 3 hours under inert atmosphere, in order to increase the samples crystallinity.

X-ray diffraction patterns were carried out on samples by using a vertical powder diffractometer X'Pert with Cu Kα radiation (λ= 0.15406 nm). Patterns were usually collected in 20-100° 2θrange with a step of 0.02° and a counting time for each step of at least 16s. Powder patterns were indexed by comparing experimental results to the data reported in the Pearson's Crystal Data database [1].

FT-IR spectra were registered with a Nexus Thermo Fisher instrument with 100 scans and spectra resolution of 2 cm^{-1}. KBr pressed disks were used for skeletal characterization with a 1 wt.% catalyst and a disk total weight of 1.00 g. Pure powder pressed disks were used for surface characterization. The disks were previously activated by outgassing at 773 K for 1 h. After activation, 50 Torr of CO_2 (SIAD, 99.99% grade) was introduced into the cell. After 10 min, brief outgassing at room temperature was realized and IR spectra recorded.

Ultraviolet, Visible and Near Infrared Spectroscopy analysis were conducted with a Jasco V-570 that operates in diffuse reflectance basing on a $BaSO_4$ baseline. The sample preparation were carried out milling the catalysts in a mortar, pressing the powder in the sample holder, obtaining a self sustained disk. The collected signal acquired in absorbance range scale is converted in Kubelka-Munk units.

DC magnetization was performed in a dc-Superconducting Quantum Interference Device (SQUID) magnometer (MPMS-Magnetic Properties Measurement System, Quantum Design) with resolution better than 10^{-6} emu (RSO option). The room temperature magnetic hysteresis cycle was obtained in the 0-50Tesla μ0H magnetic field range.

Scanning Electron Microscopic analyses were performed by the SEM ZEISS SUPRA 40 VP, with a field emission gun. This instrument is equipped with a high sensitivity "InLens" secondary electrons detector and with a EDX microanalysis OXFORD "INCA Energie 450x3". For SEM analysis, unsupported metallic nanoparticles, were suspended in ethanol and exposed to ultrasonic vibrations to decrease the aggregation; a drop of the resultant mixture was finally deposed on a Lacey Carbon copper grid. On the contrary, supported catalysts (powders) were directly mounted on a high purity conductive double sided adhesive carbon tabs, and the specimen so obtained was then imaged and analyzed

Surface area measurements were performed in a Micromeritics Autochem 2920 with a single point measurement. The samples were pretreated in He at 523 K in order to desorb or decompose potentially adsorbed surface species.

Temperature Programmed Reduction with H_2 (H_2-TPR) was used to identify and evaluate the reducibility of the various nickel species present on the alumina-supported catalysts. In a typical H_2-TPR test, the as-calcined catalyst was reduced by a 10% H_2/Ar gas mixture, while the temperature was increased from RT to 1173K at a rate of 15 K/min.

X-ray photoelectron spectroscopy (XPS) was conducted by using the Thermo Scientific monochromatic Al K-alpha line (1.4866 keV) as the excitation source. Binding energies were measured on a multi-channel detector with pass energy of 50 eV and energy step of 0.05 eV for high-resolution scans and 0.5 eV for survey scans. Spectral regions are Ni2p, Al2p and La3d. All the spectra were referenced to the elemental carbon at binding energy (BE) of 284.8 eV. Quantification of surface components was based on the peak fitting and normalization of Ni (2p 3/2), La (3d 5/2), and Al (2p) primary peaks.

2.5 Catalytic Characterization

During this Ph.D. work, two different processes were studied. Steam Reforming and Carbon dioxide hydrogenation. The tests were carried out mainly in temperature ramp in order to evaluate the catalysts activity during the processes. Another test that should be performed is on the catalysts stability, that is for sure one of the interesting parameters when working in steady state conditions and might be further developed in future works.

In this paragraph, the experimental setup of both the line will be shown.

2.5.1 Ethanol Steam Reforming (ESR) and Methane Steam Reforming (MSR)

For this process have been used the gas-solid catalytic line shown in the followed Fig. 2.1

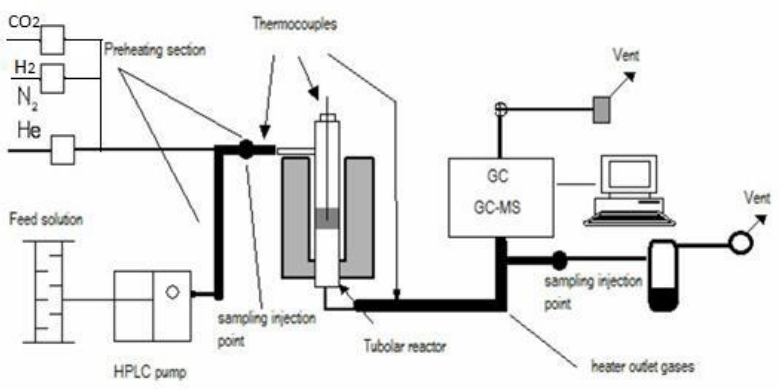

Figure 2.1: Scheme of the steam reforming catalytic line.

The carrier gas, Helium, is fed to the line controlling the flow rate through a dedicated Mass Flow controller. The liquid solution, ethanol-water (methanol-water) is fed through a HPLC pump into the preheating section in order to vaporize it. In this section, it is mixed with the carrier gas and the gaseous mixture flow to the fixed bed tubular reactor, made in silica glass, and collocated inside a furnace that can reach a temperature of 1273 K. The outlet gas passes through a condenser where condensable products or non converted reactants are separated, and then is vent out. In between the furnace and the condenser is collocated the sampling point. The analysis of the products and the reactants is made through GC and GC/MS techniques. Both the Mass Flow controller and the HPLC pump, and the GC results, were calibrated before every catalytic campaign.

The experiments were carried out in a flow fixed bed tubular glass reactor loaded with 7.4 mg of nanoparticles catalyst, or 44.1mg of supported catalysts mixed with respectively 476.5 and 442 mg of silica glass (60-70 mesh sieved). The solution feeding the plant had the following composition: a 6:1 Water:Ethanol molar ratio and 41.6% of Helium as gas carrier, with GHSV = 51700 h^{-1}.

The pre-heating and post-heating sections was kept at a temperature comprised between 480 K and 510 K. Product analysis was performed with a gas-chromatograph Agilent 4890 equipped with a Varian capillary column “Molsieve 5A/Porabond Q Tandem” and TCD and FID detectors in series. Between them, a nickel catalyst tube was employed to reduce CO_x to CH_4. Products analysis was also performed on GC/MS (FOCUS and ISQ from Thermo-Fisher), in order to identify the compounds. Experiments were always carried out in temperature ramp, in order to evaluate the catalytic activity at different temperature; moreover catalysts stability were also tested, over time, at the temperature corresponding to the maximum catalytic activity, in order to evaluate the catalyst

activity and its deactivation due to poisoning or coking. The temperature ramp tests were carried out at the following temperatures: 523K, 573K, 673K, 773K, after achieving the last temperature, the same temperature steps were followed during the descending ramp as shown in Figure 2.2. In the case of ESR the choice of this temperature range is related to the aim of developing efficient catalysts for “low temperature” where an efficient balance in energetic effect might be achieved and where CO_2 is more favored than CO and thus a higher H_2 yield might be achieved.

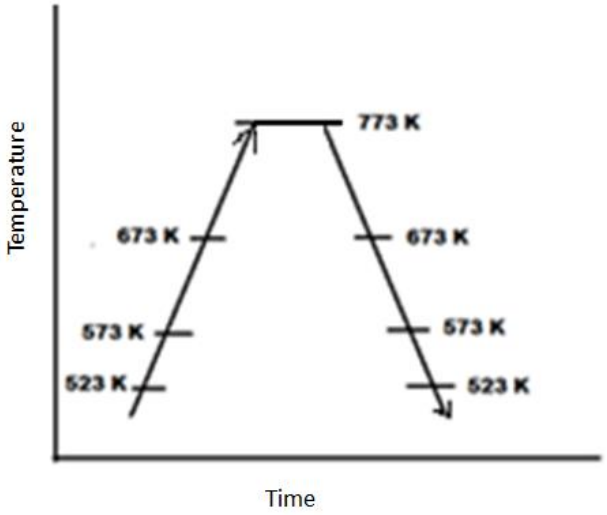

Figure 2.2: Temperature Ramp used during the ESR experiments.

For the quantitative studies the following relations have been used:

Reactants conversion is defined as:

$$X_{reactant} = \frac{nreact.\,in - nreact.\,out}{nreact.\,in}$$

Selectivity to a x_i product as:

$$S_i = \frac{n_i}{\nu_i(nreact.\,in - nreact.\,out)}$$

Where n_i is the moles number of compound i, v_i is the ratio of stoichiometric reaction coefficients, n_{react} in and out are respectively the number of moles of ethanol (methane) at the inlet and the outlet of the reactor.

The hydrogen yield is calculated as:

$$Y_{H2} = \frac{n_{H2\ out}}{6 * (n_{ethanol\ in})}$$

2.5.2 CO_2 hydrogenation experiments

For these experiments the line used is shown in the following Fig. 2.3

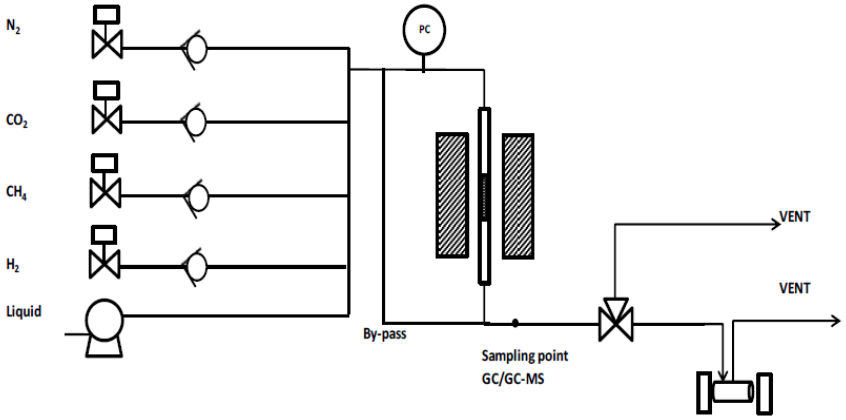

Figure 2.3: Scheme of the line use for the CO_2 methanation.

The gases are fed to the line through three different lines, in particular for N_2, CO_2 and H_2. The flow rate of each line is controlled by a dedicated Mass Flow controller, calibrated before every new test campaign.

The gas mixture is fed to the fixed bed tubular reactor, made by silica glass, sited inside a furnace, capable to reach 1273 K. The outlet gas passes first through a condenser, kept at 273 K, in order to abate the water coming out of the reactor, then through an IR cell and then is vented outside. The experiments were carried out using a reactor loaded with 88.2 mg of catalyst, on case of supported ones, and with 16 mg of nanoparticles catalysts, mixed up with 700 mg of silica glass (60-70 mesh sieved). The total flowrate was 42 ml/min with a H_2:CO_2 ratio 5:1. GHSV was equal to 52300 h^{-1}. In the case of methanation, the exothermal behavior is setting the operating temperature and

according to the literature it is well-known that Ni based catalysts work in 623-673 K range in CO methanation. Each temperature was kept for 30 minutes÷1 hour, ensuring the steady state conditions and/or evidence of deactivation processes.

It should be underlined that during catalytic tests of different samples, the catalyst weight, to compare unsupported and supported nanoparticles, was chosen to maintain the weight of active phase unaltered, i.e. weight of Co and/or Nickel in the present case. The experiments were designed in the way to keep constant the GHSV in between the two processes; a brief calculation in the WHSV gives rise to a difference that approaches 30%, and might be reasonably acceptable.

Online products analysis was performed using a Nicolet 6700 FT-IR instrument. A previous calibration of the instrument is carried out using gas mixtures with known concentrations, in order to have quantitative results. The frequencies analyzed, where CO_2, CH_4 and CO molecules absorb weakly, were :2293 cm^{-1} for CO_2, 2170 cm^{-1} for CO, 1333 cm^{-1} for CH_4 (after subtraction of baseline) Produced water was condensed upstream of the IR cell.

Quantitative analysis were carried out through IR spectroscopy, using the following relations:

CO_2 conversion:

$$X_{CO_2} = \frac{F_{CO_2}{}^{in} - F_{CO_2}{}^{out}}{F_{CO_2}{}^{in}}$$

Yield of the *i* species:

$$Y_i = \frac{F_i}{F_{CO2\ in}}$$

Selectivity to *i* product:

$$S_i = \frac{F_i}{F_{CO2\ in} - F_{CO2\ out}}$$

where F_i is the molar flow rate of i (i.e. CO and CH_4), while F_{CO_2} is the molar flow rate of CO_2, all expressed in mol/min. In order to investigate kinetic aspects, the catalysts were pretreated as

previously reported. In this case, 88.2 mg of supported-catalysts were diluted in 350 mg of silica glass.

To study the CO_2 reaction order, CO_2 partial pressure was varied between 0.02 atm and 0.07 atm while maintaining constant hydrogen partial pressure (p_{H_2} = 0.30 atm). The reaction temperatures were fixed at 493 K and 523 K for Nickel based catalysts, where the hypothesis of a differential reactor can be applied (CO_2 conversion in 3-15% range). The same procedure and hypothesis were made to study the reaction order with respect to H_2 concentration, where p_{H_2} was varied from 0.03 atm to 0.28 atm at constant p_{CO_2} (0.07 atm). At low temperature, an estimation of the apparent activation energy of CO_2 methanation was done, using the conversion values obtained under kinetic control at 493 K, 523 K and 573 K, thus deriving Arrhenius- type plots [2].

The amount of liquid water formed during reaction was measured at the end of each experiment, allowing to evaluate the goodness of our tests and as a further check of total mass balance.

2.6 References

[1] Pearson Crystal Data: Crystal structure database for inorganic compounds, ASM International, The Material Information Society

[2] Fogler HS, Elements of Chemical Reaction Engineering, IV ed., Pearson Education International, New Jersey, 2006.

Chapter 3

Preparation and characterization of Co NPs and their activity in ESR and CO_2 methanation

3.1 Introduction.

In the era of nanotechnology, catalysis by metal nanoparticles became a relevant field of investigation. In fact, a number of methods were developed allowing the preparation of well-characterized and shaped metal nanoparticles [1]. Moreover, metal nanoparticles are indeed very efficient catalysts for a number of organic reactions, as shown in the case of Pd nanocrystals [2].

Cobalt is an active catalyst for a number of hydrogenation reactions. It has been used, mostly supported such as e.g. the Co/Al_2O_3 or Co/SiO_2-ZrO_2 catalysts, in the low-temperature Fischer Tropsch process [3], CoO/SiO_2 and CoO/SiO_2-Al_2O_3, CoO/ZrO_2-Kieselguhr catalysts for hydrogenation of oxoaldehydes and amination of alcohols and the reductive amination of aldehydes and ketones for the manufacture of ethylamines and propylamines [4, 5, 6, 7].

Unsupported cobalt has been used in the past for Fischer Trøpsch synthesis [8], while Raney-type "sponge" cobalt is commercially available for use in the hydrogenation of nitriles and nitro compounds to amines [9].

Unsupported cobalt catalysts produced by reducing Co oxide where found to be very active for ESR [10, 11, 12]. Moreover, our group found that unsupported cobalt nanoparticles (NPs), prepared by reducing Co chloride with $NaBH_4$, may act as very good catalysts for ESR at least upon short time on stream experiments [13].

Because the synthetic procedure of nanoparticles strongly affect their morphological and compositional properties and it has a strong effect on their catalytic activity, in a previous work of the research group it has been clarified the effect of boron-based byproducts on the catalytic activity in ESR process catalyzed by Co NPs [14].

To go further on our investigations concerning ESR, CO_2 hydrogenation and cobalt based catalysts for these reactions, different cobalt precursor salts have been used to prepare CoNPs by reduction in aqueous solution of $NaBH_4$, in order to investigate the possible role of the different anions on the catalytic activity of the synthetized materials. Moreover, a further improvement has been achieved

preparing Co nanoparticles without using of $NaBH_4$ and thus removing completely the presence of B in the final product, allowing investigating Boron-free unsupported Cobalt nanoparticles as heterogeneous catalysts.

3.2 Experimental

The Co nanoparticles were prepared via reduction method in aqueous solution, starting from $CoCl_2 \cdot 6H_2O$ or $Co(NO_3)_2 \cdot 6H_2O$, as precursor salts and using $NaBH_4$ as reducing agent. The reaction was carried out using a $1.5 * 10^{-2}$ $molL^{-1}$ final concentration of the corresponding aqueous solution, and a ratio $Me^{2+}:BH_4^-$ varying, depending from the precursor salt: it is equal to 1:4 for $CoCl_2 \cdot 6H_2O$, and equal to 1:10 for $Co(NO_3)_2 \cdot 6H_2O$. The solution is maintained under vigorous mechanical stirring for 15 minutes. The appearance of the nanoparticles is easily observable due to the abrupt change in the solution color that becomes black. The Co NPs were then collected by filtering on a Gooch G4 filter, washed several times, dispersed, and, finally, dried under vacuum. Instead one of the sample, sample ***B***, after filtration has been dispersed in ethanol and slightly sonicated for 30 s in a low-power ultrasonic bath, in order to promote the following reaction:

$$2Co_2B + Co(BO_2)_2 \rightarrow 5\,Co + 2B_2O_x. \qquad \text{eq. 3.1)}$$

Moreover Co nanoparticles were also prepared by $Co_2(CO)_8$ thermal decomposition in anhydrous toluene. Before all the syntheses, washing cycles were performed, specifically three cycles of vacuum alternating with three cycles of Argon to make the environment of an inert reaction. Toluene and dicobalt octacarbonyl were then injected into the flask, using amounts such as to obtain a solution at a concentration of $1.5 * 10^{-2}$ $molL^{-1}$. The solution is kept under reflux for 2 hours; the Co NPs were then collected by filtering on a Gooch G4 filter, washed several times, and finally, dried under vacuum.

In Table 3.1, experimental conditions adopted to synthetize the Co-based catalysts are summarized.

Table 3.1:

Sample	Precursor	Co^{2+}/BH_4^-	Separation method
A	*cobalt chloride*	1:4	filtration
B	*cobalt nitrate*	1:10	filtration then sonication in air
C	*cobalt nitrate*	1:10	filtration
D	*dicobalt octacarbonyl*	-	filtration

The Ethanol Steam Reforming catalytic experiments were carried out as reported in paragraph 2.4.1, using 7.3 mg of catalyst mixed with 440 mg of silica glass particles.
CO_2 methanation experiment were carried out using the conditions described in paragraph 2.4.2, in particular using 16 mg of catalyst and 700 mg of silica glass particles.

3.3 Results and discussion

3.3.1 Characterization of the fresh catalysts

Different cobalt precursor salts have been used to prepare CoNPs by reduction in aqueous solution of $NaBH_4$, in order to investigate the possible role of the different anions on the catalytic activity of the synthetized materials, since the already deep knowledge on the effect of preparation parameters [14].

Thus, sample A has been prepared with the already tested methodology [13, 14] while a new synthetic procedure has been developed with $Co(NO_3)_2 \cdot 6H_2O$ as precursor salt with a BH_4^-:Co^{2+}=10 but exposing the obtained nanomaterial to different atmospheres. To our knowledge, this is the first attempt in the literature that aim and achieve to synthesis Co based nanopowders starting with nitrate precursor. A further improvement has been carried out in order to avoid the use of $NaBH_4$ and thus removing completely the presence of B in the final product, allowing to investigate Boron-free unsupported Cobalt nanoparticles as heterogeneous catalysts.

As from our previous work [13, 14, 15], all the prepared nanoparticles result to be completely amorphous after synthesis and washing procedures. Thus, all samples have been annealed with the well-established procedure (773 K for 2 hours in Argon atmosphere).

In Figure 3.1, the XRD patterns of the annealed samples are reported. Samples ***A*** and ***C***, even if they are prepared from different cobalt precursors but same separation procedure, display very similar diffraction patterns with two different crystalline phases: i) metallic cobalt (Co, cF4-Cu), and ii) Co_3B, approximately in the same quantities. Co_3B could arise from the solid-state reaction occurring at high temperature [16, 17]:

$$Co_2B + Co \rightarrow Co_3B. \qquad \text{eq 3.2)}$$

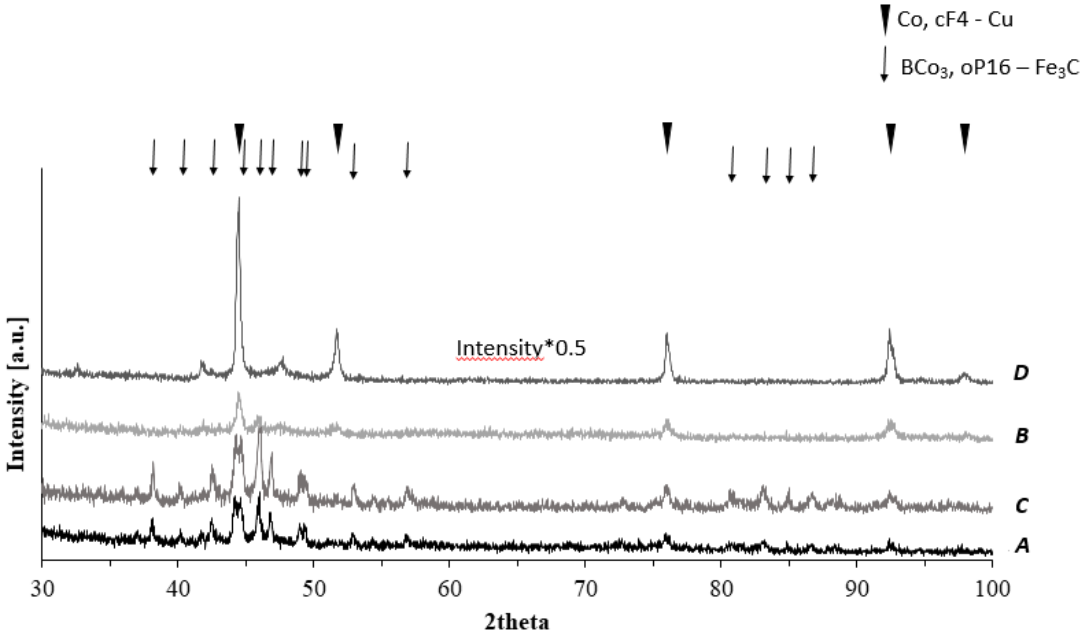

Figure 3.1: XRD patterns of the fresh catalytic materials

A different diffraction pattern is observed in the case of ***B*** annealed nanopowders, where the main observed crystalline phase is cubic metallic cobalt with a very small quantity of Co_xB. A pretty similar situation is observed in the case of ***D***, where two different metallic cobalt crystalline structure are identified, with a predominance of the cubic structure with respect to the hexagonal one.

In Figure 3.2, the IR spectra of the investigated samples are reported together with the spectra of two commercial reference compounds, i.e. Co_3O_4 and $CoCO_3$.

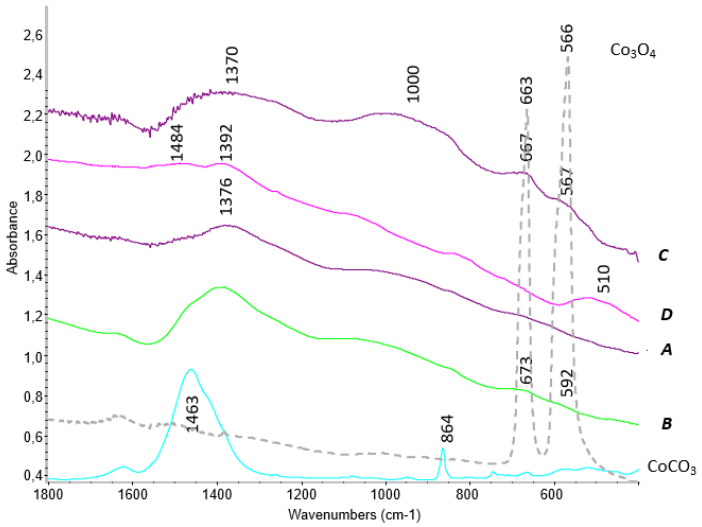

Figure 3.2. Skeletal FT-IR spectra (KBr pressed disks) of the fresh catalytic materials.

The spectrum of Co_3O_4, also reported in the figure, is in good agreement with spectra reported in literature [18, 19, 20]. In fact, spinel IR spectrum foresees four triply degenerated IR active modes (from the 39 possible optical modes), two of which fall in the MIR. Both bands in the MIR region are split into two components, which can be attributed to TO / LO (transverse and longitudinal optical modes, respectively) components [19, 20]. We find the maxima in the spectrum of our reference Co_3O_4 sample at 663 and 566 cm^{-1}, i.e. in intermediate positions with respect to those expected for TO and LO modes. It is in fact known that the transmission IR spectra of bulk particles are strongly dependent on the size, shape [21] and aggregation [22] of particles, that in fact modify the relative intensities and splittings of these polar modes. $CoCO_3$ displays only the feature at 1463 assigned to CO_3^{2-} species, while no components are observed at lower wavenumbers. For the samples arising from the $NaBH_4$ synthetic route (***A***, ***B***, ***C***), only broad components appear at 1484 and 1392-76 cm^{-1} together with weak features centered at 1062, 992 and 725 cm^{-1}. For the samples ***B*** and ***C***, together with the above mentioned features two additional weak components are observed at 673 and 592 cm^{-1} that well play with the presence of cobalt oxidised species, i.e. in the form of Co_3O_4. According to the literature [23, 24], borate species present quite different characteristic spectra for different boron oxygen compounds. Planar BO_3^{3-} groups show bands in the region 1500-1200 cm^{-1}, due to the asymmetric B-O stretching, together with features near 940 cm^{-1} due to symmetric B-O stretching and the corresponding in-plane and an out-of-plane bending modes near 740 and 650 cm^{-1}, respectively. Tetrahedral borate species give rise to asymmetric and symmetric B-O stretchings in the region 1100-900 cm^{-1}. The observed features are similar to those reported Al_2O_3-boria samples [23, 24], where, as in this case, the main borates are found as trigonal planar with a second component that might be assigned to the presence of tetrahedral borates. Similar features have been also found for nanosized Cobalt catalysts for the $NaBH_4$ hydrolysis [25], on the unsupported CoNPs and on mechanical deposited Co nanoparticles on γ-alumina [26].

A slightly different situation is observed for ***D***, where three main features are detected: the former two arising from carbonate species (1400 and 1491 cm^{-1}) which can be associated either with surface or bulk cobalt carbonates [27]. The latter one is found at 510 cm^{-1} and well agrees with the value reported for *fcc* CoO material [28]; in our case, it can be an indication of some surface oxidation, since the absence of the corresponding CoO characteristic XRD pattern. It has to be remarked that no organic compound have been evidenced on this sample suggesting that a proper drying procedure has been carried out.

In Figure 3.3 the morphologies of the fresh synthetized Co-based nanoparticles are shown.

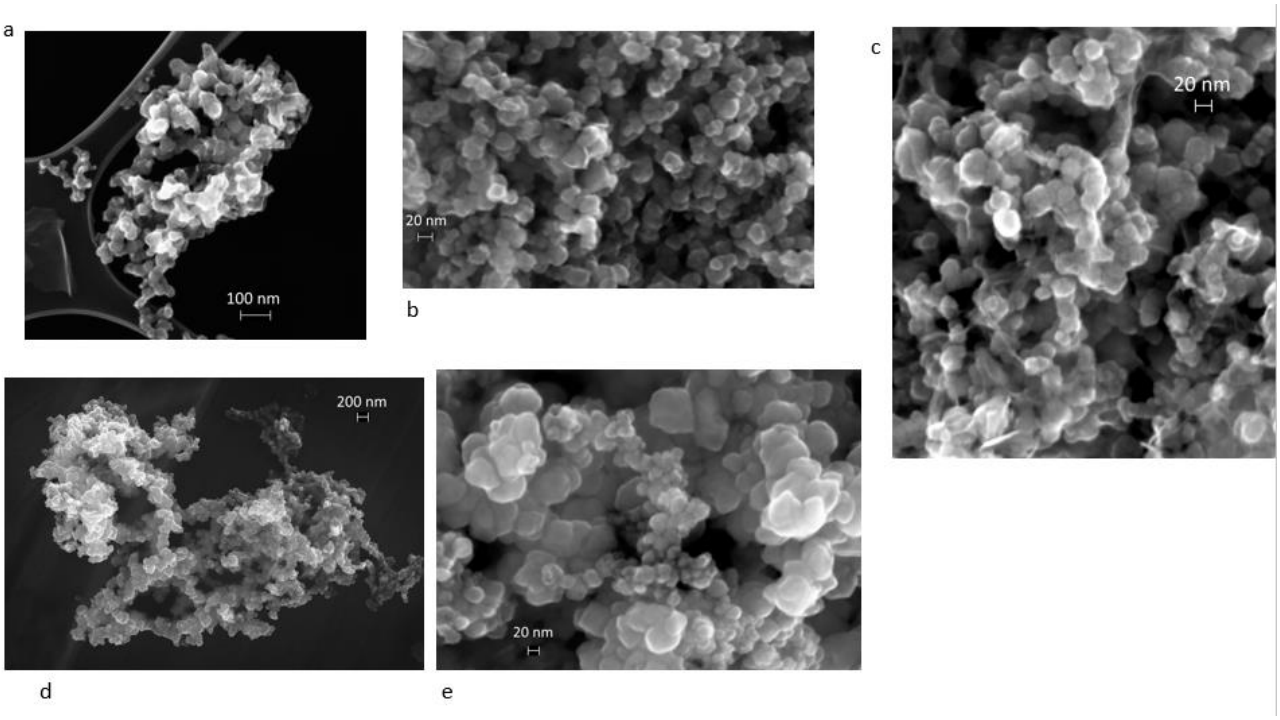

Figure 3.3 FE-SEM micrographs of the fresh catalytic materials. (a): sample ***A***; (b): sample ***B***; (c): sample ***C***; (d) and (e): sample ***D*** (different magnification).

Co NPs produced by reduction synthesis (Fig. 3.3 a, b and c) are agglomerate and they have a quite globular shape with an average diameter varying in the range 10-30 nm. Co NPs produced by thermal decomposition are agglomerated in long chains (Fig.3.3d) and they show two different morphologies (Fig.3.3 d, e): bigger platelets, with a diameter of about 50 nm and smaller rounded particles with an average diameter of about 20 nm.

3.3.2 Catalytic activity in CO_2 hydrogenation

In Figure 3.4, the profiles arising from CO_2 methanation in the ascending and descending temperature experiments are reported for ***B***, ***C*** and ***A*** materials respectively.

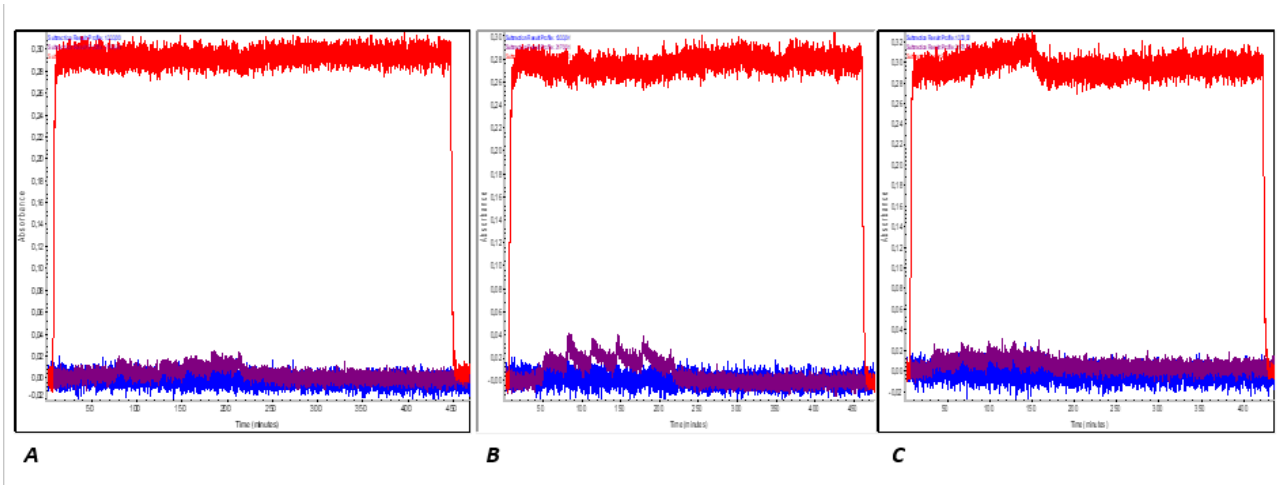

Figure 3.4. On-line FT-IR transmission/absorption analyses of the product gases upon catalytic hydrogenation experiments on samples: ***B*** (a), ***C*** (b), and ***A*** (c).

The calculated CO_2 conversion and CO and CH_4 yields are listed in Table 3.2.

T furnace [K]	X CO_2	Y CH_4	Y CO
523	7%→4%	5%→4%	1%
573	18%→15%	11%→10%	8%→7%
623	35%→30%	22%→14%	15%→16%
673	45%→43%	26%→16%	25%→28%
723	51%→42%	17%→6%	38%→36%
773	49%	4%	45%
723	43%	5%	38%
673	25%	3%	22%
623	10%	1%	9%
573	3%	1%	2%
523	2%	0%	2%

Table 3.2: CO_2 hydrogenation results in terms of CO_2 conversion, CO and methane yields

In all cases, CO_2 conversion is lower than 5% and no methane is detected among products, thus on these materials CO_2 hydrogenation to methane is completely hindered. However, the only detectable product is CO, produced mainly by reverse water gas shift reaction (eq. 3.3).

$$CO_2 + H_2 \rightleftarrows CO + H_2O \qquad \text{eq 3.3)}$$

The profile for CO production slightly differs as a function of the starting nanomaterial. In particular, ***C*** (Figure 3.4b) is the catalyst with the lowest catalytic activity in reverse WGS even though some CO is already produced at the minimum reaction temperature (523 K) and its yield remained almost constant for each temperature step in the increasing temperature experiment (523-673 K). This

catalyst is completed deactivated in the RWGS reaction after the step at 723 K (in increasing temperature) and it does show any remarkable catalytic activity in the decreasing temperature experiment. When the catalyst is exposed for a brief sonication in atmosphere, a slightly different catalytic activity is observed (sample ***B***, Figure 3.4a). As observed before no methane is produced but RWGS activity is slightly enhanced already at 523 K. Interestingly, in this case, by a temperature increase, activity is increased but a sever deactivation occurs at each temperature step with a behaviour similar to the one observed for Co/SiO_2 when acetate is used as precursor [see Chapter 5]. However, after the step at 723 K the catalyst is completely deactivated and again no recover is observed in the decreasing temperature experiment. This suggests that a key-role in RWGS activity is played by cobalt-oxidised species that are easily deactivated under CO_2 hydrogenation conditions. A different situation is observed for catalyst ***A***; it demonstrates a shift of RWGS activity to slightly higher temperatures than those observed for ***C*** catalyst (figure 3.4c); in fact, only above 523 K, a limited activity in CO production is observed and a steady state behaviour for each step can be envisaged. At this point, the limited activity can be due mainly to two different reasons: i) poisoning arising from borate species or ii) negligible activity of Co unsupported Cobalt nanoparticles. In order to clarify it, boron has been removed from preparation procedure and the profiles are reported in Figure 3.5.

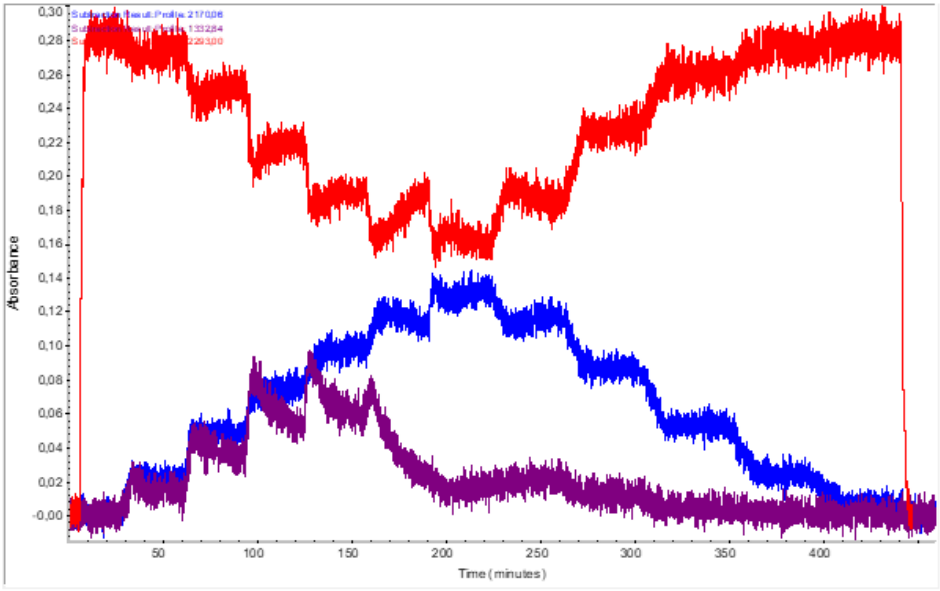

Figure 3.5. On-line FT-IR transmission/absorption analyses of the product gases upon catalytic hydrogenation experiments on sample ***D***.

In the case of ***D*** catalyst, a remarkable activity is seen in CO_2 hydrogenation to both methane and CO already at the minimum reaction temperature and the catalyst works in steady state conditions, even though a slightly deactivation is observed in terms of CO_2 conversion (from 7% to 4%). A temperature increase to 573 K produces a higher catalytic activity but together it brings an even stronger deactivation that is much more remarkable for methane yield (11 to 8%) than for CO. A similar situation is observed upon temperature increase at 623, 673 and 723 K where CO yield remains almost constant, few percentages of difference are observed, while a reduction of 40-60% is observed for methane yield. However, also in this case the temperature of 723 K is a critical one for Co based materials and afterward the catalysts loses 80% activity in terms of methane yield while it remains active as RWGS catalyst (49% CO_2 conversion, 45% CO yield). In the decreasing temperature experiment, the main product is CO and no deactivation in RWGS is observed suggesting that an irreversible catalyst modification happened at 723 K and it is not recovered by decreasing T experiment. This behaviour is similar to the one reported for Cobalt@silica catalysts when acetate is used as cobalt precursor and the catalytic performance is far away from the one predicted by thermodynamic equilibrium in the same conditions (see Chapter 5). These results suggest that boron is mainly affecting hydrogenation ability of Co catalysts thus hindering completely catalytic activity and, as well, the presence of boron in the form of borides is detrimental for unsupported cobalt nanoparticles used as catalysts for CO_2 methanation. On the other hand, B-free unsupported Co nanoparticles are active in CO_2 hydrogenation confirming that Co is an active metal for this reaction [29], but they suffer of strong deactivation after reaching 723 K. This can be due to the partial oxidation occurring at water expenses during catalytic test; in fact Co oxidised species are reported as responsible for enhanced RWGS activity and CO presence might favour the Boudouard reaction that produces carbon deposition on catalysts surface (reaction 3.4)

$$2CO \rightleftarrows C + CO_2 \qquad \text{eq 3.4)}$$

3.3.3 Catalytic activity in ethanol steam reforming

Ethanol steam reforming results are summarised in Tables 3.3-3.6.

T (K)	X C_2H_6O	X H_2O	Y H_2	S CH_4	S CO	S CO_2	S CH_2CH_2	S CH_3CH_3	S C_3H_6	S CH_3CHO	S CH_3COCH_3	S $C_4H_8O_2$
523	6%	0%	1%	1%	1%	0%	0%	0%	0%	98%	0%	1%
573	36%	1%	8%	1%	3%	5%	0%	0%	0%	91%	0%	0%
673	71%	17%	40%	10%	15%	45%	0%	0%	0%	28%	0%	0%
773	89%	31%	67%	6%	8%	70%	0%	0%	0%	16%	0%	0%
673	62%	24%	50%	6%	4%	79%	0%	0%	0%	11%	0%	0%
573	11%	1%	3%	1%	1%	12%	0%	0%	1%	85%	0%	0%
523	1%	0%	0%	0%	0%	0%	0%	0%	14%	86%	0%	0%

Table 3.3: : Ethanol conversion and products selectivities in ESR over ***C*** sample

In Table 3.3 data on ***C*** catalyst are reported. This catalyst shows negligible catalytic activity at low temperature with acetaldehyde as main product. It becomes more active at 573 K where again dehydrogenation reaction is the predominant one. Steam reforming activity rises up at 673 K where ethanol conversion reaches 71% with a hydrogen yield of 40% limited mainly by the copresence of acetaldehyde (28% selectivity). At the maximum reaction temperature, i.e. 773 K, ethanol is not completely converted (89%), hydrogen yield reaches 67% being CO_2 the main product together with acetaldehyde, CO, CH_4 whose are responsible for the limited hydrogen yield. By decreasing the reaction temperature, back to 673 K ethanol conversion is reduced to 62% against the 71% value obtained in the increasing temperature e experiments, but steam reforming reaction producing CO_2 displays an even higher activity with respect to the one observed in increasing temperature, mainly achieved for the reduction of acetaldehyde selectivity (11% against 28%). Below 573 K, ethanol steam reforming activity is hindered and ethanol conversion is lower than 15% with acetaldehyde as main product.

T(K)	X C_2H_6O	X H_2O	Y H_2	S CH_4	S CO	S CO_2	S C_3H_6	S CH_3CHO	S $C_4H_8O_2$
523	7%	0%	1%	1%	2%	0%	1%	96%	1%
573	30%	0%	6%	1%	3%	3%	0%	87%	7%
673	64%	8%	25%	3%	7%	25%	0%	63%	0%
773	73%	23%	51%	10%	17%	61%	0%	12%	0%
673	38%	9%	21%	6%	6%	45%	0%	43%	0%
573	7%	1%	2%	1%	2%	16%	2%	80%	0%
523	1%	0%	0%	0%	0%	0%	7%	93%	0%

Table 3.4) Ethanol conversion and products selectivities in ESR over ***B*** sample

On sonicated ***B*** sample, table 3.4, similar activities are obtained, even though a slight decrease in ethanol conversion is observed at all temperatures but more pronounced at 673 K and 773 K where a loss of 20% in terms of hydrogen yield is observed, achieving a value of 51 %. A more remarkable deactivation is observed in the decreasing temperature experiment already at 673 K where a loss of activity of approximately 50% is achieved. By further lowering reaction temperature, ethanol conversion further reduces below 10% and with an almost complete selectivity to acetaldehyde.

T(K)	X C_2H_6O	X H_2O	Y H_2	S CH_4	S CO	S CO_2	S CH_2CH_2	S C_3H_6	S CH_3CHO	S CH_3OCH_3	S $C_4H_8O_2$	S CH_3COOH
523	34%	0%	6%	2%	3%	1%	0%	0%	93%	0%	0%	1%
573	37%	1%	8%	2%	5%	6%	0%	0%	75%	0%	12%	0%
673	84%	7%	28%	4%	10%	17%	4%	0%	57%	2%	6%	0%
773	100%	39%	82%	8%	11%	77%	2%	0%	1%	0%	0%	0%
673	54%	1%	12%	1%	1%	18%	26%	0%	28%	2.5%	1%	0%
573	7%	0%	1%	0%	0%	4%	1%	2%	87%	4%	2%	0%
523	1%	0%	0%	0%	0%	5%	0%	4%	87%	4%	0%	0%

Table 3.5: Ethanol conversion and products selectivities in ESR over ***A*** catalyst

The results on ***A*** catalyst (see Table 3.5) are almost similar to the ones reported in our previous works on nanoparticle containing boron in the form of borides but with a reduced borate quantity. In this case, an already remarkable conversion is observed at lower temperature with acetaldehyde and ethyl acetate as main products at low temperature. Ethanol conversion rises up at 673 K even though a still remarkable acetaldehyde selectivity remains, thus limiting to 28% hydrogen yield. At

the maximum reaction temperature (773 K), hydrogen yield reaches 82 % together with a limited selectivity to methane and CO (6 and 98% respectively, and an acetaldehyde selectivity of 1%, being CO_2 the main product (77% selectivity)

A remarkable deactivation is observed in the decreasing temperature experiment with a severe reduction of 30% in ethanol conversion.

On table 3.6 the results arising from ethanol steam reforming tests over ***D*** catalyst are summarised.

T(K)	X C_2H_6O	X H_2O	YH_2	S CH_4	S CO	S CO_2	S CH_2CH_2	S C_3H_6	S CH_3CHO	S CH_3COOH	S CH_3COCH_3	S $C_4H_8O_2$
573	15%	0%	2%	1%	2%	2%	0%	0%	80%	0%	3%	2%
673	41%	0%	6%	4%	12%	3%	11%	0%	64%	0%	2%	4%
773	100%	36%	76%	14%	12%	73%	0%	0%	0%	0%	0%	0%
673	63%	3%	17%	4%	8%	13%	7%	0%	50%	11%	0%	6%
573	9%	0%	2%	1%	2%	2%	1%	0%	87%	4%	0%	3%
523	8%	0%	1%	1%	1%	2%	1%	1%	90%	4%	0%	0%

Table 3.6: Ethanol conversion and products selectivities in ESR over ***D*** catalyst

Ethanol conversion is limited at 573 K with acetaldehyde as main product but with several by-products as ethane, acetone and ethylacetate. A temperature increase enhances activity but still a poor activity toward steam reforming is observed. At the maximum temperature (773 K), ethanol is completely converted with CO_2 as main product (73%) and with the coproduction of only methane and CO (14 and 12% selectivities, respectively) thus arriving to a hydrogen yield of 76 % that well plays with the values previously observed for ***A*** sample. A remarkable increase in ethanol conversion and hydrogen yield (17% against 5% in the increasing temperature) is achieved by lowering the reaction temperature to 673 K but a slight loss in selectivity is found; in fact, together with acetaldehyde (50% selectivity), acetone (11% selectivity), ethylacetate and propylene are found among products. As observed for all other cases, a further decrease in the reaction temperature produces mainly a reduction of conversion with the predominance of acetaldehyde as product, mainly arising from ethanol dehydrogenation reaction.

This further confirms that boron in the form of borate is deactivating ESR but enhancing ethanol decomposition reaction to produce methane and CO. Moreover, by comparing these data with the one of CO_2 hydrogenation we can conclude that all the methane produced is mainly arising from

ethanol decomposition and not from CO_x hydrogenation, since the nil activity of ***A***, ***B***, and ***C*** catalysts for this reaction. Boron in the form of borides in the unsupported cobalt nanoparticles does not affect catalytic activity in ESR, but a small contribution in CO_x hydrogenation might be foreseen for Co metal particles synthetized for $Co_2(CO)_8$ precursor.

3.3.4 Characterisation of exhaust samples

All the exhaust catalysts have been characterized by means of XRD and FE-SEM after their use both in the Ethanol steam reforming and in CO_2 methanation processes.

In Figure 3.6, the diffractograms of the catalysts after methanation experiments are reported.

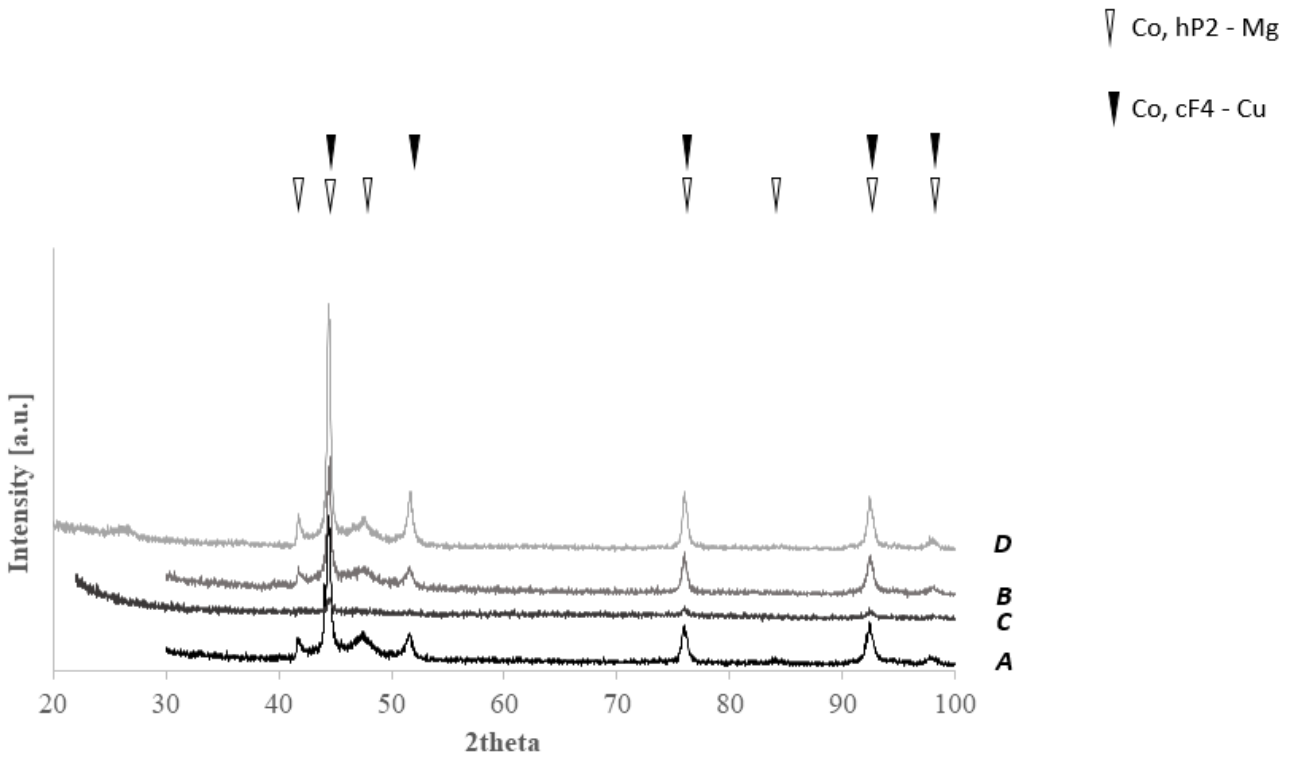

Figure 3.6. XRD patterns of the spent catalysts after methanation experiments.

It is possible to distinguish for all of them, two different crystalline phases; the first one is the metallic Co with the cubic structure (cF4-Cu) while the second one is always metallic Co but with the hexagonal structure (hP2-Mg), that is stable under 693 K. This means that at equilibrium only the

hexagonal form should appear, but in practice the transformation from cubic to hexagonal, being a solid state process is kinetically inhibited; so in this case partially occurred, while in other case it doesn't occur at all. In the diffraction pattern of sample ***D*** also a very broad peak around 2theta equal to 26° appears, assignable to the presence of graphitic carbon.

In Figure 3.7, the diffraction patterns of the catalysts after steam reforming experiments are reported.

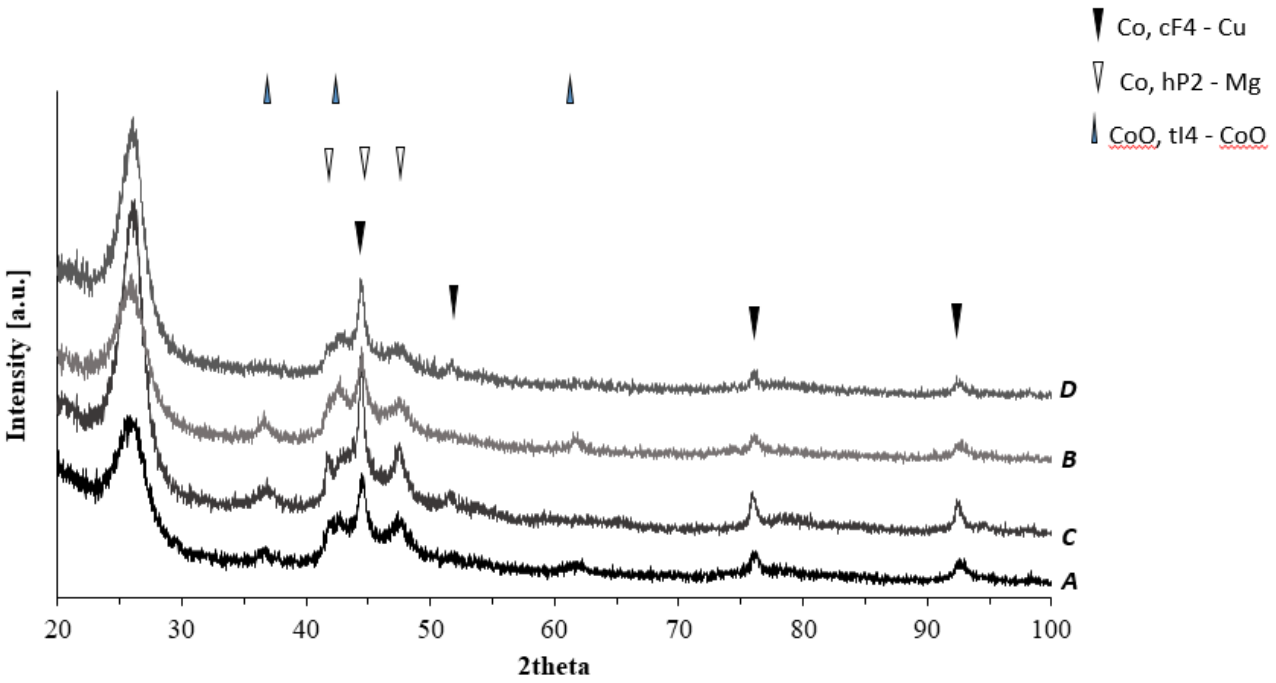

Figure 3.7. XRD patterns of the spent catalysts after ethanol steam reforming experiments

It is possible to distinguish for all of them the main features of graphitic carbon (2theta=26° and 43°); moreover in the samples synthetized by reduction in aqueous solution with $NaBH_4$, we can observe the peaks of CoO crystalline, as minority phase. In all the catalysts the majority phase is the metallic Co with the cubic structure (cF4-Cu); especially in samples ***A*** and ***C*** together with the peaks of the cubic structure also those of the hexagonal structure (hP2-Mg), can be distinguished.

Representative FE-SEM micrographs of the catalysts after methanation experiments are shown in Figure 3.8, where it is possible to observe that nanoparticles of all the samples are grown in diameter, due to a sintering phenomenon, and they seem to be embedded in a carbon veil.

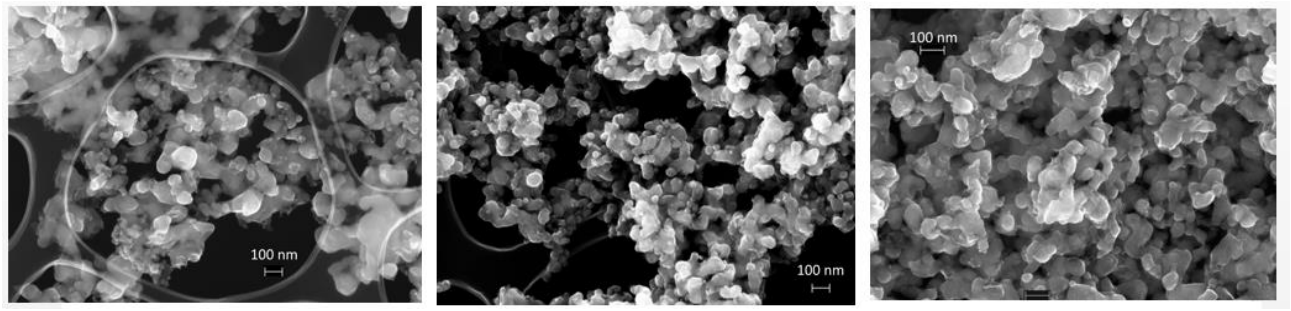

A ***B*** ***C***

Figure 3.8. FE-SEM micrographs of the spent catalysts after methanation experiments.

In Figure 3.9 FE-SEM micrographs of the materials after steam reforming experiments are shown. For all the catalysts it is possible to identify well dispersed nanoparticles in a matrix of carbon nanotubes, as always observed for Co-based nanoparticles catalysts after this process [13, 14, 15].

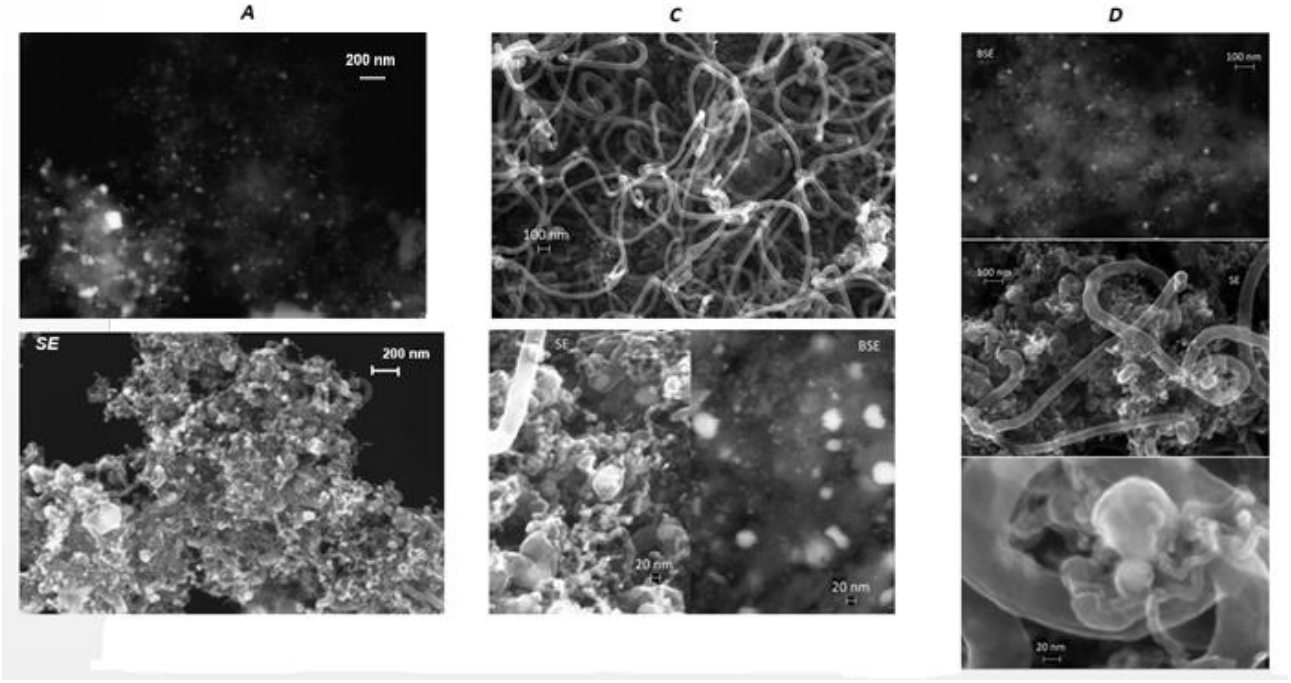

Figure 3.9. FE-SEM micrographs of the spent catalysts after ethanol steam reforming experiments at different magnification

3.4. Conclusions

The main conclusion of this work are the following:

- It is possible to obtain Co-nanoparticles by reduction with sodium borohydride even if nitrate cobalt precursor is used, without any change in the morphology of the synthetized NPs.
- It seems that no effect of the precursor is observed on catalytic activity, while residual boron has a strong effect on catalytic activity.
- In particular Boron deactivates Co catalysts in CO_2 methanation, and not only hinders the rWGS reaction but it avoid the formation of C-H bonds. The presence of Co^{2+} species seems to catalyse RWGS reaction, even though a fast deactivation is observed for all $NaBH_4$-based NPs.
- Unsupported cobalt nanoparticles produced by carbonyl are active in the CO_2 hydrogenation, however they suffer of deactivation due to carbon deposition in the form of encapsulating carbon through Boudouard reaction.
- In ESR the presence of oxidized cobalt species reduces H_2 yield and ethanol conversion favoring ethanol dehydrogenation reaction
- In ESR the absence of boron slightly reduces the hydrogen yield and this might be due to a small activity in COx hydrogenation of bare Co metallic particle. Thus the fundamental understanding of the role of boron is here further clarified
- The exhaust materials are mainly composed by cubic metallic cobalt coupled with the presence of hcp cobalt. In ESR a clear carbon deposition is observed for all catalysts while for CO_2 methanation a weak feature coming from graphitic carbon is observed for ***D*** the only catalysts active for this reaction.

3.5. References

[1] C. Burda, X. Chen, R. Narayanan, M.E. El-Sayed, Chem. Rev. 105 (2005) 1025-1102.

[2] B.C. Ranu, K. Chattopadhyay, L. Adak, A. Saha, S. Bhadra, R. Dey, D. Saha, Pure Appl. Chem. 81 (2009) 2337-2354.

[3] A.Y. Khodakov, W. Chu, P. Fongarland, Chem. Rev. 107 (2007) 1692-1744.

[4] G. Busca, Heterogeneous Catalytic Materials, Elsevier, Amsterdam, 2014.

[5] T. L. Renken, M. W. Forkner US Patent Application 20080227632 (2008) to Huntsman petr. Co.

[6] B. Chen, U. Dingerdissen, J.G.E. Krauter, H.G.J. Lansink Rotgerink, K. Möbus, D.J. Ostgard, P. Panster, T.H. Riermeier, S. Seebald, T. Tacke, H. Trauthwein, Appl. Catal. A Gen. 280 (2005) 17-46.

[7] P.R. Likhar , R. Arundhathi, M.L. Kantam, P.S. Prathima, Europ. J. Org. Chem. 31 (2009) 5383-5389.

[8] B.H. Davis, in Greener Fischer-Tropsch Processes for Fuels and Feedstocks, P.M. Maitlis, and A. de Klerk, eds., Wiley, New York, 2011, pp. 193-200

[9] The catalyst technical Handbook, Johnson Matthey, 2008, available on internet

[10] V.A. de la Peña O'Shea, N. Homs, E.B. Pereira, R. Nafria, P. Ramirez de la Piscina. Catal. Today 126 (2007) 148–152.

[11] S. Tuti, F. Pepe, Catal. Lett. 122 (2008) 196-203.

[12] W. Gac, W. Zawadzki, B. Tomaszewska, Catal. Today 176 (2011) 97–102

[13] G. Garbarino, P. Riani, M. A. Lucchini, F. Canepa, S. Kawale, G. Busca, Int. J. Hydrogen Energ., 38 (2013) 82-91.

[14] Riani P, Garbarino G, Infantes-Molina A, Rodríguez-Castellón E, Canepa F, Busca G, Hydrogen from steam reforming of ethanol over cobalt nanoparticles: effect of boron impurities, *Appl Catal A Gen* **518** 67-77 (2016).

[15] P. Riani, G. Garbarino, M. A. Lucchini, F. Canepa, G. Busca J. Mol. Catal. A: Chem. 383– 384 (2014) 10– 16.

[16] G.N. Glavee, K.J. Klabunde, C.M. Sorensen, G.C. Hadjapanayis, Langmuir 8 (1992) 771-773.

[17] G.N. Glavee, K.J. Klabunde, C.M. Sorensen, G.C. Hadjapanayis, Langmuir 9 (1993) 162-169.

[18] G. Busca, R. Guidetti and V. Lorenzelli, J. Chem. Soc., Trans., 1990, 86 , 989-994.

[19] M. Lenglet, B. Lefez, Solid State Commun. 98 (1996) 689-694.

[20] Y. Li, W. Qiu, F. Qin, H. Fang, V.G. Hadjiev, D. Litvinov, J. Bao, J. Phys. Chem. C, 120 (2016) 4511-4516.

[21] M. Andrés-Vergés, C.J.Serna, J. Mat. Sci. Letters 7(1988) 970-972

[22] J. E. Iglesias, M. Ocaña, C.J. Serna, Appl. Spectrosc., 44 (1990) 418-426

[23] Delmastro A, Gozzelino G, Mazza D, Vallino M, Busca G, Lorenzelli V, Characterization of microporous amorphous alumina-boria, *J Chem Soc Faraday Trans* **88**:2065-2070 (1992).

[24] Mazza D, Vallino M, Busca G, Mullite-type structures in the systems Al_2O_3-Me_2O (Me = Na, K) and Al_2O_3-B_2O_3, *J Am Ceram Soc* **75**:1929-1934 (1992).

[25] Simagina VI, Komova OV, Netskina OV, Nanosized Cobalt Catalysts for Hydrogen Storage Systems Based on Ammonia Borane and Sodium Borohydride, in Gromov, A., Teipel, U., Metal Nanopowders: Production, Characterization, and Energetic Applications, 2014:199-227

[26] P. Riani, G. Garbarino, F. Canepa, G. Busca, J. Chem. Technol. Biotechnol. (2018) in press published on internet.

[27] B. Klingenberg, M.A. Vannice, Chem. Mater. 8 (1996) 2755–2768.

[28] Chih-Wei Tang, Chen-Bin Wang, Shu-Hua Chien, Thermochimica Acta 473 (2008) 68–73.

[29] T.A. Le, M.S. Kim, S.H. Lee, E.D. Park, Top. Catal 60 (2017) 714–720

Chapter 4

Preparation and characterization of Co NPs and their activity in ESR

Our research group reported previously on the preparation and characterization of transition metal nanoparticles (NPs), in particular Nickel [1] and Cobalt [2, 3, 4], and on their application to a high-temperature catalytic reaction, the Ethanol Steam Reforming (ESR), to produce syngas and hydrogen; this process is potentially useful for producing renewable hydrogen starting from bioethanol [5, 6]. In these studies was found that, although Ni catalysts are most commonly used for steam reforming reactions, Co NPs may be, depending on preparation conditions, even more active than Ni nanoparticles and are also more performant and stable (at the laboratory conditions and timescales) than conventionally prepared catalysts for this application.

A common method for producing metal nanoparticles, both of noble metals (such as e.g. platinum [7]) and of the less easily reducible transition metals [8], is to reduce metal salts with sodium borohydride ($NaBH_4$). We have, however, shown that the resulting nanoparticles can be contaminated by boron impurities, that, depending on the preparation history of the samples, can act as deactivating agents or not [17]. In particular, we found that the presence of borates tends to reduce activity of Co NPs based catalysts, while the presence of cobalt borides may be not deactivating [17].

Concerning conventional supported catalysts, we previously found that alloying Nickel with Cobalt [9, 10, 11, 12, 13] may produce even better catalysts than monometallic ones for ESR, even because the nature of the support has been reported to have a considerable effect on the activity of the metal [14, 15, 16].

In this chapters are described synthesis of unsupported (Co,Ni) nanoparticles, and their activity as catalysts for Ethanol Steam Reforming. The aims of this work are: i) to check the effect of the preparation procedure on the resulting (Co,Ni) nanomaterials, ii) to evaluate the effect of the bimetallic formulation and on the role of boron impurities in a complex system and iii) to elucidate the chemistry of the ESR process for (Co,Ni) NPs.

4.1 NPs preparation of bimetallic nanoparticles.

The (Co,Ni) nanoparticles were prepared via reduction method in aqueous solution, starting from $NiCl_2 \cdot 6H_2O$, $CoCl_2 \cdot 6H_2O$ and using $NaBH_4$ as reducing agent. The reaction was carried out using a 1:1 (samples A, B, C, D, E) or 2:1 (sample F) or a 4:1 (sample G) concentration ratio between Co(II) and Ni(II) chloride salts, in order to reach a final concentration of 10^{-2} M for metals in solution, with a Me^{2+}:BH_4^- ratio equal to 1:2.

The aqueous salt solution was kept under vigorous mechanical stirring in Argon atmosphere; once obtained a good homogeneity, sodium borohydride was added. Its addition caused a rapid change in the solution color that turned into black, confirming the appearance of the nanoparticles. The reaction mixture was maintained under vigorous mechanical stirring for 15 minutes, then the (Co,Ni) NPs were collected using different methods (centrifugation sample D, filtration samples A, B, F, G, filtration followed by sonication samples C, E), washed several times and, finally, dried and stored in dynamic vacuum. As already observed for Co NPs [2, 3, 17] the washing procedure strongly affects the purity of the sample. This is related to the adopted reducing agent that could leave boron in the final product, thus producing metal borides together or instead of the corresponding metals. This inconvenient can be avoided by washing in open air, thus converting the boron impurities into borates, which can be then removed during the washes with water.

The notation of the samples and their main characteristics are summarized in Table 4.1.

Table 4.1. Summary of catalysts properties

Sample notations	Separation method	Ni/Co nominal composition	Ni/Co measured composition	B/Me (Me=Co,Ni) measured ratio	A $(BO_3)^{3-}$
A	filtration	1	1	1	0.13
B	filtration	1	1	1	0.23
C	sonication	1	1	0.43	0.24
D	centrifugation	1	n.m.*	n.m.*	0.4
E	sonication	1	n.m.*	n.m.*	0.25

F	filtration	0.50	0.52	1	0.13
G	filtration	0.25	0.26	1	0.18
* n.m. stays for not measured					

4.2 Result and discussion

4.2.1 Separation, behavior and characterization of catalyst D, separated by centrifugation

The separation of the (Co,Ni) NPs from the reaction medium has been performed through centrifugation carried out applying the following process parameters 7500 rpm and a total time of 15 min, followed by washing in deionized water, then in ethanol and drying under vacuum. According to previous indications, this procedure guarantees a long contact time between nanoparticles and an oxidizing atmosphere, thus producing the conversion of boron in the borides to borates as much as possible. The sample has been characterized by means of XRD before annealing (not shown), providing evidence of a complete amorphicity of the sample, and after annealing in Ar at 773 K for 3 h. In this case (Figure 4.1), crystalline $B_2O_6M_3$ (M=Ni, Co) with an orthorhombic structure pertaining to space group number 58 (oP22, $Mg_3(BO_3)_2$ type) is present together with the features of cubic metallic (Ni,Co) solid solution (cF4-Cu type).

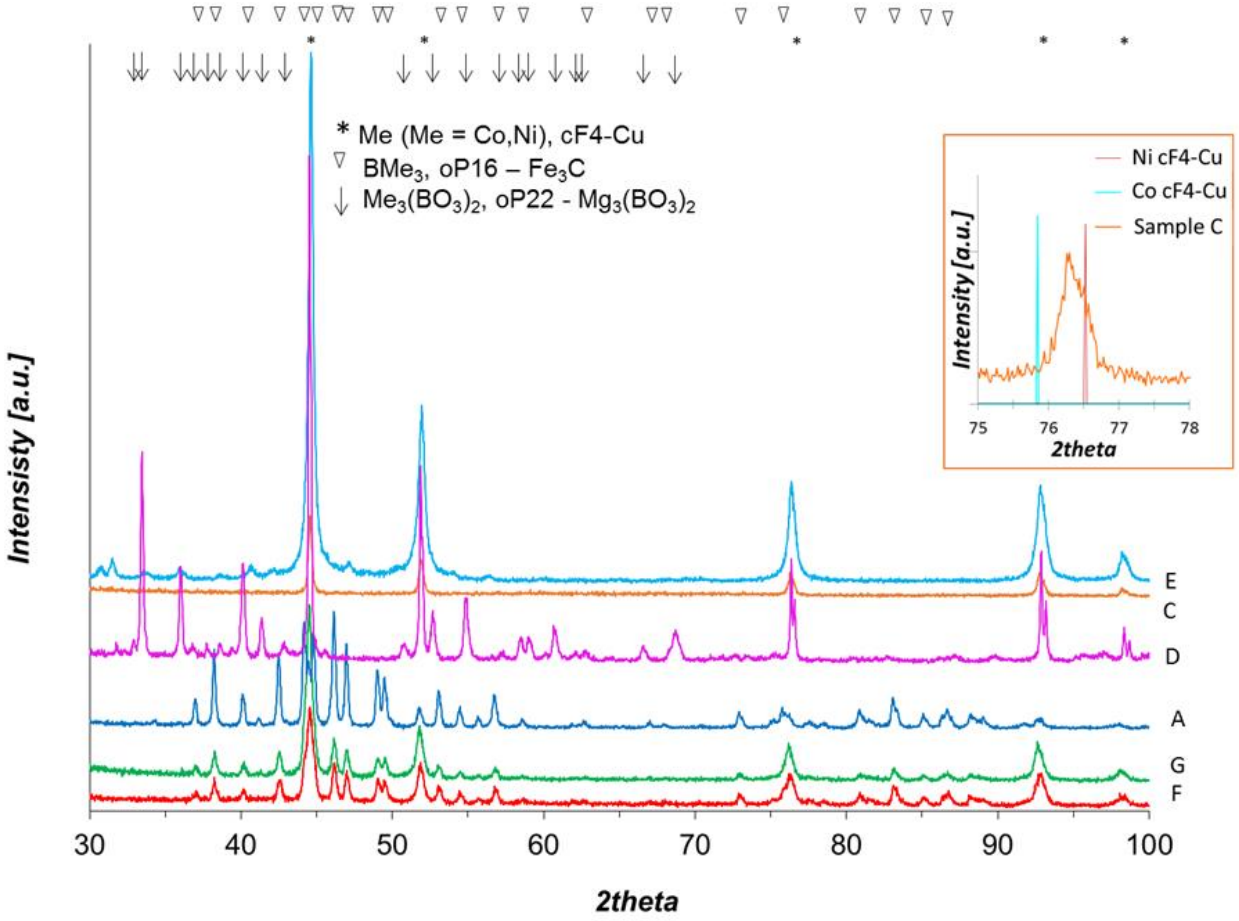

Figure 4.1: XRD of annealed sample under investigation. In the inset, the peak at 2theta=76.3° has been magnified, showing the formation of the alloy between Ni and Co.

FE-SEM micrograph identifies (Co,Ni) NPs of the order of 50 nm (not shown here) with a Co/O=Ni/O≈ 0.2 atomic ratio, obtained by EDX, demonstrating again the compresence of both metals and the quite high oxygen content, suitable with the results coming from other techniques. The high oxygen presence is confirmed by the presence of borates by IR spectroscopy (Figure 4.2) characterized by the features in the region 1500-1200 cm^{-1} and 900-700 cm^{-1} due to borates with different configurations (i.e. planar and tetrahedral) [18,19,20]. Planar BO_3^{3-} groups are characterised by asymmetric and symmetric B-O stretching in the 1500-1200 cm^{-1} and 1000-900 cm^{-1} regions respectively; instead, in-plane and an out-of-plane bending modes are found near 740 and 650 cm^{-1}.

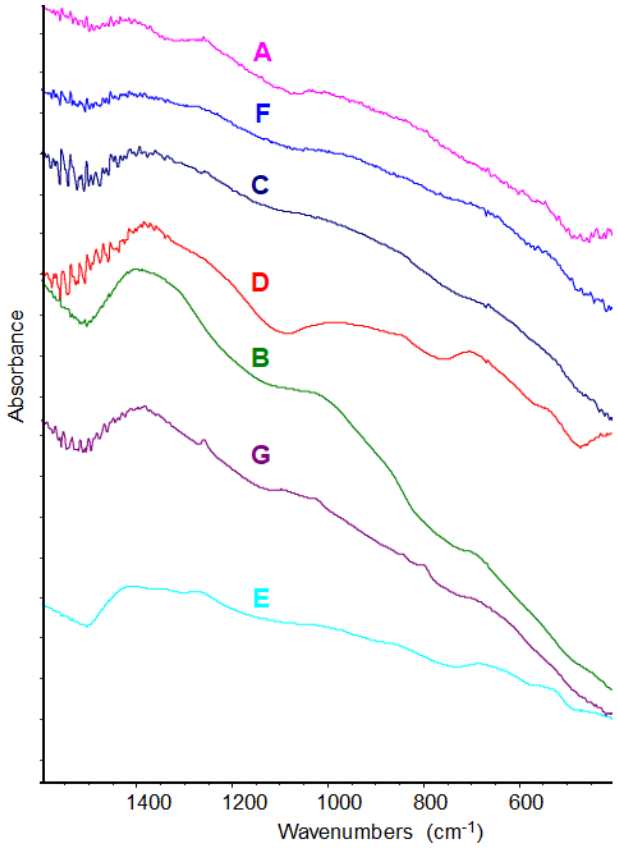

Figure 4.2: IR spectra of fresh investigated catalysts in the characteristic skeletal region (1600-400 cm^{-1})

Tetrahedral borate species have characteristic asymmetric and symmetric B-O stretchings in the region 1100-900 cm^{-1} [198, 19]. Similar features have been also found for nanosized Cobalt catalysts for the $NaBH_4$ hydrolysis [20], for the unsupported [2, 17] and for supported CoNPs [17].

4.2.2 *Separation, behavior and characterization of catalysts C and E, separated by filtration and successive washing in deionized water for three times*

The separation of the (Co,Ni) NPs from the reaction medium has been performed through filtration and successive washing in deionized water for three times. Then (Co,Ni) NPs were dispersed in 20 ml of absolute ethanol (>99.8%) and sonicated under Argon flow for 1 minute, in order to convert all eventual borides to borate species and thus enhancing the production of amorphous (Co,Ni) metallic NPs. Two samples have been prepared and characterized to evaluate data reproducibility. In this case, the XRD pattern of the annealed samples (Figure 4.1) shows only the characteristic

peaks of metallic (Co,Ni) cubic alloy. A representative peak (2theta=76.3°) has been magnified in inset of Fig. 4.1 showing that the maximum is in-between the peaks of pure annealed Co and Ni metals.

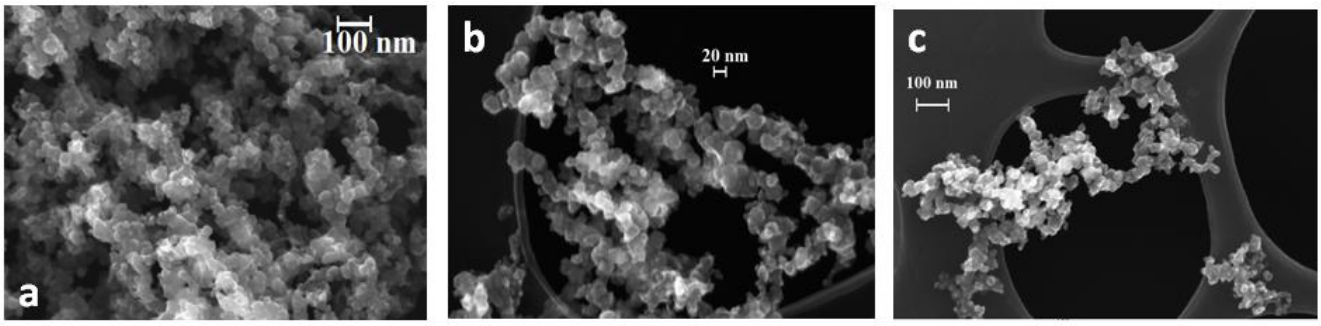

Figure 4.3: FE-SEM micrographs in secondary electrons for representative samples: C (3a), B (3b) and G (3c).

In Figure 4.3, FE-SEM micrographs show (Co,Ni) NPs with a maximum diameter of ≈20 nm; their composition has been obtained by SEM-EDX analysis and has been quantified by a Co/Ni=1 and a Co/O= Ni/O= 2.0 (average on 10 spots) atomic ratio, for both samples. HAADF-STEM images confirmed the morphology observed at FE-SEM (Fig. 4.4a).

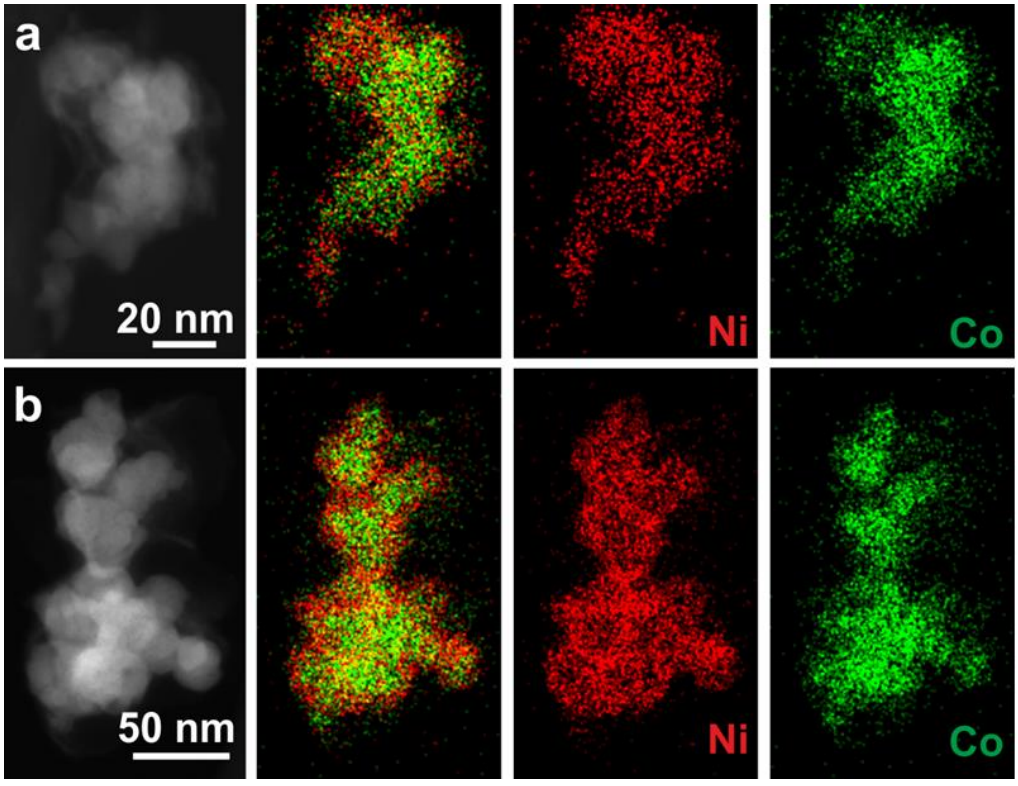

Figure 4.4: HAADF-STEM images and corresponding STEM-EDX maps of Co and Ni for samples (a) C and (b) B.

The STEM-EDX elemental maps show a slightly Ni-richer surface and a Co-rich core of the NP agglomerates. Moreover, elemental quantification carried out by STEM-EDX (three areas including a large number of NPs) indicates the presence of B (B/Co=0.42), and the atomic ratio between Co and Ni inside the nanoparticles (Ni/Co=0.99), thus confirming the achievement of the proper stoichiometric ratio. The results of IR analysis (see Fig. 4.2) confirm, for both samples, the goodness of our method showing the typical features of borates species with a lower intensity than that observed in the previous case(sample D).

4.2.3 Separation, behavior and characterization of catalyst B, separated by filtration and successive washing in deionized water for ten times.

The separation of the (Co,Ni) NPs from the reaction medium has been performed through filtration and successive washing in deionized water for ten times, in order to remove all the anions and cations from the reducing agent and salt precursor, i.e. Na^+ and Cl^-. Then the sample has been dried under dynamic vacuum. The annealed sample (Fig. 4.1) shows the characteristic diffraction pattern of the orthorhombic BMe_3 (Me=(Co,Ni) oP16, Fe_3C) together with the features of cubic metallic (Ni,Co) solid solution (cF4-Cu type). The BMe_3 presence might be explained by taking into account the complex solid state reactions network (reaction 1 and 2) reported in the literature [21,22] occurring at 773 K and in inert atmosphere for Co based materials, supposing that also Ni gives rise to the same reactions pathways (1 and 2, where Me=Co, Ni).

$2Me_2B + Me(BO_2)_2 \rightarrow 5Me + 2B_2O_x$ (1)

$Me_2B + Me \rightarrow Me_3B$ (2)

FE-SEM micrograph (Fig. 4.3b) identifies (Co,Ni) NPs with a maximum diameter of 20 nm and with a Co/O=0.8 and Ni/O=0.5 atomic ratio, obtained by SEM-EDX analysis. HAADF-STEM images confirmed the morphology observed at FE-SEM (Fig. 4b) and also the spatial distribution of Co and Ni over the NPs observed in the sample C.

Elemental quantification carried out by STEM-EDX indicates the presence of a higher B content compared to sample C (B/Co=B/Ni≈1), also confirmed by the absorbance value of the borates peaks measured at IR, and the achievement of the proper stoichiometric ratio between Co and Ni inside the nanoparticles (Ni/Co=1).

In Figure 4.2, IR spectra of fresh sample B is reported and the typical feature for borates are still well detectable according to the fingerprint bands at 1400, 1100 and 950 cm^{-1}. The band at 1400 cm^{-1} has a comparable absorbance to the one of C.

4.2.4 Separation, behavior and characterization of catalysts A, F and G, separated by filtration and successive washing in deionized water for three times and dried under dynamic vacuum

The separation of the (Co,Ni) NPs from the reaction medium has been performed through filtration and successive washing in deionized water for three times and dried under dynamic vacuum, in order to prevent NPs oxidation. In this case, the preparation have been performed for three different concentration ratios between Co(II) and Ni(II) chloride salts: 1:1 for sample A, 2:1 for sample F and 4:1 for sample G, always preserving the final concentration of 10^{-2} M for metals in solution, with a ratio Me^{2+}:BH_4^- equal to 1:2. The different stoichiometric ratios have been chosen in order to study the effect of the different Ni/Co ratio on the catalytic activity.

In Figure 1 (samples F and G), the annealed samples show the same peaks BMe_3 (Me=(Co,Ni) oP16, Fe_3C) together with the features of cubic metallic (Co,Ni) solid solution (cF4-Cu type). In this case, the sample seems to be enriched in the cubic metal phase with respect to sample B that are similar to the pattern of A (not reported, since good data reproducibility as evidenced for E and C). In Figure 3d, FE-SEM micrograph of sample G (reported as meaningful example) identifies (Co,Ni) NPs with a maximum diameter of 20 nm and with a Co/O=Ni/O≈3 ratio, obtained by SEM-EDX analysis. This datum well compare with the IR analysis (Figure 4.2) that shows relatively broad features for borates species.

Elastically-filtered (zero-loss) TEM and HAADF-STEM images of these samples (Figure 4.5 a,b,c), respectively, confirm the morphology observed by FE-SEM. Elemental quantification indicates, for all the three samples, the presence of a high B content (B/Co=B/Ni=1) and the Co/Ni atomic ratio within the nanoparticles (Ni/Co=1 for A, assessed by STEM-EDX, and Ni/Co=0.26 for G and Ni/Co=0.52 for F, the latter two assessed by EELS).

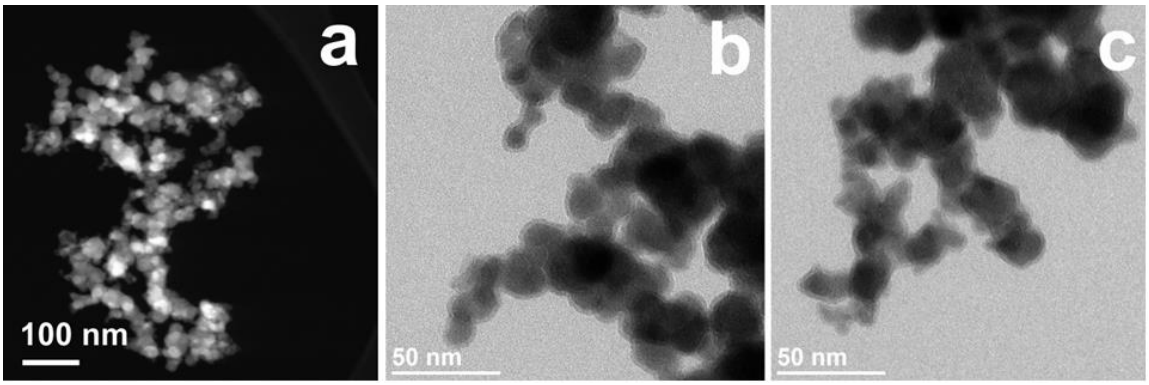

Figure 4.5: (a) HAADF-STEM image of sample A and (b,c) elastically filtered (zero-loss) TEM images of samples (b) F and (c) G.

4.3 Magnetic measurements

In Figure 4.6, the room temperature magnetic hysteresis cycles of two representative samples, namely E and A, are reported. Both samples display the same anhysteretic behavior with no saturation magnetization reached at the highest explored field ($\mu_0 H$ = 5 Tesla). Very low values of the coercive field are reached for the two samples, namely 2 Oe (0.2 mT) and 9 Oe (0.9 mT) for samples E and A, respectively. Both systems are, thus, in the superparamagnetic regime, confirming the very small dimensions of the nanoparticles.

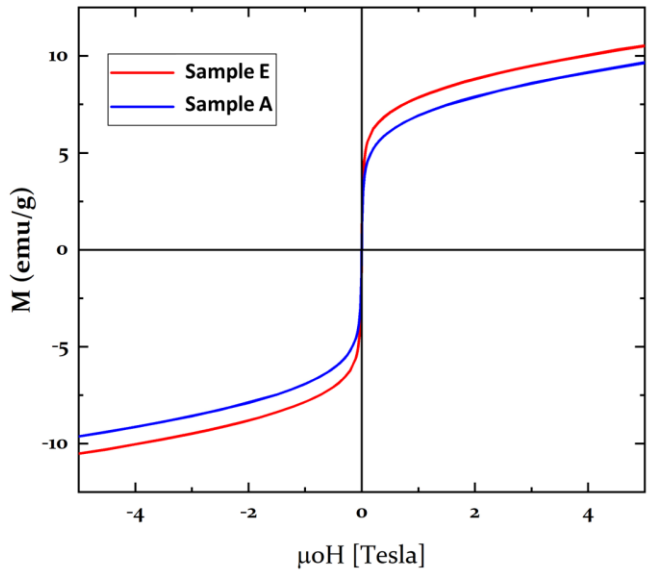

Figure 4.6: Room temperature magnetic hysteresis cycles of E and A samples.

4.4 Catalytic activity results

4.4.1 Effect of borate species on catalytic activity

In order to evaluate the effect of borates on the catalytic activity of (Ni,Co) NPs the catalytic behavior of the following samples A, B, D and E, all with a Ni/Co ratio ≈ 1 but separated with different procedures, will be compared, after tests at a GHSV of 324000 h^{-1}. It has to be remarked that the following order, in terms of borates concentration on the fresh samples, has been evaluated by means of IR spectroscopy (Figure 2): D > E > A > B).

In Table 4.2, the catalytic activity of the sample D is summarized. This sample, according to XRD on the annealed sample, contains both crystalline borate and the metals solid solution.

Table 4.2: Catalytic activity of sample D in ESR at GHSV 324000 h^{-1}, ethanol and water conversion, hydrogen yield and selectivities to carbon products.

T (K)	X C_2H_6O	X H_2O	Y H_2	S CH_4	S CO	S CO_2	S CH_2CH_2	S CH_3COH	S CH_3COCH_3	S $(CH_3CH_2)_2O$
523	1%	0%	0%	0%	0%	0%	0%	100%	0%	0%
573	15%	0%	3%	2%	3%	0%	0%	95%	0%	0%
673	100%	16%	44%	29%	32%	31%	2%	5%	1%	0%
773	100%	32%	69%	21%	12%	68%	0%	0%	0%	0%
673	83%	15%	39%	21%	20%	39%	3%	16%	0%	0%
573	15%	1%	3%	4%	6%	6%	0%	80%	0%	4%
523	3%	0%	1%	0%	0%	0%	0%	100%	0%	0%

By looking at the catalytic activity, it has a limited ethanol conversion at low temperature (i.e. 1% at 523 K) with acetaldehyde as the only detectable product, produced by ethanol dehydrogenation.

(3) $CH_3CH_2OH \rightarrow CH_3CH{=}O + H_2$

A temperature increase (573 K) produces an increased ethanol conversion with the presence of acetaldehyde, methane and CO, being produced by ethanol catalytic decomposition.

(4) $CH_3CH_2OH \rightarrow CH_4 + CO + H_2$

likely with the intermediate formation and further decomposition of the same acetaldehyde

(5) $CH_3CH{=}O \rightarrow CH_4 + CO$

At 673 K, ethanol is completely converted and a hydrogen yield of 44% is achieved, with methane, CO and CO_2 selectivities of ~30% each, suggesting that both ethanol decomposition (4) and ethanol steam reforming (ESR, 6) are occurring.

(6) $CH_3CH_2OH + 3\ H_2O \rightarrow 2\ CO_2 + 6\ H_2$

Small amounts of acetaldehyde and acetone are also observed suggesting that ethanol dehydrogenation reaction (4) still occurs while aldol condensation of acetaldehyde followed by dehydrogenation and decarbonylation also occurs to some extent. A further temperature increase to 773 K produces an increased CO_2 selectivity by a faster ESR reaction and a maximum hydrogen yield of 69%. A slight deactivation is observed when comparing the ascending and descending temperature experiments, suggesting that carbon deposition may occur resulting in deactivation of ethanol decomposition more than ESR. However, at 573 and 523 K the situation is similar to the one reported for the increasing temperature experiments with acetaldehyde as the main product.

The sample E after annealing is mainly composed by the cubic (Ni,Co) alloy, as discussed in paragraph 4.2, while the as cast sample presents the characteristic features of surface borates when characterized through FT-IR. In this case, the catalytic activity, summarized in Table 4.3, is similar to the one reported for D at 523 and 573 K while at 673 K ethanol conversion is still far from 100% (i.e. 93%) and hydrogen yield approaches 40%.

Table 4.3: Catalytic activity of sample E in ESR at GHSV = 324000 h^{-1}, ethanol and water conversion, hydrogen yield and selectivities to carbon products.

T (K)	X C_2H_6O	X H_2O	Y H_2	S CH_4	S CO	S CO_2	S CH_2CH_2	S CH_3COH	S C_3H_6O
523	4%	0%	1%	0%	0%	0%	0%	100%	0%
573	13%	0%	2%	3%	4%	0%	0%	93%	0%
673	93%	13%	39%	28%	34%	27%	0%	10%	2%
773	100%	31%	65%	24%	10%	66%	0%	0%	0%
673	81%	12%	33%	26%	26%	30%	2%	16%	1%
573	15%	0%	3%	6%	8%	2%	0%	84%	0%
523	4%	0%	1%	2%	3%	2%	0%	93%	0%

At the maximum reaction temperature, a hydrogen yield of 65% is obtained and some deactivation is again present in the decreasing temperature experiment.

The catalytic activity of sample B is summarized in Table 4.4.

Table 4.4: Catalytic activity of sample B in ESR at GHSV 324000 h^{-1}, ethanol and water conversion, hydrogen yield and selectivities to carbon products.

T(K)	X C_2H_6O	X H_2O	Y H_2	S CH_4	S CO	S CO_2	S CH_3CHO	S C_3H_6O
523	18%	0%	3%	4%	6%	1%	89%	1%
573	28%	1%	6%	3%	6%	3%	88%	0%
673	97%	17%	48%	24%	36%	32%	7%	1%
773	100%	36%	75%	17%	8%	75%	0%	0%
673	83%	14%	39%	18%	27%	31%	22%	1%
573	8%	0%	2%	4%	6%	3%	87%	0%
523	4%	0%	1%	0%	0%	0%	100%	0%

Despite the same applied conditions, in this case, a remarkable ethanol conversion is already obtained at 523 K with acetaldehyde as main product (89% selectivity) together with CO and methane (6% and 4% selectivities, respectively) as by-products. As observed in all other cases, ethanol conversion increases by increasing the reaction temperature but, in this case, a slightly higher hydrogen yield (75%) is obtained mainly at the expenses of methane and CO selectivities. By lowering the reaction temperature at 673 K, the catalyst loses 10% of its catalytic activity and again this is assignable to the reduced ethanol decomposition activity, since the constant value observed for CO_2 selectivity. Below 673 K, ESR activity is nil (at 573 K, 6% CO_2 selectivity) and the main reaction is again the dehydrogenation of ethanol to acetaldehyde and its further decomposition.

The sample showing the lowest amount of borates (A, Table 4.5) is even more active at low temperature in the production of acetaldehyde, CO and CH_4 (32% ethanol conversion) but its activity it is slightly reduced at 573K (10% ethanol conversion) with an analogous products distribution.

Table 4.5: Catalytic activity of sample A in ESR at GHSV 324000 h^{-1}, ethanol and water conversion, hydrogen yield and selectivities to carbon products.

T(K)	X C_2H_6O	X H_2O	Y H_2	S CH_4	S CO	S CO_2	S CH_2CH_2	S CH_3CH_3	S CH_3CHO	S C_3H_6O
523	32%	0%	6%	5%	8%	1%	0%	0%	85%	1%
573	10%	0%	2%	3%	6%	2%	0%	0%	89%	0%
673	71%	10%	30%	14%	27%	23%	1%	0%	34%	1%
773	100%	39%	81%	12%	7%	81%	0%	0%	0%	0%
673	55%	22%	22%	20%	40%	17%	1%	2%	20%	1%
573	13%	0%	3%	4%	8%	4%	0%	0%	84%	0%
523	2%	0%	0%	1%	2%	0%	0%	0%	96%	0%

At 673 K, the conversion has the worst values (71%) among the compared catalysts due mainly to the lowered activity in acetaldehyde decomposition reaction. An opposite situation is observed at the maximum tested temperature where the best hydrogen yield is observed (82%). In the decreasing temperature experiments, the observed catalytic behavior is similar to the one reported for the other samples with a non-negligible deactivation for the investigated system as already reported of Co [17].

The comparison of the data concerning samples D, E, B and A, shows, according to IR analysis, a decrease of the amount of borate species (D > E > B > A), and a roughly inversed steam reforming activity at 773 K (H_2 yields 68% ≈ 65% < 75% < 81%, for D, E, B and A, respectively). Thus, a negative role for the presence of borate species is confirmed. The same trend is also found for ethanol conversion at 523 K (0.8 % (D) < 4.0 % (E) < 18.0 % % (B) < 32.4 % (A)) where acetaldehyde is by far the main product in all cases. This suggests that the sites allowing acetaldehyde dehydrogenation at low temperature can become sites for steam reforming at a temperature sufficiently high to activate water.

It seems interesting to compare the behavior of sample D, the richest in borates, with that of a very similar pure Cobalt sample (Ni free), reported in reference [3] (i.e. denoted as D). The comparison shows that a strong enhancement of catalytic activity at 673 K is achieved by substituting half of the Co amount with Ni. At this temperature, an ethanol conversion of 100% (Y_{H_2} =44%) is achieved with the bimetallic catalyst against the 60% for the monometallic Co NPs (Y_{H_2}=17%), with the main production of C1 gases (CO, CH_4 and CO_2, selectivities 30% approx.) and

the detection of extremely low amounts of acetaldehyde, which is instead the main product for bare CoNPs. A second effect can rely on the reduced deactivation observed upon the decreasing temperature experiment; in fact, by comparing the data at 673 K, bimetallic NPs reduce their activity by a 20% that rise up to 50% for monometallic Co NPs.

Again by comparing the behavior of these two borate-rich samples, hydrogen yield at the highest tested temperature is similar in the two cases and this is mainly due to the still uncomplete conversion of ethanol over monometallic borate-rich Co NPs that compensate the higher CH_4 selectivity observed for bimetallic borate-rich (Co,Ni) NPs. This might suggest that the addition of Nickel to the formulation of Co nanoparticles can partially overcome to the deactivation induced by the presence of borates, which can, on the other hand, protect the NPs from ageing in oxidant environment, i.e. open air, as discussed in the following paragraph.

4.4.2 Effect of B/Co ratio and of the presence of borides (samples C and B as synthetized and after ageing)

The effect of B/Co has been investigated by considering samples with the same Ni/Co ratio ≈1 and a comparable amount of borates as determined on fresh catalysts by means of IR spectroscopy. As previously reported, sample B is characterized by a B/Co atomic ratio ~ 1 and, after annealing, contains the cubic metal alloy and the boride BMe_3. After annealing, sample C shows only the characteristic cubic metal alloy solid solution, while the B/Co has been estimated to be ~ 0.43 on the fresh nanopowder.

Tables 4.4 and 4.6 report the catalytic activity data of samples B and C, respectively.

Table 4.6: Catalytic activity of sample C in ESR at GHSV 324000 h^{-1}, ethanol and water conversion, hydrogen yield and selectivities to carbon products.

T (K)	X C_2H_6O	X H_2O	Y H_2	S CH_4	S CO	S CO_2	S CH_2CH_2	S CH_3CHO	S C_3H_6O	S $C_4H_8O_2$	S CH_3COOH
523	38%	0%	7%	4%	6%	0%	0%	89%	1%	0%	0%
573	13%	0%	3%	3%	5%	3%	0%	88%	0%	1%	0%
673	94%	13%	42%	23%	43%	22%	1%	8%	1%	0%	1%
773	100%	29%	62%	25%	13%	62%	0%	0%	0%	0%	1%
673	83%	13%	38%	18%	32%	27%	1%	19%	2%	0%	1%

573	14%	0%	3%	4%	8%	4%	0%	82%	0%	2%	0%
523	4%	0%	1%	1%	2%	2%	0%	94%	0%	0%	0%

The catalytic activity of these two samples is similar, suggesting that the presence of metal boride phase has a negligible effect.

These two catalysts have also been tested after ageing, performed by leaving (Ni,Co) NPs in open air for 30 days. Ageing of sample C did not significantly change the IR spectrum, where the band assignable to borates at 1410 cm^{-1} did not change its absorbance. As reported in Table 4.7, compared to Table 4.6, the catalytic activity of sample C did not change significantly after ageing. In order to strengthen ageing process, the same catalyst has been exposed to ambient air at 473 K for 10 minutes; also in this case no modification of the IR spectrum and of the catalytic activity (not reported) have been observed.

Table 4.7: Catalytic activity of aged sample C in ESR at GHSV 324000 h^{-1}, ethanol and water conversion, hydrogen yield and selectivities to carbon products.

T (K)	X C_2H_6O	X H_2O	Y H_2	S CH_4	S CO	S CO_2	S CH_3CHO	S C_3H_6O
523	8%	0%	1%	3%	3%	1%	93%	0%
573	14%	0%	3%	3%	4%	1%	91%	0%
673	94%	12%	38%	26%	36%	23%	12%	1%
773	100%	34%	72%	18%	10%	72%	0%	0%
673	67%	8%	25%	18%	20%	23%	34%	1%
573	12%	0%	2%	3%	4%	4%	88%	0%
523	3%	0%	1%	2%	2%	3%	91%	0%

A complete different situation is observed in the IR spectrum of the catalyst B, where a drastic increase of the band at 1410 cm^{-1} is evident after ageing (Fig. 4.7), and also results in a strong decrease of catalytic activity (not reported here).

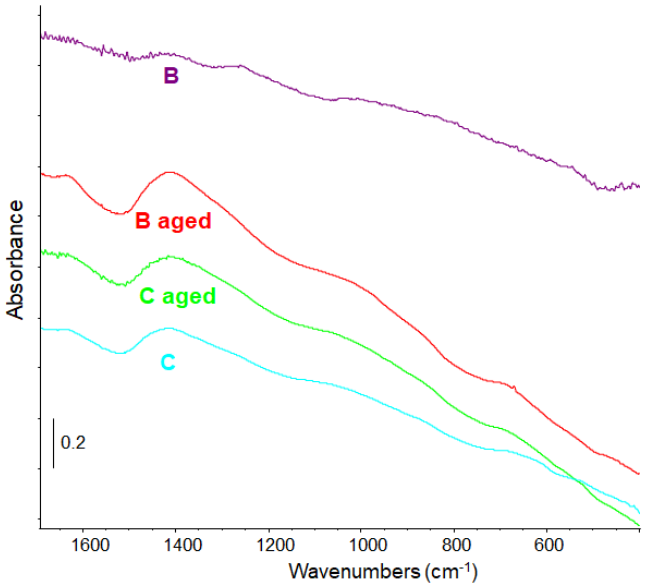

Figure 4.7: IR of fresh and aged B and C samples

The behavior of sample C suggests that, despite the lower catalytic activity of borate containing (Ni,Co) NPs, a protective effect can be played by surface borate in avoiding ageing of nanoparticles (e.g. irreversible poisoning).

Thus, as already reported for CoNPs, the presence of boron in the form of borates in the fresh nanoparticles has an evident negative effect (reduction of ethanol conversion and hydrogen yield) in the catalytic activity while a positive one is evidenced in the reduced ageing of this materials when aged or manipulated in a non-controlled atmosphere. On the other hand, the presence of boride species does not influence negatively the catalytic activity, but the catalyst is more prone to deterioration by ageing.

4.4.3 Effect of Ni/Co ratio (samples A, F and G).

To evaluate the effect of Ni/Co ratio, catalysts with the same B/Co ratio and quite comparable borates content have been considered. The compared samples are: A (Ni/Co=1), F (Ni/Co=0.52) and G (Ni/Co=0.26). Additionally, Ni-free Co sample from our previous work (sample A labeled in [3) is also taken into account, while data on a Co-free Ni sample are considered, also reported previously [1].

In Table 4.8, the data for sample G are reported.

Table 4.8: Catalytic activity of sample G in ESR at GHSV 324000 h^{-1}, ethanol and water conversion, hydrogen yield and selectivities to carbon products.

T (K)	X C_2H_6O	X H_2O	Y H_2	S CH_4	S CO	S CO_2	S CH_2CH_2	S CH_3CHO	S C_3H_6O
523	5%	0%	1%	0%	0%	0%	0%	100%	0%
573	13%	0%	2%	3%	5%	0%	0%	92%	0%
673	100%	13%	41%	30%	39%	25%	2%	3%	2%
773	100%	43%	87%	9%	3%	88%	0%	0%	0%
673	88%	10%	34%	23%	32%	21%	1%	9%	0%
573	15%	0%	3%	5%	8%	2%	0%	85%	0%
523	4%	0%	1%	0%	0%	0%	0%	100%	0%

The comparison with the data concerning sample A (Table 4.5) shows that sample G is definitely more active at any temperature, with higher performances in ESR at 773 K, providing 87 % yield in H_2 at 773 K. This sample also shows full selectivity to acetaldehyde at 523 K, but high selectivities to methane (23-30 %) at 673 K. The data concerning sample F (not shown) are intermediate between those of samples A and G. If compared with Co-free Ni NPs [1], catalyst G appears to be definitely more selective to ESR, with lower methane production. In contrast, if compared with Ni-free Co NPs [3] sample G is more active with a lower acetaldehyde production. It seems that the (Co,Ni) bimetallic nanoparticles may improve the catalytic behavior, with a reduction of the ethanol (or acetaldehyde) decomposition activity of nickel, and an improving of the activity of cobalt.

In order to further check the role of Nickel in the bimetallic formulation, the GHSV has been reduced by a factor five (from 324000 h^{-1} to 51700 h^{-1}), and experiments have been reported for 523 K. As previously reported for Co NPs [3], a decrease of space velocity is not affecting high temperature performances, while a strong effect is detectable at low temperature suggesting that, also in this case, the experiments are conducted in a proper kinetic regime. In these conditions, ethanol conversion that is 0% for Co NPs, rises at 42% for (Co,Ni) NPs (Ni/Co =0.26) and is 92% for Ni NPs [1]. However, a complete change in product distribution is also observed in these conditions (see Figure 4.8): for (Co,Ni) NPs the main products, with an almost complete selectivity, is acetaldehyde with a small coproduction of CO and CH_4, while for Ni NPs the main products are methane and CO while yield to acetaldehyde is found to be lower than 12%. This

further confirms that Ni addition may increase catalytic activity of monometallic Co NPs. Monometallic CoNPs do not catalyze ethanol decomposition at low temperature; this reaction is faster on Ni catalysts.

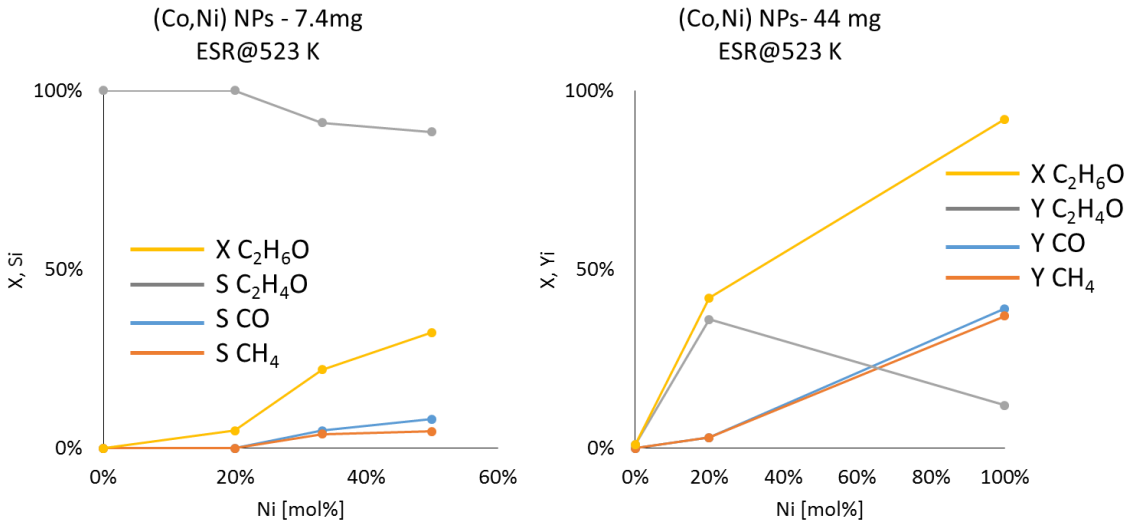

Figure 4.8: Effect of gas space velocity and Ni content in (Co,Ni) NPs in ESR condition at 573 K

4.5 *Characterization of the catalytic materials after catalysis.*

After catalysis, the exhaust catalysts have been characterized by means of XRD and FE-SEM.

In Figure 4.9, the diffractograms of representative catalysts after increasing and decreasing temperature experiments are reported.

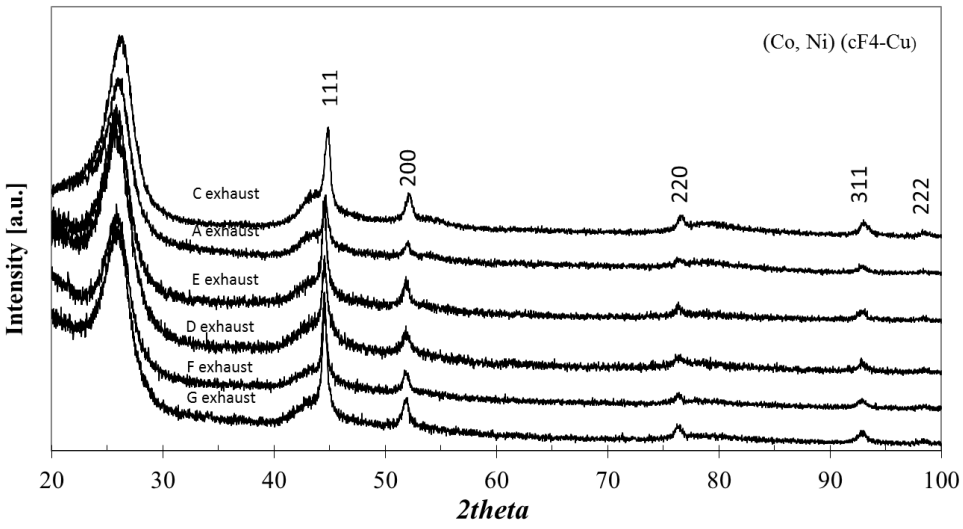

Figure 4.9: XRD of exaust samples

It is possible to distinguish for all of them two different crystalline phases; the former one is the (Co,Ni) solid solution with a cubic structure (cF4-Cu) while the latter is assignable to the presence of graphitic carbon (2theta=25° and 44°). According to our previous studies on unsupported Co [3] and Ni [1] nanoparticles, the XRD of the exhaust catalysts present the Cubic structure for Co while a metastable hexagonal (hcp) structure, stabilized by the presence of Carbon, for Ni. However, according to the present study, bimetallic (Co,Ni) NPs are found with the cubic structure with no evidence of Ni hcp structure, supporting the formation of a solid solution, between the two metals. Representative FE-SEM micrographs are shown in Figure 4.10, where it is possible to identify well dispersed nanoparticles in a matrix of carbon nanotubes.

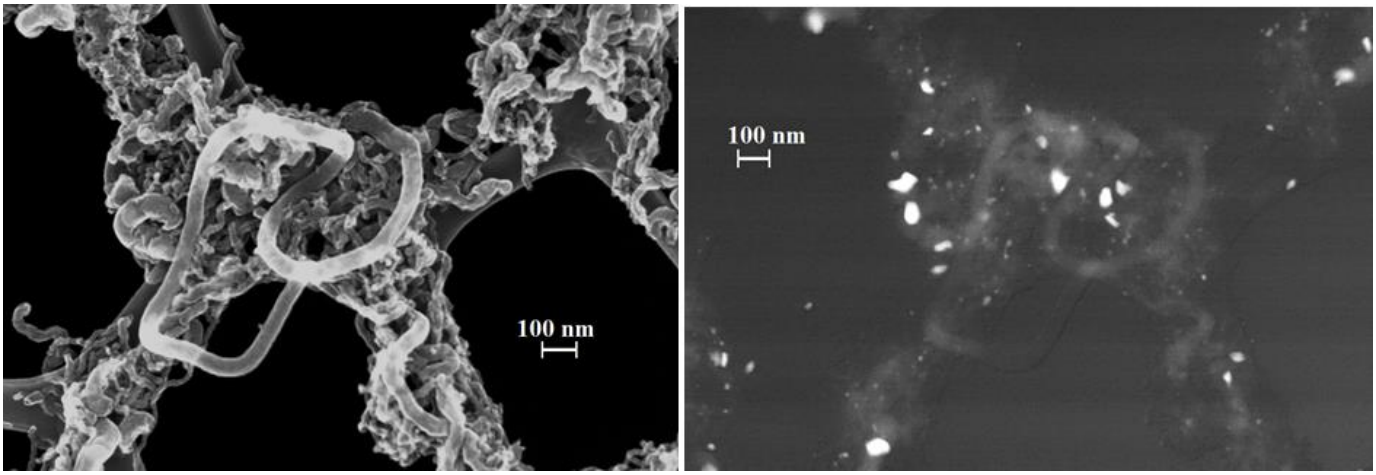

Figure 4.10: FE-SEM micrographs of a representative exaust sample (G): image acquired collecting secondary electrons on the left and back-scattered electrons on the right.

Also SEM-EDX analysis on bright particles (as observed in figure 10 (right) with BSE signal) reveals after catalytic tests the co-presence of both Ni and Co, suggesting that no preferential rearrangement (i.e. preferential growth of carbon on Ni, with sequential segregation) occurs in this case.

4.6 Conclusions

The data described and discussed above allow to obtain the following conclusions:

1. The reduction of Ni and Co chlorides by sodium borohydride allows to produce (Co,Ni) bimetallic nanoparticles with a quite homogeneous particle size of about 20 nm. These particles, originally amorphous, crystallize into the cubic structure (cF4-Cu) solid solution alloy after annealing in inert atmosphere.
2. The washing and separation procedures leave boron impurities in the sample. The separation procedure and thermal treatments determines the amount and state of boron impurities, mainly in the form of borates or borides.
3. The bimetallic nanoparticles are active in ethanol conversion in the presence of steam. The presence of boron impurities, however, affects the catalytic activity. The presence of borate species is associated to weaker catalytic activity. However, the catalysts can be aged without losing activity. Reversely, the presence of borides does not affect activity but is associated to catalysts that lose activity upon ageing.
4. For low Boron catalysts, the addition of Nickel to Cobalt nanoparticles improves the catalytic activity in ethanol steam reforming allowing yields as high as 87 % at 773 K, at high space velocities (GHSV 324000 h^{-1}).
5. In particular, the addition of Ni to Co increases catalytic activity while the presence of Co reduces the tendency of Nickel to produce methane by ethanol decomposition. Consequently, the sample with Ni/Co = 0.26 appears to be a better catalyst than pure Ni and pure Co, with very high activity at very low contact times. The performances of these catalytic unsupported nanoparticles appear to be better than those of conventional supported catalysts.
6. Carbonaceous materials, such as carbon nanotubes and graphitic carbon, form on the catalyst surface upon reaction.
7. Metallic particles are active in ESR even without any support. This implies that the surfaces of both nickel and cobalt particles, and their alloys, possess in reaction conditions the functionalities for activating both water and ethanol. The effect of the supports is most likely an indirect one, modifying the physical properties of the metal particles.

4.7 References

[1] P. Riani, G. Garbarino, M. A. Lucchini, F. Canepa, G. Busca J. Mol. Catal. A: Chem. 383– 384 (2014) 10– 16.

[2] G. Garbarino, P. Riani, M.A. Lucchini, F. Canepa, S. Kawale, G. Busca, Int J Hydrogen Energ 38 (2013) 82-91.

[3] P. Riani, G. Garbarino, A. Infantes-Molina, E. Rodríguez-Castellón, F. Canepa, G. Busca, Appl Catal A Gen 518 (2016) 67-77.

[4] P. Riani, G. Garbarino, F. Canepa, G. Busca, Cobalt nanoparticles mechanically deposed on α-Al_2O_3: a competitive catalyst for the production of hydrogen through ethanol steam reforming, J. Chemical Technology and Biotechnology, in press

[5] N. Bion, D. Duprez, F. Epron, ChemSusChem 5 (2012) 76–84.

[6] G. Nahar, V. Dupont, Biofuels 3 (2012)167-191.

[7] M. Aminul Islam, M. Anwarul Kabir Bhuiya, M. Saidul Islam, Asia Pac. J. En. Envir. 1 (2014) 107-121.

[8] C.J. Jia, F. Schüth, Phys. Chem. Chem. Phys. 13 (2011) 2457-2487.

[9] C. Resini, M. C. Herrera Delgado, S. Presto, L. J. Alemany, P. Riani, R. Marazza, G. Ramis, G. Busca, Int. J. Hydrogen Energy, 33 (2008) 3728-3735.

[10] G. Busca, U. Costantino, T. Montanari, G. Ramis, C. Resini, M. Sisani, Int. J. Hydrogen Energy, 35 (2010) 5356-5366.

[11] E. Moretti, L. Storaro, A. Talon, S. Chitsazan, G. Garbarino, G. Busca, E. Finocchio, Fuel 153 (2015) 166-175.

[12] Gharahshiran VS, Yousefpour M (2018) Int J Hydr En 43: 7020-7037.

[13] Rodriguez-Gomez A, Caballero A (2018) Mol Catal 449: 122-13.

[14] Soykal I, Bayrama B, Sohna H, Gawadea P, Miller JT, Ozkan US (2012) Appl Catal A Gen 449:47–58.

[15] Garbarino G, Wang C, Valsamakis I, Chitsazan S, Riani P, Finocchio E, Flytzani-Stephanopoulos M, Busca G (2015) Appl Catal B Environ174:21-34.

[16] Garbarino G, Chitsazan S, Phung TK, Riani P, Busca G (2015) Appl Catal A Gen 505:86-97.

[17] P. Riani, G. Garbarino, F. Canepa, G. Busca, Cobalt nanoparticles mechanically deposed on γ-Al_2O_3: a competitive catalyst for the production of hydrogen through ethanol steam reforming, J. Chemical Technology and Biotechnology, in press

[18] A. Delmastro, G. Gozzelino, D. Mazza, M. Vallino, G. Busca, V. Lorenzelli, J. Chem. Soc. Faraday Trans. 88 (1992) 2065-2070.

[19] D. Mazza, M. Vallino, G. Busca, J. Am. Ceram. Soc. 75 (1992) 1929-1934.

[20] V.I. Simagina, O.V. Komova, O.V. Netskina, Nanosized Cobalt Catalysts for Hydrogen Storage Systems Based on Ammonia Borane and Sodium Borohydride, in A. Gromov, U. Teipel, Metal Nanopowders: Production, Characterization, and Energetic Applications, (2014) 199-227.

[21] G.N. Glavee, K.J. Klabunde, C.M. Sorensen, G.C. Hadjapanayis, Langmuir 8 (1992) 771-773

[22] G.N. Glavee, K.J. Klabunde, C.M. Sorensen, G.C. Hadjapanayis, Langmuir 9 (1993) 162-169.

Chapter 5

Preparation of SiO_2 supported cobalt catalysts and their activity in ESR and CO_2 methanation

The CO_x hydrogenation reactions and the steam reforming reactions are essentially the inverse ones of the others. The "microreversibility principle" accounts for the good activity of materials based on the same active phase for both reactions. However, just because they are essentially inverse equilibrium reactions, ones of them (hydrogenations including methanations) are exothermic and must be carried out at low temperature (573-773 K), while the others (steam reforming processes) are endothermic and must be carried out at high temperatures (873-1173 K). Thus, the stability requirements for the catalysts are different.

On the other hand, catalysts for ESR should result in low methane coproduction. Methane production during ESR can come from methanation of CO and/or CO_2, a successive by-reaction, or by cracking of ethanol or acetaldehyde, essentially a parallel by-reaction. In previous studies carried out by our research group, Ni-based catalysts for both ESR [1] and CO_2 methanation was tested. In spite of the high activity of Ni-based catalysts in methanation, we concluded that they produce methane during ESR mainly through cracking of ethanol or acetaldehyde [2].

We also reported on cobalt-based catalysts for ESR and found that they frequently produce low amounts of methane. Our studies included unsupported cobalt nanoparticles [3,4], mechanically supported cobalt nanoparticles Co/α-Al_2O_3 [5], impregnated Co/γ-Al_2O_3 [6] and Co/CeO_2-ZrO_2 [7], coprecipitated Co/ZnO-Al_2O_3 [8] as promising catalysts for this reaction.

To go further on our investigations concerning ESR, CO_2 hydrogenation and cobalt based catalysts for these reactions, we prepared Co/SiO_2 catalysts using two different precursors and we tested them in both reactions. Silica was of an interesting support for us, because Co/SiO_2 was reported to be a good catalyst also for ESR [9] and silica is quite a stable material and is nearly inert against adsorption and activation of both ethanol and CO_2. This allows us also to evaluate the role of the reactants adsorption on the support in these reactions.

5.1 Experimental

Commercial Silica gel (Carlo Erba, S_{BET} 350 m^2/g) has been used as catalyst support after calcination at 823 K for 3 h. The synthesis of Cobalt based catalysts has been carried out by wet impregnation starting from different metals precursors ($Co(NO_3)_2*6H_2O$ and $Co(CH_3COO)_2*4H_2O$)) aqueous solution, keeping a total Co loading of 20 wt.%. The catalysts have been then dried at 373 K overnight and then calcined at 823 K for 3 hours. The notation for the samples will be the following: Co/SiO_2 (N) and Co/SiO_2 (A) for nitrate and acetate precursors, respectively.

Catalytic activity in Ethanol Steam Reforming was measured in a flow fixed-bed tubular glass reactor, loaded with 44.1 mg of catalyst mixed with 440 mg of silica glass particles (60-70 mesh sieved). The fed gas had the following composition 8.3% ethanol, 50.1% H_2O and 41.6% helium giving rise to GHSV values of 51700 h^{-1} calculated on the catalyst volume. The reaction temperature was varied as follows: 523 K → 573 K → 673 K → 773 K → 873 K → 973 K → 873 K → 773 K → 673 K → 573 K → 523 K, with the reaction held at each temperature for 1 h. The same experiment has been also stopped at 773 K in order to evaluate any effect of temperature higher than calcination ones (not reported), since the pretty similar behavior of the catalytic activity in the two cases.

Product analysis was performed with a gas-chromatograph Agilent 4890 equipped with a Varian capillary column "Molsieve 5A/Porabond Q Tandem" and TCD and FID detectors in series. Between them a nickel catalyst tube was employed to reduce CO_x to CH_4. Products analysis was also performed on GC/MS (FOCUS and ISQ from Thermo-Fisher), in order to have a precise identification of the compounds. The conversion of the reactants is defined as follows:

$$(1)\quad X_{\text{reactant}} = \frac{\text{nreact.in} - \text{nreact.out}}{\text{nreact.in}}$$

while selectivity to C-product *i* is defined as:

$$(2)\quad S_i = \frac{n_i}{\nu_i(\text{nreact.in} - \text{nreact.out})}$$

where n_i is the number of moles in compound i, and ν_i is the ratio of stoichiometric reaction coefficients. The hydrogen yield is defined as:

$$(3)\quad Y_{H2} = \frac{n_{H2\ out}}{6*(n_{ethanol\ in})}$$

For CO_2 methanation experiments, a tubular silica glass flow reactor, containing a fixed bed with 88.2 mg of catalyst mixed with 700 mg of silica glass particles 0.25–0.21 mm (corresponding to 60-

70 mesh sieved) was used in steady-state catalytic experiments. CO_2 hydrogenation experiments were conducted with the following feed gas: 6% CO_2, 30%H_2 and N_2 balance, used as carrier gas. The gas hourly space velocity GHSV was equal to 55000 h^{-1}. In order to follow any hysteresis, activation or deactivation effects, experiments were performed both in ascending and descending reaction temperature (523 K, 573 K, 623 K, 673 K, 723 K, 773K and reverse).

Online products analysis was performed using a Nicolet 6700 FT-IR instrument. Frequencies, where CO_2, CH_4 and CO molecules absorb weakly, were used (2293 cm^{-1} for CO_2, 2170 cm^{-1} for CO, 1333 cm^{-1} for CH_4, after subtraction of baseline) with previous calibration using gas mixtures with known concentrations, in order to have quantitative results. Produced water was condensed upstream of the IR cell. From the inlet and outlet concentrations calculated from the absorbances of CO, CO_2, CH_4 and the measured inlet and outlet total flows (which allow to take into account the variation of the number of moles during the reaction), CO_2 conversion (X_{CO_2}), selectivities and yields to products, S_i and Y_i, were calculated [10]. They are defined as:

$$X_{CO2} = \frac{F_{CO2\ in} - F_{CO2\ out}}{F_{CO2\ in}} \quad (4)$$

$$S_i = \frac{F_i}{F_{CO2\ in} - F_{CO2\ out}} \quad (5)$$

$$Y_i = \frac{F_i}{F_{CO2\ in}} \quad (6)$$

where F_i is the molar flow rate of i (i.e. CO and CH_4), while F_{CO_2} is the molar flow rate of CO_2 and they were all expressed in mol/min.

5.2 Results and discussion

5.2.1 Characterization of the fresh catalysts.

In Table 5.1, the elemental composition of the two catalysts, as obtained by EDX analysis, is reported. It closely corresponds to the virtual composition.

Table 5.1:

Notation	Precursor	Virtual composition Co wt.%	EDX composition Co wt.%
Co/SiO_2 (A)	acetate	20	22
Co/SiO_2 (N)	nitrate	20	21

In Figure 5.1, the XRD patterns of the as prepared samples are reported together with the diffractograms of the Co_3O_4 phase.

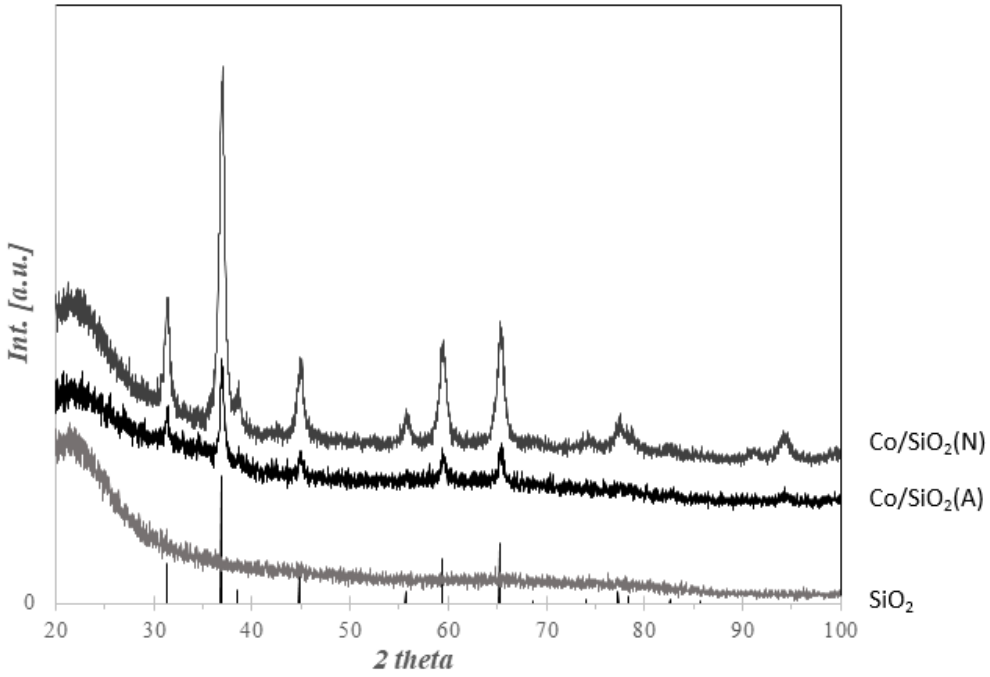

Figure 5.1. XRD patterns of the fresh catalytic materials.

The calcined silica support is still completely amorphous as expected for silica gel. The introduction of cobalt in the catalyst formulation produces the appearance in both cases of the pattern of the Co_3O_4 spinel phase. A rough evaluation of the average crystal size of the Co_3O_4 spinel phase using the Scherrer formula gives rise to ~ 15 nm particle diameter for sample N and ~ 22 nm particle diameter for sample A.

The IR spectra of bare silica calcined at 823 K and of the prepared catalysts are reported in Fig. 5.2 left.

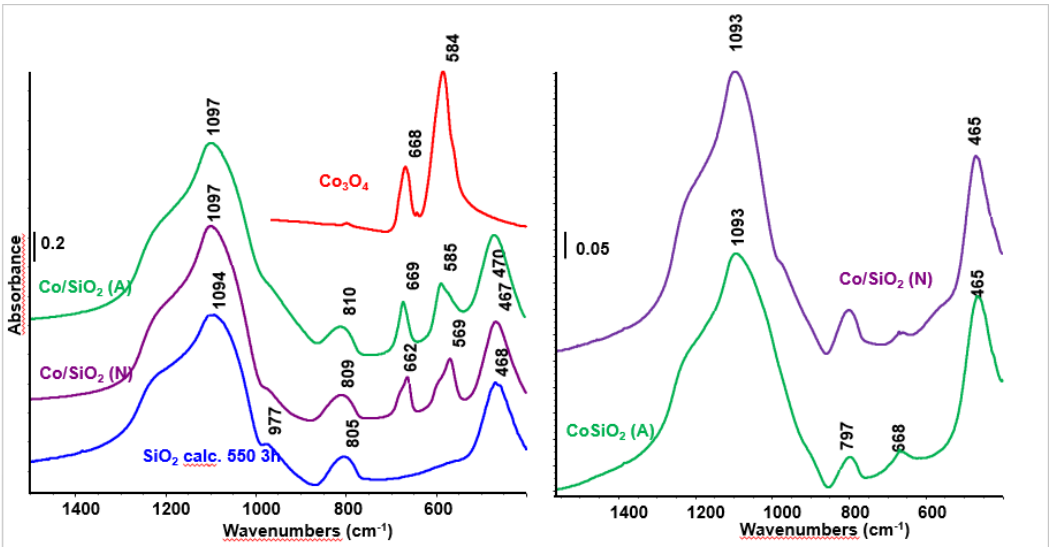

Figure 5.2. Skeletal FT-IR spectra (KBr pressed disks) of the fresh catalytic materials (left) and on exhaust catalysts after methanation (right).

The spectrum of the bare silica is characterized by the bands assigned to the Si-O-Si asymmetric stretching (ν_1 = 1094 cm^{-1} with the pronounced shoulder at 1230 cm^{-1}), the Si-O stretching of silanol groups SiOH (ca. 977 cm^{-1}), the Si-O-Si symmetric stretching/in plane bending (ν_2 = 805 cm^{-1}), and to the corresponding out of plane bending mode (ν_3 = 468 cm^{-1}), typical of amorphous silica [11].

The absence of bands in the region 1800-1300 cm^{-1} in the spectra of the as prepared catalysts confirms that both nitrate and acetate precursors have been effectively decomposed during the calcination procedure.

The IR spectra of the catalysts present the bands of silica and bands coming from cobalt species corresponding to the bands observed in the IR spectrum of Co_3O_4, also reported in the figure, in agreement with the literature [12,13,14]. In fact, the IR spectrum of spinel structures imply the existence of 39 optical mode that give rise to four triply degenerated IR active modes, two of which fall in the MIR (Mid infrared) region and two in the FIR (Far infrared) region at around 390-5 and 215-20 cm^{-1} (not recorded here). Both bands in the MIR region are split into two components, which can be attributed to TO / LO (transverse and longitudinal optical modes, respectively) components [13,14]. We find the maxima in the spectrum of our reference Co_3O_4 sample at 668 and 584 cm^{-1}, i.e. in intermediate positions with respect to those expected for TO and LO modes. It is in fact known that the transmission IR spectra of bulk particles are strongly dependent on the size, shape [15] and aggregation [16] of particles, that in fact modify the relative intensities and splittings of these polar

modes. In the case sample Co/SiO_2 (A) we find also the maxima almost in the same position (668 and 584 cm^{-1}), with clear shoulders at lower frequencies. In the case of sample Co/SiO_2 (N) the bands are located at lower frequencies (662 and 569 cm^{-1}), with clear shoulders at higher frequencies. In all cases, the bands observed are at intermediate position between those reported for LO modes (675, 595 cm^{-1}) and TO ones (655, 550 cm^{-1}) [14]. Interestingly, the spectrum we found for sample Co/SiO_2 (N) is very similar to that previously reported of a Co_3O_4/SiO_2 (SBA) mesoporous sample [17] prepared with the same cobalt precursor. The data suggest that Co/SiO_2 (N) and Co/SiO_2 (A) samples contain Co_3O_4 nanoparticles with two main crystal shapes in different relative amounts.

Looking at the bands of silica, the IR spectra of both catalysts show that the position of the Si-O-Si asymmetric and symmetric stretching bands of amorphous silica are slightly but significantly shifted upwards in the spectra of the Co/SiO_2 catalysts (1094 to 1097 cm^{-1}, 805 to 809,810 cm^{-1}), suggesting that quite a significant interaction occurred. The spectrum of silica is also significantly modified in the region 1050-800 cm^{-1}. To look better at this we analyzed the difference spectra (Fig. 5.3) obtained by subtracting the spectrum of calcined silica from those of the fresh catalysts.

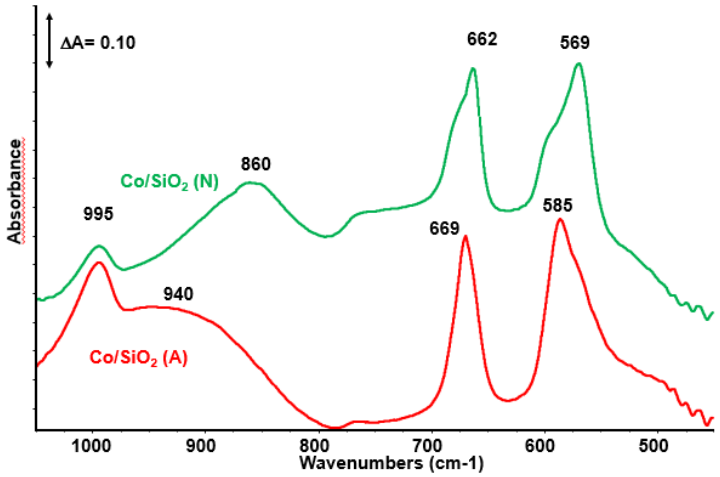

Figure 5.3. Subtractions of the silica spectrum from the skeletal FT-IR spectra (KBr pressed disks) of the fresh catalysts.

The subtraction spectrum relative to sample Co/SiO_2 (N) is consistent with a small shift of the Si-O-Si stretching bands as a predominant perturbation while the spectrum of sample Co/SiO_2 (A) presents a more evident perturbation with the strong growth of a sharp band at 995 cm^{-1} and of a broader one at 940 cm^{-1}. The position of these bands is compatible with the formation of terminal

silicate bonds, such as those of cobalt silicate species $\equiv O_3Si\text{-}O\text{-}Co^{2+}$ and / or $=O_2SiO_2=Co^{2+}$, similar to those present in the XRD patterns e.g. of Co_2SiO_4 [18].

The results arising from UV-vis-NIR spectroscopy on fresh catalysts are reported in Figure 5.4 left.

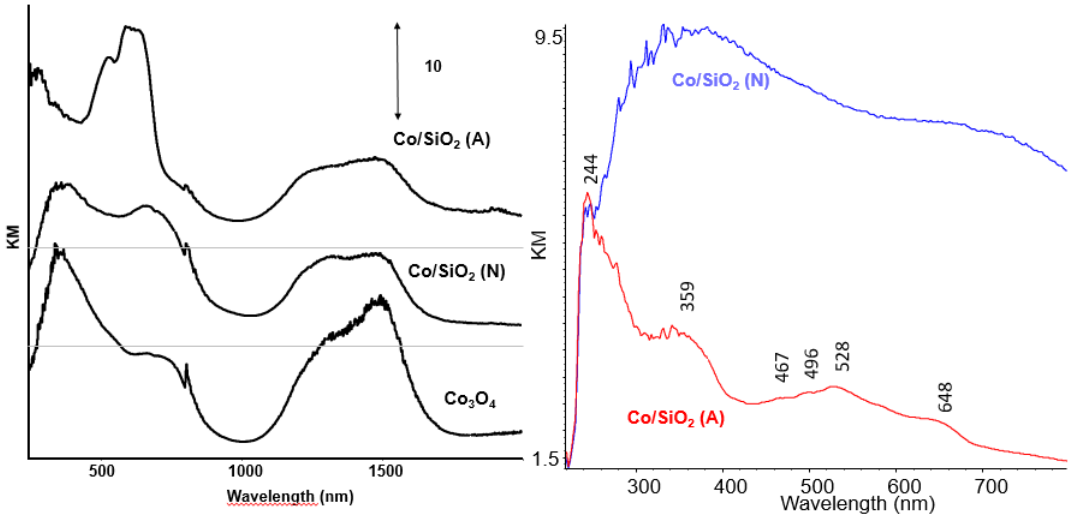

Figure 5.4. DR-UV-Vis-NIR spectra of the fresh catalytic materials left) and on exhaust catalysts after methanation (right).

The spectrum we recorded for bulk Co_3O_4 is consistent with those reported in the literature [19,20]. It presents a peak with maximum around 360 nm probably with a component at higher wavenumber around 415 nm, another component evident as a pronounced shoulder near 700 nm, and a broad doublet in the near region with a minor component around 1320 nm a the main maximum, possibly multiple, at 1495 nm. The complex maximum around 400 nm is assigned to the $p(O^{2-})\rightarrow e_g(Co^{3+})$ and $p(O^{2-})\rightarrow t_2(Co^{2+})$ "ligand to metal" charge transfer transitions which are nearly superimposed. The absorptions around 700 and 1320 nm are assigned to intercationic charge transfer transitions, i.e. $t_{2g}(Co^{3+})\rightarrow t_2(Co^{2+})$ and $t_2(Co^{2+}) \rightarrow e_g(Co^{3+})$ respectively. The components at around 1495 are associated to internal d-d transitions of Co^{2+} ions [19,20].

The spectrum of Co/SiO_2 (N) is closely similar to that of Co_3O_4, with only a difference in the relative intensities of the components, confirming that it contains essentially Co_3O_4 nanoparticles. Instead, the spectrum of sample Co/SiO_2 (A) is markedly different: it shows, probably superimposed to the same spectrum due to Co_3O_4 particles, a strong doublet at 527, 593 and 634 nm. Similar triplets are observed in the spectra of Co_2SiO_4 and $MgCoSiO_4$ (Olivine structure) [18], other crystalline cobalt silicates [21], in cobalt containing glasses [22], as well as for Co exchanged zeolites and silica-alumina [23, 24]. These absorptions are assumed to originate from three spin- allowed d-d transitions of Co^{2+}

($t_1g(^4F) \rightarrow {}^4t_2g(^4F)$, ${}^4t_1g(^4F) \rightarrow {}^4a_2g(^4F)$, and ${}^4t_1g(^4F) \rightarrow {}^4t_1g(^4P)$ [21]). In agreement with the IR spectra, the spectra in the visible region indicate that in the case of sample Co/SiO_2 (A), together with Co_3O_4 nanoparticles, isolated Co^{2+} species entered in the silica matrix, also exist.

In Figure 5.5, the FE-SEM micrographs of the silica gel and of the as prepared catalysts are reported.

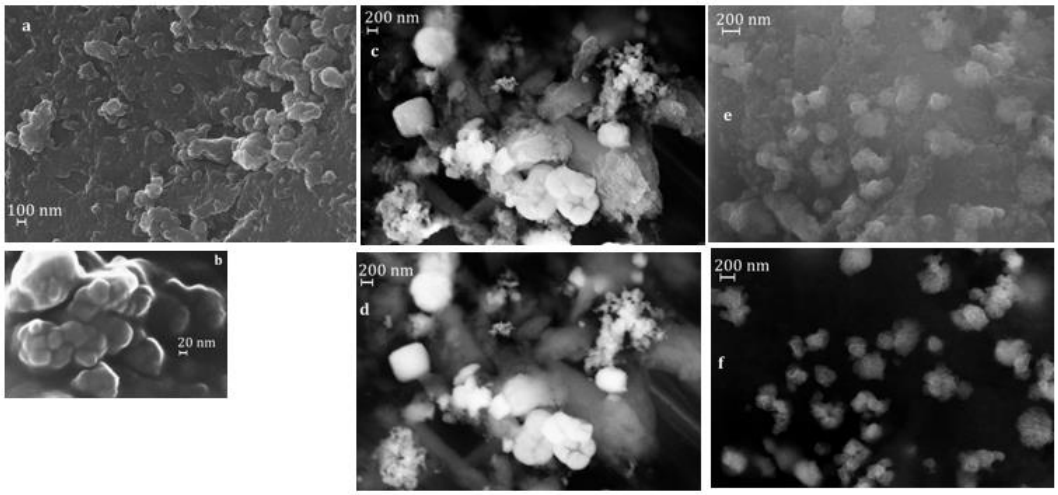

Figure 5.5. FE-SEM micrographs of the fresh catalytic materials (a) and (b): silica gel (different magnification); (c) and (d): sample A (Inlens and BSE respectively); (e) and (f): sample N (Inlens and BSE respectively).

The silica gel is constituted by squared or elongated smooth agglomerates about 20-200 µm large constituted by small globular particles with 20-200 nm diameter giving rise to a sponge-like structure (Fig. 5.5, a and b). The morphology of cobalt particles in sample Co/SiO_2 (A) (Figs. 5.5 c and d) is characterized by very small elemental particles (few tens of nm, in rough agreement with the data coming from XRD) sometimes associated into large aggregates of variable size and shape. In the case of sample Co/SiO_2 (N) (Figs 5.5, e and f), the small elemental particles are less evident while the aggregates with 100-200 nm size are more homogeneous.

5.2.2 Catalytic activity in CO_2 hydrogenation

In figure 5.6, the results arising from online analysis of the product gas after the hydrogenation reactor.

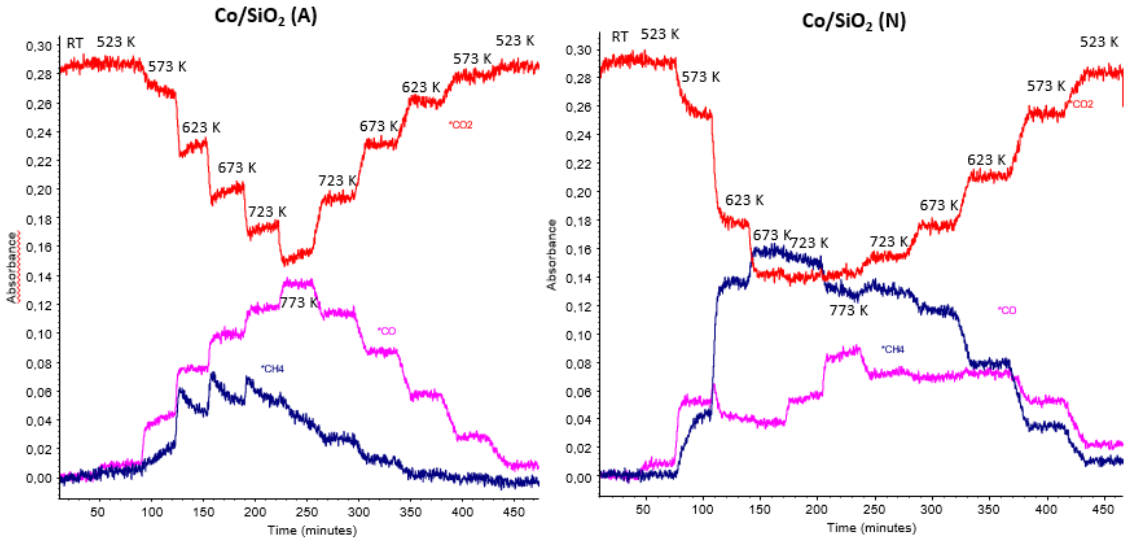

Figure 5.6. On-line FT-IR transmission/absorption analyses of the product gases upon catalytic hydrogenation experiments.

The data are shown in terms of absorbance of CO_2, CO and methane as a function of time (and thus of temperature steps). We do not observe any other products except water, so that the results are interpreted considering the occurrence of two reactions:

reverse water gas shift (rWGS): $CO_2 + H_2 \leftrightarrows CO + H_2O$ (1)

CO_2 methanation $CO_2 + 4\ H_2 \leftrightarrows CH_4 + 2\ H_2O$ (2)

In principle, reaction (2) can be parallel to reaction (1) or can be the result of the sequence of reaction (1) with the successive reaction (3), the methanation of CO

CO methanation $CO + 3\ H_2 \leftrightarrows CH_4 + H_2O$ (3)

It has to be remarked that no catalysts pre-reduction has been performed prior to catalytic experiments. Thus, the catalysts at the beginning of the experiment contain oxidized cobalt (Co_3O_4 and Co^{2+} in silica for sample Co/SiO_2 (A)). Also, we must remark that the intrinsic absorption (extinction coefficient) of the absorption bands we choose for analysis of CO_2, CO and CH_4 are (obviously) different: thus the curves do not directly represent the concentration of the species. The online analysis of the product mixture allows to provide evidence of possible activation / deactivation phenomena occurring during the pseudo-stationary steps.

The calculated CO_2 conversion and CO and CH_4 yields are reported in Table 5.2.

Table 5.2: equilibrium and experimental data for CO_2 hydrogenation

	Experimental data						Thermodynamic Equilibrium			
	Co/SiO_2(A) catalyst			Co/SiO_2(N) catalyst			Methanation + rWGS			rWGS only
T [K]	X CO_2	Y CH_4	Y CO	X CO_2	Y CH_4	Y CO	X CO_2	Y CH_4	Y CO	X CO_2 = Y CO
298	0%	1%	0%	0%	1%	0%	100%	100%	0	--
523	2%	2%	0%	0,0%	0,4%	0,1%	99,99%	99,99%	0,00%	21,50%
573	5%→8%	3%→5%	2%→3%	17%→20%	3%→11%	8,%	99,80%	99,80%	0,00%	29,83%
623	33%→29%	16%→12%	17%	57%	52%	5%	97,39%	97,31%	0,08%	38,37%
673	45%	18%→16%	27%→29%	70%	67%	3%	89,89%	89,17%	0,72%	46,57%
723	58%→51%	22%→14%	37%	71%	63%	8%	79,84%	76,32%	3,52%	54,06%
773	61%→57%	12%→10%	49%→47%	66%	48%	18%	71,27%	59,58%	11,69%	60,66%
723	42%→41%	8%→6%	34%→36%	61%	47%	14%	79,84%	76,32%	3,52%	54,06%
673	25%→26%	4%→3%	22%→23%	50%	38%	13%	89,89%	89,17%	0,72%	46,57%
623	12%	1%	10%	31%	16%	15%	97,39%	97,31%	0,08%	38,37%
573	3%	1%	2%	10%	1%	8%	99,80%	99,80%	0,00%	29,83%
523	0%	0%	0%	2%	1%	1%	99,99%	99,99%	0,00%	21,50%
298	0%	1%	0%	1%	1%	0%	100%	100%	0	--

Here they are compared with the expected conversion and yields calculated supposing that thermodynamic equilibrium is established for hydrogenation to CO and CH_4 or for hydrogenation to CO only (reverse water gas shift, rWGS).

In the case of catalyst Co/SiO_2 (A), the CO_2 conversion at 523 K is very low while at 573 K it is evident that a catalyst activation is occurring (the absorbance of CO_2 is decreasing in the step, thus conversion is increasing in the step). Accordingly, both CO and CH_4 yields are increasing, in the step. It is supposed that, in these conditions, reduction of at least part of cobalt oxide to cobalt metal is occurring. As expected, by increasing temperature the conversion of CO_2 increases (for kinetic reasons) but it remains well lower than that allowed by thermodynamics, showing that the reaction is under kinetic control. At these temperatures, the selectivity to CO is higher than selectivity to methane, in contrast to thermodynamics that would forecast almost complete hydrogenation to methane with production of traces only of CO. On the other hand, already at 623 K, and also at 673 K and 723 K catalyst deactivation is occurring upon the steps (CO_2 conversion is decreasing in the steps). However, while methane yield is also decreasing in the steps, CO yields are nearly stable or even slightly increasing in the steps. This indicates that two different active sites and/or pathways are active for rWGS and methanation in these conditions over this catalyst. At 773 K, CO_2 conversion is still lower than that allowed by rWGS but is far lower than that allowed by methanation. CO yield approaches 50%, still lower than that allowed by thermodynamics of the rWGS, with coproduction of 10% CH_4. It is evident that catalyst activity is quite good for rWGS and very low for methanation.

During the decreasing temperature step further deactivation of the methanation reaction is evident while the production of CO is nearly stable in the steps but slightly less than in the increasing temperature experiment. Thus, deactivation occurs for both methanation and rWGS, but is by far more important for methanation.

The behavior of catalyst Co/SiO_2 (N) is markedly different. While at 523 K a small amount of both products is already observed, at 573 and 623 K the catalyst shows a pronounced activation behavior, with increase of the production of methane, that results, at 623 K, in a slight decrease of the production of CO. In any case, the yield of CO is far lower than that of CH_4, but definitely higher than that forecast by thermodynamics if methanation was allowed. The conversion of CO_2 is still slightly lower than that allowed by thermodynamics of methanation at 723K and 773K, with a coproduction of CO markedly superior to that allowed by thermodynamics if methanation is allowed. The conversion of CO_2 is, in the temperature descending steps, lower than in the temperature ascending steps, with a decrease of methane yield more pronounced than that of CO.

Looking at the overall CO_2 conversion, catalyst Co/SiO_2 (N) is more active than catalyst Co/SiO_2 (A), and is also slightly more resistant to deactivation. Catalyst Co/SiO_2 (N) is definitely more active than catalyst Co/SiO_2 (A) and also more stable in methanation. Instead, catalyst Co/SiO_2 (A) is more active than catalyst Co/SiO_2 (N) in producing CO as a result of rWGS reaction. However, weak deactivation is also found for the production of CO.

5.2.3. Characterization of spent catalysts after methanation experiments

In Fig. 5.7 the XRD patterns of the catalysts after the methanation experiments are reported.

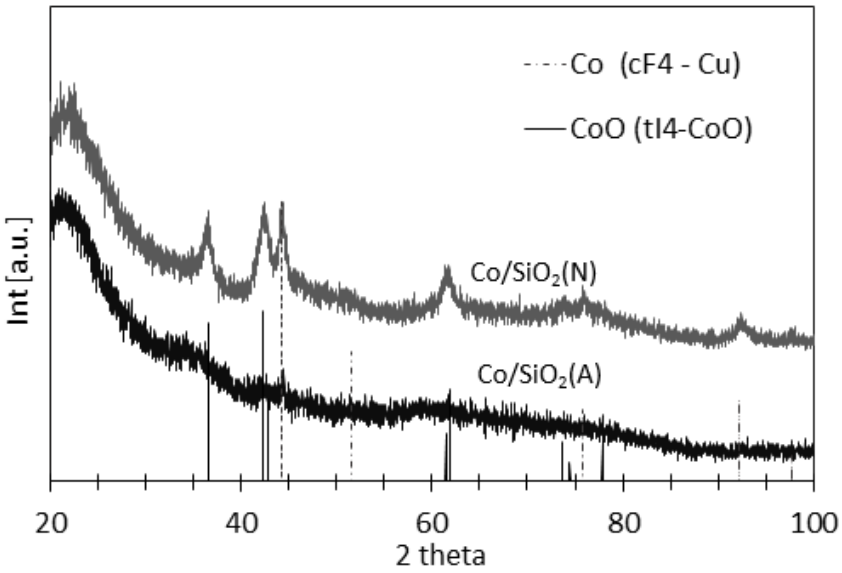

Figure 5.7. XRD patterns of the spent catalysts after methanation experiments.

In the case of catalyst Co/SiO_2 (N), the presence of both metallic cobalt in its cubic polymorph (i.e. the high temperature phase of this metal [25]) and cobalt monoxide CoO is observed. The detection of cubic cobalt instead of the hexagonal polymorph stable at room temperature is not unusual in CO hydrogenation catalysts [26]. On the other hand, it has been reported that it can be stabilized by carbon coating [27]. On the other hand, for nanoparticles the formation of one of the two phases may depend on preparation details [28].The presence of CoO indicates that the spent catalyst is only partly reduced.

A different result is observed in the case of catalyst Co/SiO_2 (A), which appears to be predominantly amorphous.

The FE-SEM images of the two catalysts are reported in Fig. 5.8.

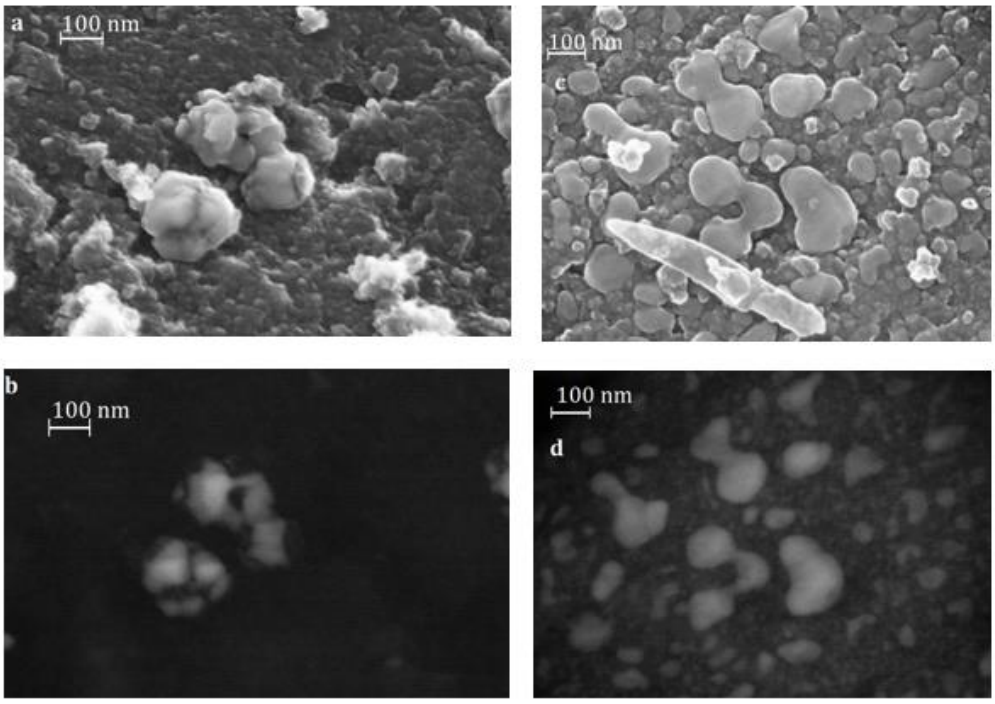

Figure 5.8. FE-SEM micrographs of the spent catalysts after methanation experiments. (a) and (b): sample A (in lens and BSE respectively); (c) and (d): sample N (in lens and BSE respectively);

The comparison of the particle shapes in the "secondary electrons" images and those obtained using backscattered electrons, indicate that cobalt-containing aggregates or polycrystalline particles are encapsulated in carbon residue covering layers. Additionally, in particular in the case of sample Co/SiO_2 (N) (Fig. 5.8 c and d)cobalt-based particles appear to be grown in size, with respect to the Co_3O_4 particles observed on the fresh catalyst, up to near 100 nm diameter, while cobalt seem also to having been dispersed over the silica particles (which appear moderately bright in the BSE images). Thus, deactivation might arise from two main reasons: coking (formation of encapsulating carbon) and amorphization of cobalt particles possibly causing dispersion of cobalt into the silica matrix, which seems to having been particularly occurred in the case of sample (A).

Encapsulation of cobalt particles by carbon can be the main reason for the rapid deactivation of the methanation reaction. This agrees with the main mechanism of deactivation of cobalt-based Fischer Trøpsch catalysts [29]. The lower activity and lower stability towards methanation of sample Co/SiO_2 (A) with respect to sample Co/SiO_2 (N) can be tentatively attributed to the larger cobalt particle size in the former coming from the larger size of Co_3O_4 particles, that may result in lower hydrogenation activity [30]. As already said, the activity in producing CO seems to follow a parallel and independent path in both catalysts. Isolated bivalent cobalt species in or on silica, which are more abundant in catalyst Co/SiO_2 (A) than in catalyst Co/SiO_2 (N), as well as CoO particles may have

activity in the rWGS reaction producing CO and may justify the better activity in rWGS of catalyst Co/SiO_2 (A).

The IR spectra of spent samples, obtained after sieving to separate silica glass particles, show the typical features of silica already observed for fresh silica support, i.e. the typical position of pure silica 1093, 797 and 465 cm^{-1}, suggesting a reduced interaction in between Cobalt and silica after reduction and reduction. Together with those bands, a new band is observed at 668 cm^{-1} for both catalysts after methanation experiments. This band, stronger in the case of sample Co/SiO_2 (A), corresponds to the one previously observed in the IR spectrum of the cobalt phyllosilicate antigorite ($Co_3Si_2O_5(OH)_4$) [31] where a Co atom is in an octahedral site in an octahedra layer. Thus, this band is assigned to a Co-O-Co stretching mode of octahedra Cobalt oxide clusters.

The UV-vis features of the spent catalysts are reported in Figure 4 left. The spectra of Co/SiO_2 (N) shows a continuous diffuse reflectance in all the range suggesting that a large part of Cobalt is in the metallic state. The spectrum of Co/SiO_2 (A) instead shows stronger transmittance and the triplet discussed above for the fresh sample of Co^{2+} dispersed in silica. Concluding, the all data agree indicating that in the Co(N) sample metallic cobalt and CoO (whose IR spectrum is superimposed to silica) are present together with some octahedral cobalt cluster. In the case of sample A instead amorphous octahedral Co clusters and Co silicate species are present after methanation reaction.

5.2.4 Catalytic activity in Ethanol Steam reforming (ESR)

Preliminary ESR experiments were realized by increasing decreasing temperature steps experiments with temperatures up to 773 K, which is the previous calcination temperature for Co/SiO_2 catalysts. In these conditions, ethanol dehydration to acetaldehyde is the main reaction, steam reforming occurring only to a small extent. In these experiments a substantial stability of the catalyst up to 773 K was found, with the activity in the descending temperature steps well corresponding to that obtained in the ascending temperature step.

To push ESR reaction temperatures up to 973 K are needed. However, we did not precalcine the catalysts at so high a temperature to not cause a so strong reaction of cobalt with the silica support before ESR experiments.

Catalyst Co/SiO_2 (A), whose activity data are reported in Table 5.3, is active as an ethanol dehydrogenation catalyst at 673 K while it gives rise to complete steam reforming at 873 K and 973 K with an hydrogen yield of 72-74 %, limited by the production of methane with ~10% selectivity. Limited deactivation is observed in the decreasing temperature steps.

Table 5.3: ESR on Co/SiO_2 (A) catalysts

T(K)	X C_2H_6O	X H_2O	Y H_2	S CH_4	S CO	S CO_2	S CH_2CH_2	S CH_3CHO	S C_3H_6	S DEE	S $C_4H_8O_2$	S C_6H_6
523	0,01	-	-	-	-	-	-	-	-	-	-	-
573	0,01	-	-	-	-	-	-	-	-	-	-	-
673	0,24	0,00	0,04	0,00	0,00	0,00	0,09	0,86	0,01	0,02	0,02	0,01
773	0,85	0,03	0,22	0,03	0,07	0,10	0,09	0,68	0,01	0,00	0,01	0,01
873	1,00	0,31	0,74	0,10	0,37	0,52	0,00	0,00	0,00	0,00	0,00	0,00
973	1,00	0,30	0,72	0,11	0,38	0,50	0,00	0,00	0,00	0,00	0,00	0,00
873	1,00	0,30	0,72	0,11	0,37	0,51	0,00	0,00	0,00	0,00	0,00	0,00
773	0,75	0,10	0,32	0,05	0,14	0,25	0,02	0,53	0,00	0,00	0,01	0,00
673	0,20	0,01	0,05	0,03	0,06	0,06	0,01	0,83	0,00	0,00	0,01	0,00
573	0,05	0,00	0,01	0,00	0,01	0,04	0,00	0,85	0,10	0,00	0,00	0,00
523	0,01	-	-	-	-	-	-	-	-	-	-	-

Catalyst Co/SiO_2 (N), whose activity data are reported in Table 5.4, is definitely more active than catalyst A in ESR, which already occurs to a large extent at 773 K and is complete at 873 K with 75 % hydrogen yield and also ~10% methane selectivity.

Table 5.4: ESR on Co/SiO_2 (N) catalysts

T(K)	X C_2H_6O	X H_2O	Y H_2	S CH_4	S CO	S CO_2	S CH_2CH_2	S CH_3CH_3	S CH_3CHO	S C_3H_6	S $C_4H_8O_2$
523	0,01	-	-	-	-	-	-	-	-	-	-
573	0,02	-	-	-	-	-	-	-	-	-	-
673	0,17	0,00	0,03	0,00	0,00	0,01	0,03	0,00	0,90	0,03	0,03
773	1,00	0,23	0,61	0,11	0,33	0,40	0,01	0,00	0,15	0,00	0,00
873	1,00	0,32	0,75	0,11	0,31	0,58	0,00	0,00	0,00	0,00	0,00
973	1,00	0,24	0,65	0,11	0,51	0,34	0,02	0,01	0,01	0,00	0,00
973	1,00	0,18	0,56	0,10	0,50	0,25	0,07	0,01	0,07	0,00	0,00
873	0,60	0,03	0,18	0,01	0,18	0,09	0,09	0,01	0,62	0,00	0,01
773	0,17	0,00	0,03	0,01	0,03	0,02	0,01	0,00	0,92	0,01	0,00
673	0,04	0,00	0,01	0,00	0,01	0,02	0,00	0,00	0,91	0,05	0,00
573	0,01	-	-	-	-	-	-	-	-	-	-
523	0,01	-	-	-	-	-	-	-	-	-	-

However, it results to be less stable: In the descending temperature experiments, deactivation is already advanced at 873 K with decrease of conversion and ESR activity, and increased dehydrogenation selectivity to acetaldehyde.

5.2.5 Characterization of spent catalyst after ESR

In Figure 5.9, the diffractograms of the catalysts after ethanol steam reforming tests are reported.

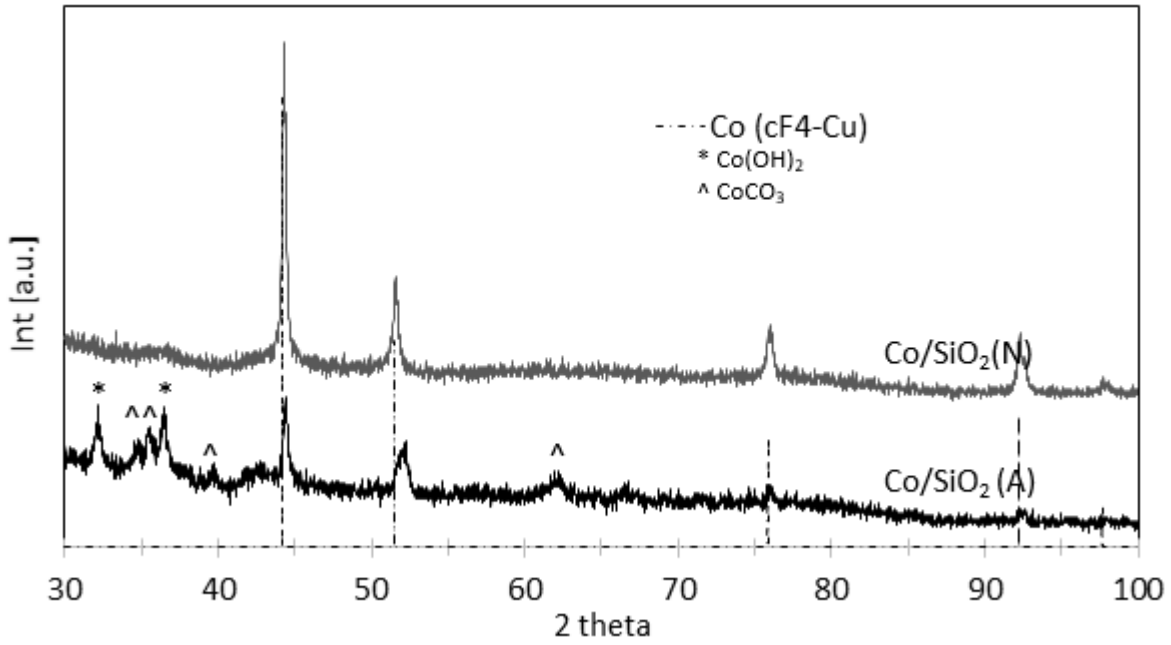

Figure 5.9. XRD patterns of the spent catalysts after ethanol steam reforming experiments.

In both cases cubic metallic cobalt (Co, cF4-Cu) is detected. The measured particle sizes, evaluated with the Scherrer formula, are around 31 nm for sample Co/SiO_2 (N) and 28 nm for sample Co/SiO_2 (A). Thus, interestingly, even if the starting Co_3O_4 particles were smaller for sample Co/SiO_2 (N), after reaction they underwent a greater sintering becoming larger than sample A after ESR experiments. In the case of catalyst Co/SiO_2 (A), however, also oxidized cobalt species are found in the form of $Co(OH)_2$ and $CoCO_3$.

FE-SEM images (Fig. 5.10) show, in the case of sample Co/SiO_2 (A) the presence of large (> 100 nm diameter) carbon nanotubes containing Co particles (Fig.5.10 a,c) together with smaller nanotubes (~ 20 nm diameter) which are mostly empty (Fig.5.10 b,d). It can be mentioned that, in agreement also with previous studies, the formation of carbon nanotubes does not result in strong catalyst deactivation.

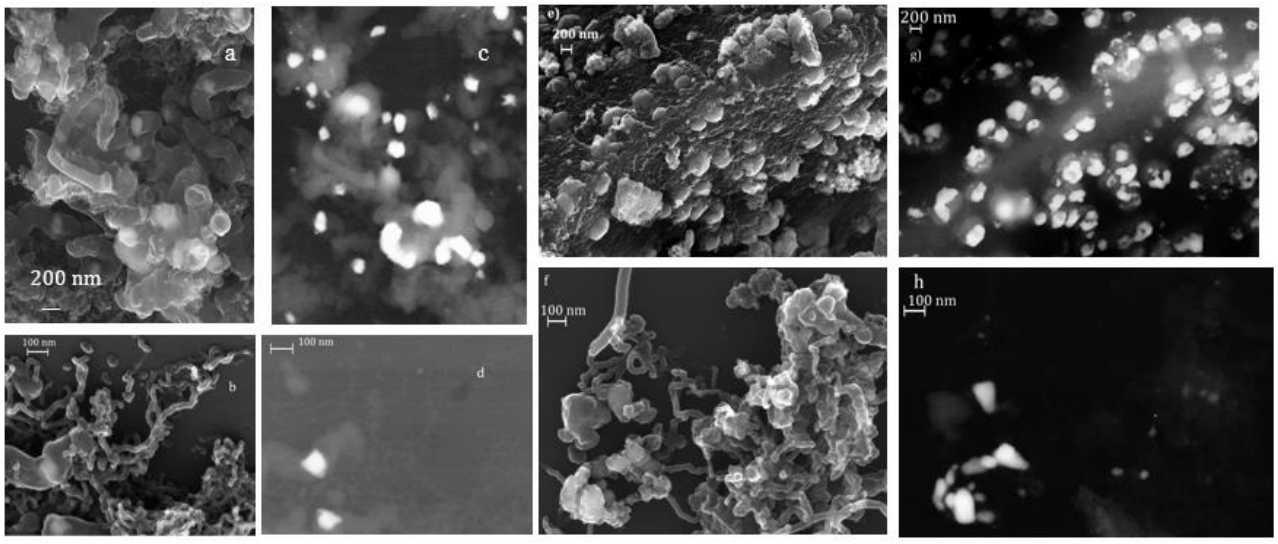

Figure 5.10. FE-SEM micrographs of the spent catalysts after ethanol steam reforming experiments. (a) - (d): two different portions of sample A (in lens (a) and (c), and BSE (b) and (d) respectively). (e) - (h): two different portions of sample N (in lens (e) and (g), and BSE (f) and (h) respectively).

Instead, by a close look to the sample Co/SiO_2 (N) micrographs, only some portions of the sample show the formation of carbon nanotubes, together with Co-containing particles characterized by 100-50 nm diameter (Fig.5.10 f, h). Most of the surface does not contain carbon species, and clearly shows small cobalt-containing particles (~ 200 nm diameter) emerging from the surface of silica particles and surrounded by cobalt-containing silica (Fig.5.10 e, g).

These data suggest that smaller cobalt particles are more active in ESR, in agreement with the literature [32] but also in forming carbon nanotubes, that, however, do not hinder the reaction at list in the timescale of our laboratory experiments. These particles are more abundant on spent Co/SiO_2 (A). Larger cobalt-containing particles partly embedded on the silica matrix, which are predominant in sample Co/SiO_2 (N), likely represent deactivated sites for both ESR and formation of carbon nanotubes. It is not excluded that these particles also contain silicate species. The deactivation of Co/SiO_2 (N) sample should be associated to a stronger reaction of cobalt particles with silica producing such strongly interacting particles. A similar mechanism was identified to be another cause of deactivation of Co/SiO_2 catalysts for the Fischer-Tropsch reaction, and water was found to favor this deactivation mechanism [27].

It seems interesting also to remark that both catalysts produce mainly acetaldehyde at 673 K. This likely indicates that at this temperature water is still not activated. For this reason the catalysts behave as dehydrogenation catalysts. However, catalyst N produces predominantly acetaldehyde

also at 873 K in the temperature descending experiments, i.e. when it is deactivated for ESR. This suggests that deactivation of sample (N) occurs with poisoning of the water activation sites.

5.3 Conclusions

The main conclusion of this work are the following:

1. Co/SiO_2 catalysts are active in CO_2 methanation at 573-773 K and atmospheric pressure, but deactivate easily and fast.
2. The catalysts, which are charged in the reactor in oxide form as Co_3O_4/SiO_2, activate spontaneously by reduction in the CO_2/H_2 feed at 573 K and above. The active phase for methanation is constituted by cubic cobalt particles. These particles, however, rapidly become deactivated by encapsulating carbon according to their high activity in favoring the formation of C-C bonds.
3. These catalysts also have remarkable activity in the reverse Water Gas Shift reaction producing CO upon CO_2 hydrogenation. The active sites for this reaction appear to be independent from those for methanation.
4. Depending on the precursor, Co/SiO_2 catalysts can contain Co^{2+} ions interacting with the support in the form of isolated cobalt (II) silicate species. After reaction they may also contain CoO particles. These unreduced cobalt species are likely responsible for rWGS activity.
5. Co/SiO_2 catalysts are also very active in ethanol steam reforming at 873-973 K with coproduction of only limited amounts of methane (~ 10 % C-selectivity) at full ethanol conversion.
6. The active phase for ESR is supposed to be represented by cubic cobalt, whose activity is greater for smaller particles. However, these particles are also active in producing carbon nanotubes. On the other hand, the formation of carbon nanotubes does not hinder catalytic activity at the timescale of a few hour laboratory experiment.
7. Depending on the precursor, the catalyst may deactivate by forming larger cobalt-containing nanoparticles partly embedded on the silica/cobalt silicate surface. These particles, possibly containing also silicate species, are also not active in producing carbon nanotubes, i.e. they are unable to both activate water and favor C-C bond formation.

8. At lower temperature (773 K and less) or when deactivated, the catalysts become active in producing acetaldehyde in spite of the presence of steam. This confirms that deactivation of the catalysts inhibits the sites for activation of water for steam reforming.
9. The differences observed among catalysts produced from cobalt acetate and cobalt nitrate can be associated to the different pH of the impregnating solution. The higher pH of cobalt acetate solution can result in small dissolution of silica and favor the formation of cobalt silicate surface species. These species can reduce the reactivity of the surface of silica thus reducing the density of the “anchoring” sites for Co metal particles, finally producing larger cobalt particles.
10. These cobalt silicate surface species can stabilize the surface also against further reaction observed at high temperature (in ESR conditions), more evident for the ex-nitrate sample N, that finally results in catalyst deactivation.

5.4 References

[1] G. Garbarino, C. Wang, I. Valsamakis, S. Chitsazan, P. Riani, E. Finocchio, M. Flytzani-Stephanopoulos, G. Busca, Appl. Catal. B Envir., 174 (2015) 21-34.

[2] G. Garbarino, P. Riani, L. Magistri, G. Busca, Int. J. Hydrogen Energy, 39 (2014) 11557-11565

[3] G. Garbarino, P. Riani, M. Lucchini, F. Canepa, S. Kawale, G. Busca, Int. J. Hydrogen Energy, 38 (2013) 82-91

[4] P. Riani, G. Garbarino, A. Infantes-Molina, E. Rodríguez-Castellón, F. Canepa, G. Busca, Appl .Catal .A Gen. 518(2016) 67-77.

[5] P. Riani, G. Garbarino, F. Canepa, G. Busca, J. Chem. Technol. Biotechnol. (2018) in press published on internet

[6] K. Aasberg-Petersen, I. Dybkjær, C.V. Ovesen, N.C. Schjødt, J. Sehested, S.G. Thomsen, J. Nat. Gas Sci. Eng. 3 (2011) 423-459

[7] E. Moretti, L. Storaro, A. Talon, S. Chitsazan, G. Garbarino, G. Busca, E. Finocchio, Fuel 153 (2015) 166–175

[8] G. Busca, U. Costantino, T. Montanari, G. Ramis, C. Resini, M. Sisani, Int. J. Hydrogen Energy, 35 (2010) 5356 -5366

[9] R.U. Ribeiro, J.W.C. Liberatori, H. Winnishofer, J.M.C. Bueno, D. Zanchet, Appl. Catal. B Environ. 91 (2009) 670–678.

[10] O. Levenspiel, Chemical Reaction Engineering, 3rd ed., Wiley, New York, 1999, p.87.

[11] G. Busca in S. D. Jackson, J.S.J. Hargreaves eds., Metal Oxide Catalysis, Wiley, 2009, pp.119-120.

[12] G. Busca, R. Guidetti and V. Lorenzelli, J. Chem. Soc., Trans. ,1990, 86 , 989-994.

[13] M. Lenglet, B. Lefez, Solid State Commun. 98 (1996) 689-694.

[14] Y. Li, W. Qiu, F. Qin, H. Fang, V.G. Hadjiev, D. Litvinov, J. Bao, J. Phys. Chem. C, 120 (2016) 4511-4516.

[15] M. Andrés-Vergés, C.J.Serna, J. Mat. Sci. Letters 7(1988) 970-972

[16] J. E. Iglesias, M. Ocaña, C.J. Serna, Appl. Spectrosc., 44 (1990) 418-426

[17] J. Gonzalez-Prior, J.I. Gutierrez-Ortiz, R. Lopez-Fonseca, G. Busca, E. Finocchio, B. de Rivas, Catal. Sci. Technol. , 6 (2016) 5618-5630.

[18] M. El Hadri, H. Ahamdane, M.A. El Idrissi Raghni, Bull. Mat. Sci. 40 (2017) 375-382.

[19] S. Thota, A. Kumar, J. Kumar, Mater. Sci. Eng. B 164 (2009) 30–37

[20] N.H.M Zaki, M. Mustaffa, M.F.M. Taib, O.H.Hassan, M.Z.A.Yahya, A.M.M.Ali, Int. J. Eng. Tech., 7 (2018) 121-125

[21] M.N. Taran, G.R. Rossman, American Mineralogist 86 (2001) 889-895.

[22] A. Ceglia, W. Meulebroeck, K. Baert, H. Wouters, K. Nys, H. Thienpont, H. Terryn Surf. Interface Anal. 44 (2012) 219–226.

[23] L., Drozdova, R. Prins, J. Dedechek, Z. Sobalik, B. Wichterlova, J. Phys. Chem. B 106 (2002) 2240-2248.

[24] T. Montanari, M. Bevilacqua, C. Resini, G. Busca, J. Phys. Chem. B 108 (2004) 2120-2127.

[25] R. Lizárraga, F. Pan, L. Bergqvist, E. Holmström, Z. Gercsi, L. Vitos, Scientific Reports 7 (2017) 3778 |

[26] G. Busca, F. Trifiro, and A. Vaccari, Langmuir, 1990, 6 (9), pp 1440–1447

[27] S.V. Pol, V.G. Pol, G. Seisenbaeva, V.G. Kessler, A. Gedanken, Chem. Mater., 16 (2004) 1793–1798.

[28] N. Liakakos, B. Cormary, X. Li, P. Lecante, M. Respaud, L. Maron, A. Falqui, A. Genovese, L. Vendier, S. Koïnis, B. Chaudret, K. Soulantica, J. Am. Chem. Soc., 2012, 134 (43), pp 17922–17931

[29] M.D. Argyle, C.H. Bartholomew, Catalysts 5 (2015) 145-269.

[30] T.O. Eschemann, K.P. de Jong, ACS Catal., 5 (2015) 3181–3188.

[31] J.R. Sohn, J.I. Leon, Korean J. Chem. Eng. 6 (1989) 56-57.

[32] A.L.M. da Silva, J.P.den Breejen, L.V. Mattos, J.H. Bitter, K.P.de Jong, F.B. Noronha, J. Catal. 318 (2014) 67-74

Chapter 6

Preparation and characterization of alumina supported nickel catalysts and their catalytic activity in CO_2 methanation and ESR: effect of lanthanum doping

In order to improve the CO_2 methanation process efficiency, a possible way is to improve the cheap Ni/γ-Al_2O_3 catalysts, by tailoring optimal Ni particle size [1] and loading [2], thus increasing low temperature activity and CH_4 selectivity, as well as by stabilizing it structurally. Our research group previously found that Lanthanum doping improves the properties of Ni/γ-Al_2O_3 catalysts for steam reforming reactions [3]. Lanthanum is also reported to be fundamental in most of perovskite cathodes in Solid Oxide Fuel Cells [4] (i.e. LSM, LSCF etc.). On the other hand, lanthanum is reported to be a relevant additive to alumina in catalyst formulations: it improves alumina properties by increasing its mechanical strength [5] and stabilizing spinel-type alumina with respect to sintering and loss of surface area [6]. Additionally, it has been reported that lanthana can be used as precursor of sulfur-tolerant catalysts, being converted in situ to lanthanum oxysulfide (La_2O_2S) [7].

In previous works we reported on the methanation activity of different Ni/Al_2O_3 catalysts [2,8], as well as on the preparation and characterization of La_2O_3-Al_2O_3 catalytic materials [9, 10]. In the present chapter will be reported on ways to improve the catalytic properties of a home-made 13.6 wt.% Ni/γ-Al_2O_3 catalyst by modifying the alumina support with Lanthanum.

6.1. Materials preparation

The catalysts were prepared using Puralox 200 Sba (γ-Al_2O_3, 200 m^2/g) from Sasol previously calcined at 1023 K for 5 h as bare support. The catalytic materials, summarized in Table 6.1, were prepared through incipient wetness impregnation using $La(NO_3)_3*xH_2O$ (x~4) and $Ni(NO_3)_2*6H_2O$ (from Alfa Aesar and Sigma Aldrich, respectively) aqueous solutions.

Table 6.1: Composition, surface area and hydrogen consumption data

	NiO wt%	La_2O_3 wt%	BET Surface area	H_2 consumption
	w_{NiO}/w_{cat} [%]	w_{La2O3}/w_{cat} [%]	[m^2/g]	[μmol/g]
NiØLA	16.7%	-	151	3159
Ni4LA	16.7%	4%	150	3142
Ni14A	16.7%	14%	131	3051
Ni37LA	16.7%	37%	100	2974

The theoretical amounts of La and Ni to obtain the designed % oxide on alumina (measured as $100*g_{MO}/100g_{cat}$ where MO is La_2O_3 or NiO and cat is the total catalyst weight). Different La_2O_3 contents in catalyst formulation (xLA, with x= 4, 14 and 37 wt.%) were achieved by dissolving the precursor salts in a volume of deionised water, in the way that the total liquid volume was equal to the pore volume of the material. A step of drying at 353 K in vacuum was undertaken for 15 h and calcination in air at 1023 K for 5 h with a temperature ramping of 2 K/min was performed. The NixLA catalyst was prepared using xLA as the support, thus the first impregnation was with La and the second with Ni precursors with an intermediate calcination of the support with the same procedure applied for the whole catalysts and reported above.

For the catalytic experiments and characterization, the catalysts were reduced in situ with a 20 mol%H_2-80 mol%N_2 mixture and a total flow rate of 70 NmL/min. The heating rate was fixed at 25 K/min to 1023 K, then held for 30 min at that temperature. The catalysts were cooled to r.t. (room temperature) in the same atmosphere to avoid oxidation and kept in a pure nitrogen stream.

All the synthetized catalysts have been fully characterized by means of: surface area measurements, X-Ray diffraction, Temperature Programmed Reduction with H_2 (H_2-TPR), FT-IR, X-ray photoelectron spectroscopy (XPS), microscopic analyses FE-SEM and EDX microanalysis.

6.2. Results

6.2.1 Characterization of the fresh catalyst

6.2.1.1 Surface area measurements.

The surface area of the pure alumina support, calcined at 1023 K for 5 h, is 170 m^2/g. The sequence of impregnation of lanthanum and nickel reduces the surface area, to nearly 150 m^2/g for NiØLA and Ni4LA, down to 130 m^2/g and 100 m^2/g for Ni14LA and Ni37LA, respectively.

6.2.1.2 XRD Characterization

In Figure 6.1, the XRD patterns of the as prepared samples under study are reported together with the diffractograms of the corresponding supports.

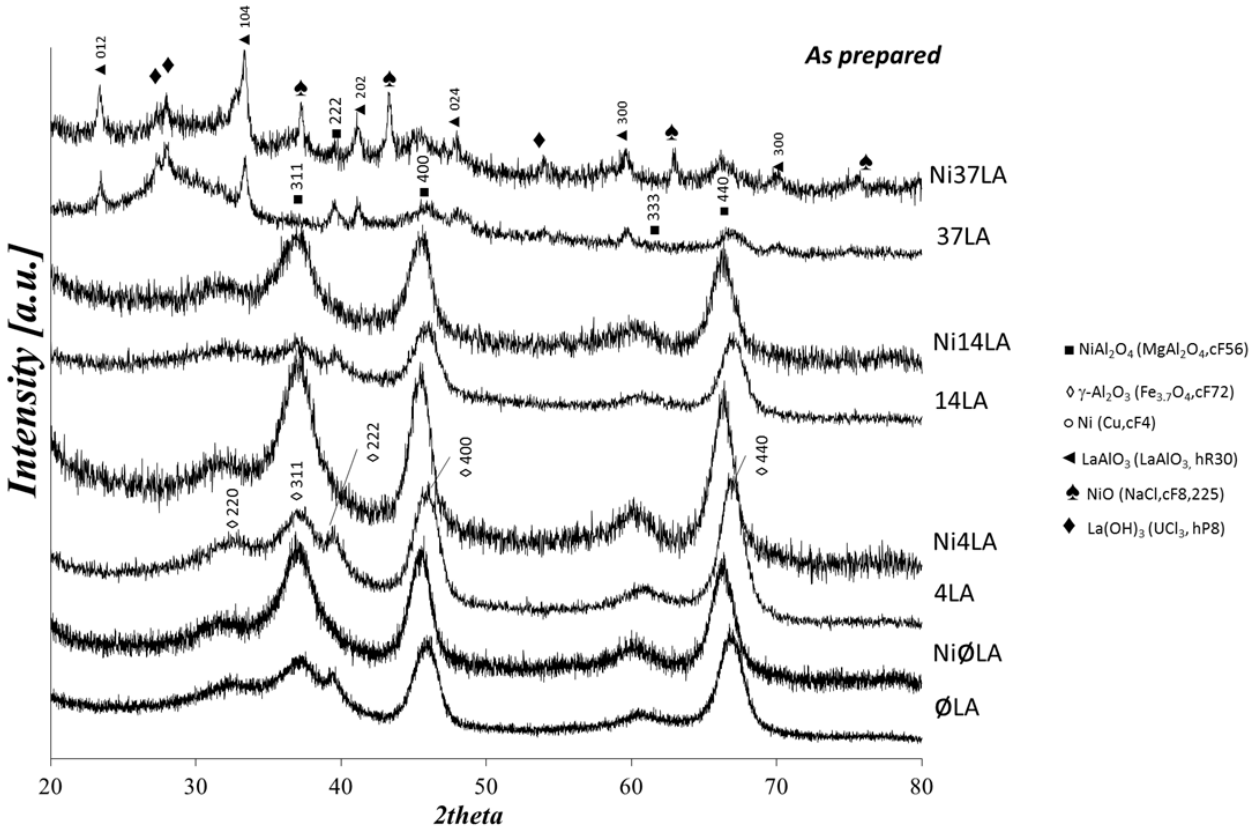

Figure 6.1. X-Ray diffraction patterns of as cast supports (xLA) and unreduced Ni-based catalysts (NixLA) together with the identification of crystalline phases [11].

The diffraction patterns of NiØLA, Ni4LA and Ni14LA show, with respect to γ-Al_2O_3 (ØLA), an intensification and a shift toward smaller 2θ of the 400 and 440 spinel peaks and, in particular, to

those assigned to the 311 peak, with almost complete disappearance of the 222 one. The resulting diffraction pattern is similar to that observed for $NiAl_2O_4$ inverted spinel [12] even if the composition is still cationically deficient ($Ni_{0.26}Al_2O_{3.26}$ in line with the determined EDX composition $Ni_{0.36}Al_2O_{3.36}$) with respect to the spinel composition, although less deficient than γ-Al_2O_3. This is in line with previous studies that showed that XRD patterns of both cationically deficient and stoichiometric $NiAl_2O_4$ are very similar [12,13]. As already reported, a strong interaction of surface Ni with alumina occurs with the formation of surface or subsurface Ni aluminate and this is evident by observing the shift toward low 2θ values of the 440 peak that corresponds to a slight expansion of the cubic cell volume [14]. The presence of lanthanum does not modify the diffractogram in these cases and a constant 2θ shift of the 440 peak is observed for the three samples. The picture for the samples NiØLA, Ni4LA and Ni14LA suggests that Ni spreads and strongly interacts with the alumina surface while lanthanum disperses over the surface without a significant perturbation of the bulk.

A different situation is observed for the Ni37LA catalyst. In this case, several different phases are found together with the spinel. In fact, the presence of $La(OH)_3$ and a rhombohedral perovskite $LaAlO_3$, phases are observed, as found in the corresponding La_2O_3-Al_2O_3 "support" [9]. The presence of NiO (bunsenite, JCPDS table 04-0835) is clearly observed only for the Ni37LA sample, while it is not present in other samples whose Ni loading is the same [15]. This might be due to the significant reduction of the surface area of the La-rich support and/or to its different composition, resulting in a lower interaction of Ni with the surface favouring the oxide formation.

In Figure 6.2, the diffraction patterns of the reduced catalysts are reported.

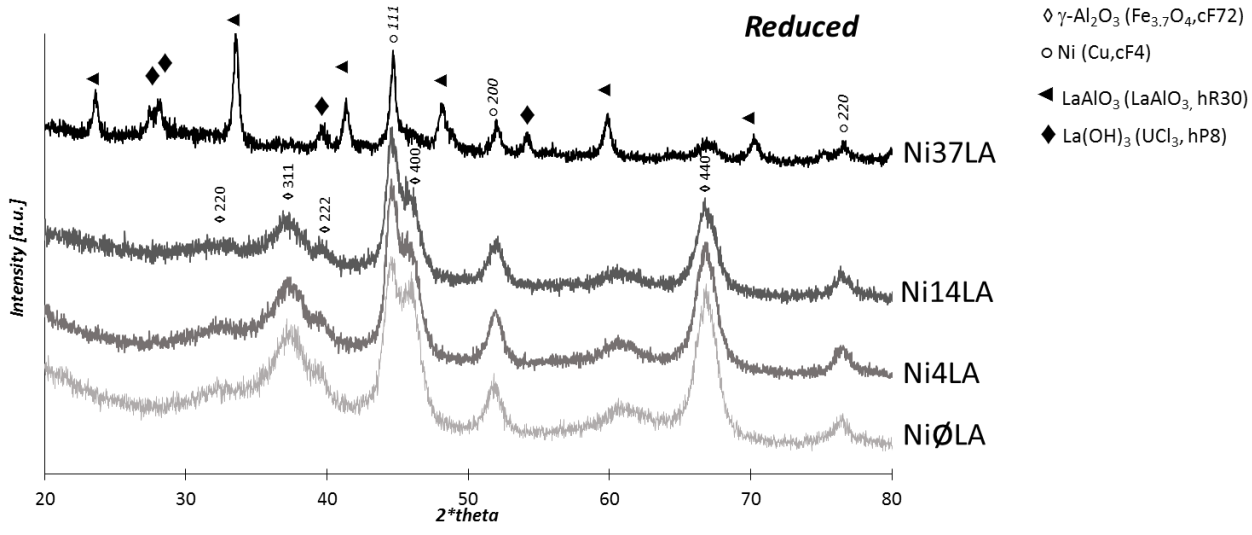

Figure 6.2. X-Ray diffraction patterns of reduced NixLA catalysts and identification of the crystalline phases

As expected, reduction of NiØLA, Ni4LA and Ni14LA produces cubic metallic Nickel with a reappearance of the characteristic 222 peak typical of γ-Al_2O_3, and a shift of γ-Al_2O_3 peaks to the characteristic listed structure peaks [16,11]. This indicates that, upon reduction, the surface or sub-surface aluminate phase produces less dispersed nickel as Ni nanoparticles.

For Ni37LA, the disappearance of the peak corresponding to NiO is observed with the appearance of cubic metallic nickel. For this sample, an increased crystallinity is observed after reduction with a clear appearance of the peaks assigned to $La(OH)_3$. For the metallic Ni phase, an evaluation of crystallite size through the Scherrer formula, using the (2,0,0) crystal plane family, determined particle diameters of 7 nm, 8 nm, 10 and 15 nm in the four samples, at increasing, from 0 to 37 wt. %, La_2O_3 loading, with a linear trend. To calculate crystallite dimensions, data have been previously treated with a smooth function, and then the line profile peaks have been fitted with a pseudo-Voigt function.

6.2.1.3 Skeletal IR and UV-vis spectroscopic characterization of unreduced catalysts.

In Figure 6.3, the infrared skeletal spectra of the materials are reported. The spectra of Ni-containing samples markedly differ from the spectra of the Ni-free “supports” because of the presence of a pronounced component at 723 cm^{-1}, as well as to a slight shift downwards of the main band from near 545 cm^{-1} to 508 cm^{-1}. This confirms the results obtained by XRD showing the features of spinel $NiAl_2O_4$ or of cationically deficient $Ni_xAl_2O_{3+x}$ spinels, which are very similar each other [12].

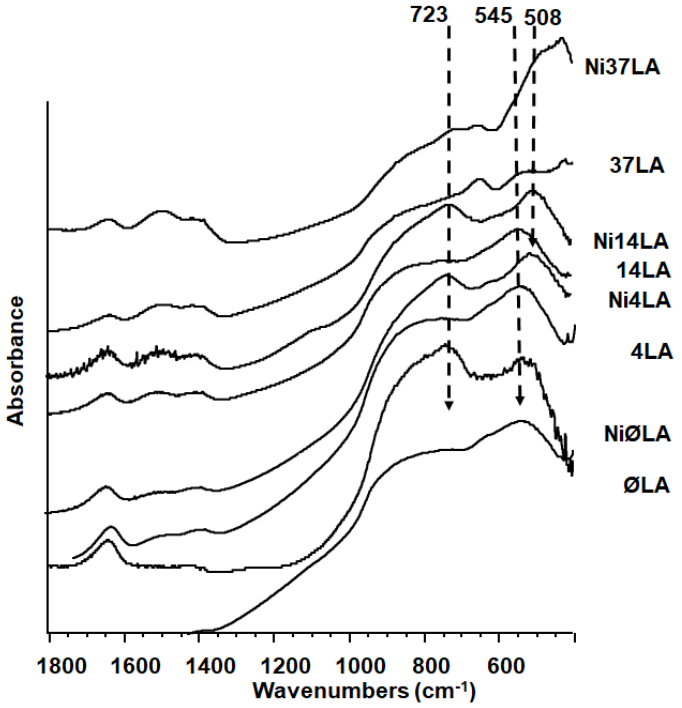

Figure 6.3. Skeletal IR spectra of as cast supports xLA and unreduced NixLA catalysts.

A different situation is found for Ni37LA where the feature at 429 cm^{-1} is associated to the presence of bulk NiO [17, 18, 19, 20] which masks the features of other phases such as $LaAlO_3$ [3, 21]. The presence of lanthanum species is confirmed by the fingerprint of carbonate features (1400 and 1491 cm^{-1}) which can be associated either with surface or bulk lanthanum carbonates [22, 23]. It is noted that the carbonate band intensities increase as the La- loading increases.

In Figure 6.4, the diffuse reflectance UV-visible spectra (DR-UV-vis-NIR) of the as prepared catalysts are reported. NiØLA, Ni4LA, Ni14LA spectra show absorption in the visible region, characterized by a split band at 601 and 633 nm, which is attributed to the $^3A_{2g} \rightarrow a^3T_{1g}$ d–d transition of Ni^{2+}, split for the presence of the weaker $^3A_{2g} \rightarrow a^1E_g$, whose position and shape are typical of Ni^{2+} dispersed on alumina [13, 24] in an environment similar to that of $NiAl_2O_4$ spinel.

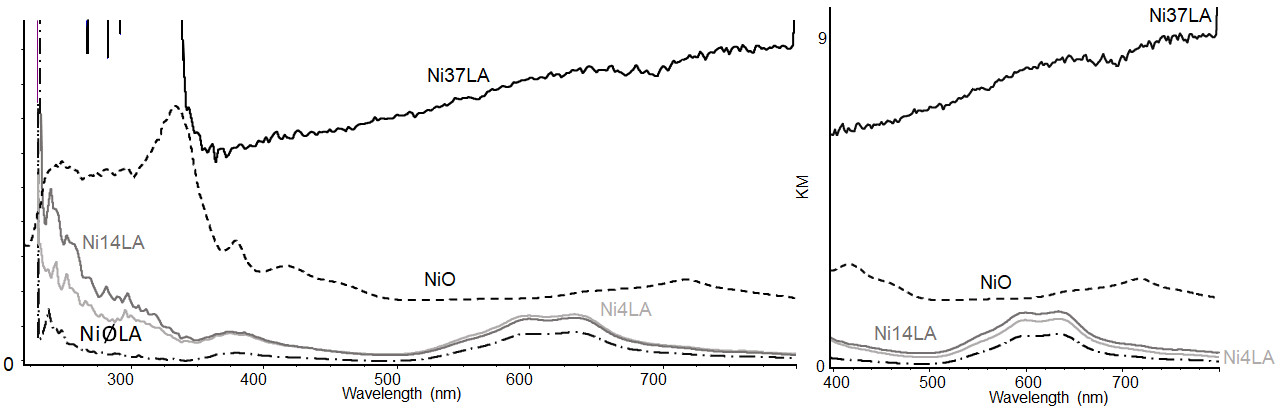

Figure 6.4. DR-UV-vis spectra of NixLA catalysts (full lines) and NiO reference sample (dotted line)

Moreover, the clear absence of the feature at 718 nm indicates that NiO species are not present in any of the three catalysts [13]. By looking at the NIR region, a broad band is observed near 1048 nm that is assigned to v_1 ($^3A_{2g} \rightarrow {}^3T_{2g}$) transition of Ni^{2+} in octahedral surroundings in a position similar to the one reported for low loading Ni catalysts, i.e. $NiAl_2O_4$ [25] and Ni highly dispersed on alumina [14,15].

Indeed, the spectra of NiØLA, Ni4LA and Ni14LA look qualitatively similar in the visible region, although the addition of lanthanum seems to slightly increase the background absorption. At lower wavenumbers, in the UV region, the addition of Lanthanum seems to cause the formation of a shoulder centered around 310 nm, absent in the case of the NiØLA sample, at the high wavenumber side of the absorbance increase due to the a O^{2-} (2p)→ Ni^{2+} (3d) charge transfer transition. This shoulder, located at lower energy than the corresponding transition of isolated Ni^{2+} on alumina, can be associated to Ni^{2+} species interacting with other Ni^{2+} or with La^{3+} species.

In agreement with the XRD results, a different situation is observed for Ni37LA. This sample is absorbing a great part of the radiation, inhibiting the possibility to observe characteristic absorption in the visible range. This might be due to the strong absorption of the visible light by $LaNiO_3$ perovskite [26]. Additionally, the sample shows a cut off near 350 nm due to the appearance of the strong O^{2-} (2p)→ Ni^{2+} (3d) charge transfer transition of bulk NiO, in agreement with XRD and H_2-TPR data.

These spectroscopic data confirm that, even in the presence of significant amounts of lanthanum, nickel strongly interacts with alumina. Only at the highest La loading, the situation changes, with the formation of lanthanum rich phases.

6.2.1.4 XPS analysis of unreduced catalysts.

In Fig. 5, the XP spectra are reported in the Al(2p), Ni(3p) and La(3d 5/2) regions. The Al(2p) spectra of NiØLA, Ni4LA and Ni14LA show a significant shift of the main peak from 74.2 eV, value reported for γ-Al_2O_3 [27, 28], down to 73.9 eV for Ni4LA and Ni14LA and further shifting to 73.5 for Ni37LA. The shift of the XP peak to lower binding energy is interpreted as due to a decreased ionicity of the Al-O bond [29] or to a higher density of the phase [30]. In any case the trend, i.e. the shift increasing

with increasing Ni loading, seem to further indicate a strong interaction of Ni with surface Al ions. In the same region, an additional component appears at 68.9 eV for NiØLA, shifting to 68.2 eV and 68.0 for Ni4LA and Ni14LA samples respectively, which is due to Ni 3p core level spectra of Ni^{2+} species [31, 32]. A split of the components is observed for Ni37LA where signals at 69 and 67 eV are present showing that an additional Ni-containing species is formed, which can be identified as $LaNiO_3$ phase [33] or $LiAl_{1-x}Ni_{1-x}O_3$ solid solution.

The XP spectrum of NixLA samples in the 830-845 eV region (Fig. 6.5) is due to lanthanum 3d5/2 transition. The peak positions we found for the three La-containing catalysts are close to 835.0 eV and 838.5 eV, at slightly higher energies than those reported for bulk $La(OH)_3$ [34], La_2O_3 [34, 35, 36], $LaAlO_3$ [34, 36], and for a number of La hexaaluminates [37, 38, 39] but in good agreement with our previous results [3].

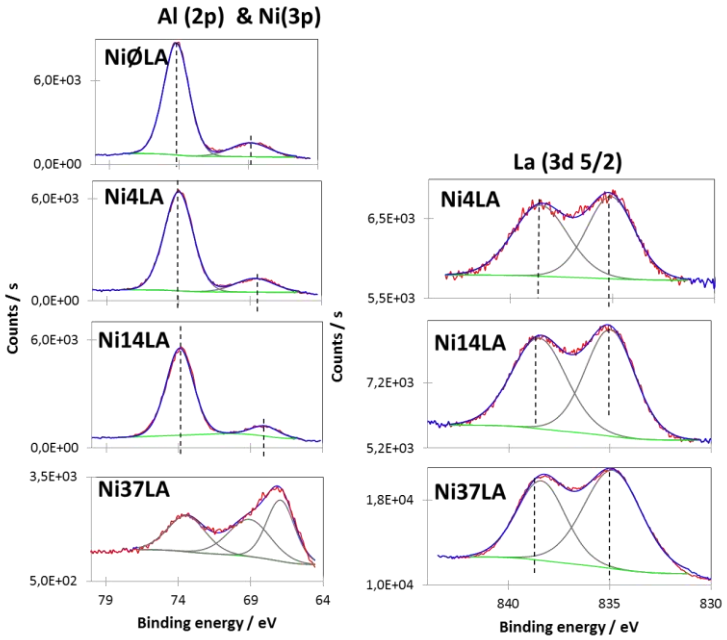

Figure 6.5. (left) Al(2p) and Ni (3p) regions (80-64 eV) and (right) La (3d 5/2) region (845-830 eV).

The XP spectrum of the NiA sample, in the Ni 2p3/2 region (830-865 eV) (Fig. 6.6), shows two main peaks at 856.1 and 862.3 eV which compare quite well with the spectra reported of $NiAl_2O_4$, Ni/Al_2O_3 samples [40, 41] and $LaNiAl_{11}O_{19}$ [38, 39]. They can be assigned to a Ni^{2+} main component and its satellite line (≈ 862 eV). For La and Ni containing samples, the XP spectra in the La 3d3/2 and Ni 2p3/2 region (830-860 eV) are partially overlapped (Fig. 6.6).

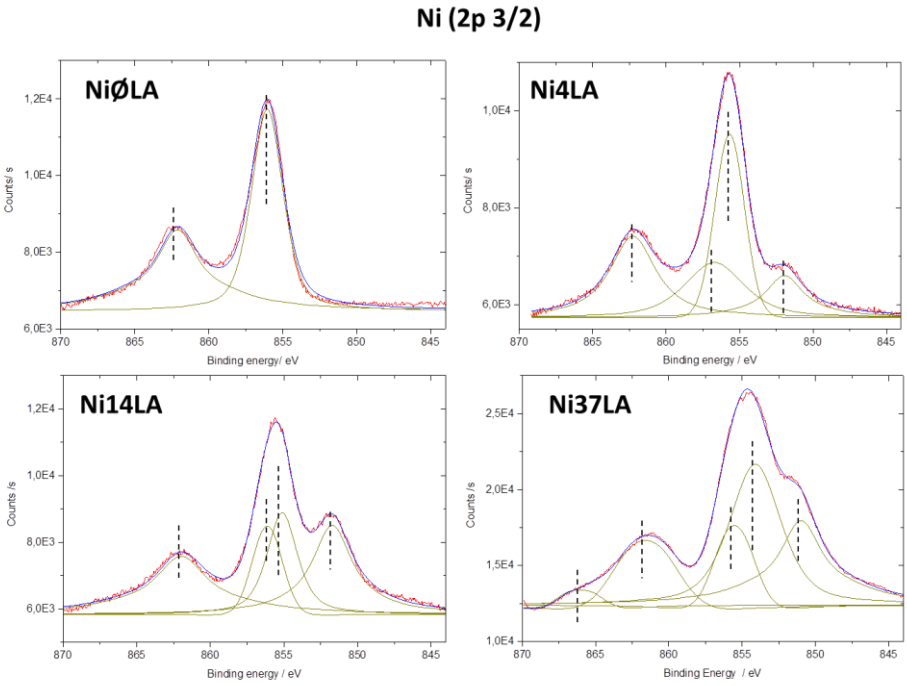

Figure 6.6. XP spectra of NixLA catalyst in the Ni(2p 3/2) region (870-845 eV).

The doublet due to La 3d3/2 (≈ 852 and 855.5 eV) increases in intensity with increasing Lanthanum loading (as expected), while the Ni 2p3/2 doublet shifts slightly and progressively to lower energies down to about 855 and 861 eV. This behavior confirms some interaction occurs between Ni^{2+} and La^{3+} centers. The low binding energies of Ni2p3/2 observed in Ni37LA can be assigned to the presence of NiO with the characteristic peak at 853.7 eV [13]. On Ni37LA, an additional peak is clearly observable at 866 eV and it is assignable to the plasmon component of La [42], not detectable for low-loaded lanthanum catalysts. By looking at the surface elemental composition, coming from XP spectra of the as prepared catalysts (Table 6.2), it is possible to detect that the addition of lanthanum on Ni4LA is at the expense of surface Al, not of nickel. This indicates that, in the case of this sample, the addition of lanthanum allows to nearly complete the surface “monolayer” of supported species on the alumina surface. In the case of Ni14LA also the surface Ni is slightly reduced but the Ni-alumina interaction is still nearly intact. A completely different situation is found for the Ni37LA sample where, in agreement with XRD data, alumina reacts with lanthanum and nickel oxide species.

Table 2: Composition of reduced catalysts (design and EDX compositions) and on the as prepared catalysts (XPS composition).

	Design composition			EDX composition			XPS surface composition				H_2/Ni
	Ni wt.%	La wt.%	Al wt.%	Ni wt.%	La wt.%	Al wt.%	Ni	La	Al	O	From TPR
	w_{Ni}/w_{cat} [%]	w_{La}/w_{cat} [%]	w_{Al}/w_{cat} [%]	w_{Ni}/w_{cat} [%]	w_{La}/w_{cat} [%]	w_{Al}/w_{cat} [%]	at.%	at.%	at.%	at.%	[-]
NiØLA	13.6	-	45.7	13.5	-	39.0	3.9	-	45.0	51.0	1.18
Ni4LA	13.6	3.5	43.5	13.0	3.0	37.0	4.1	0.7	44.7	50.6	1.17
Ni14LA	13.6	12.4	38.0	14.0	9.5	35.5	3.0	2.5	40.3	51.6	1.14
Ni37LA*	13.6	32.7	25.4	20.5	32.0	15.5	21.2	13.2	18.5	45.6	1.11

For Ni37LA* catalyst composition might be not representative for the inhomogeneities of the sample.

6.2.1.5. IR surface characterization of unreduced catalysts.

In Fig. 6.7, left, the IR spectra of the surface hydroxyl groups of the samples are compared. It is evident that the addition of lanthanum as well as of nickel causes the decrease of the intensity of the OH stretching bands of the surface hydroxyl groups.

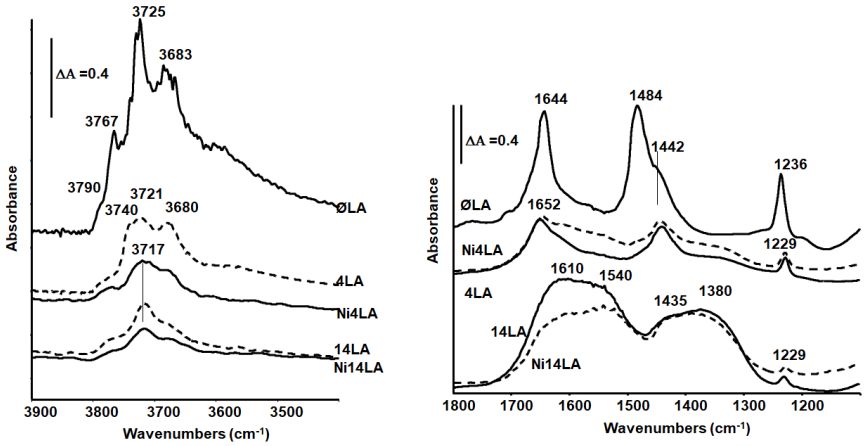

Figure 6.7. (left) IR spectra of xLA and NixLA in the OH region and (right) IR spectra of xLA and NixLA catalysts upon CO_2 adsorption.

This is in line with a progressive coverage of the alumina surface. In Figure 6.7 right, the spectra of carbonate species resulting from CO_2 adsorption and short outgassing at r.t. are reported. The

spectrum observed on bare alumina is due to two types of hydrogencarbonate species (ν_{as} COO at 1644 cm^{-1}, ν_{sym} COO split at 1484 and 1442 cm^{-1}, δOH at 1236 cm^{-1}), as reported many times [9, 10]. The spectra of both 4LA and Ni4LA show the bands of one hydrogencarbonate type only, indicating that the deposition of Lanthanum is "selective" and "poisons" the more active AlOH and Al^{3+}-O^{2-} acido-basic couples of alumina, as discussed elsewhere [3]. The addition of Ni to 4LA causes a slight decrease of the above bands and the appearance of broader bands near 1540 and around 1400 cm^{-1}, likely due to bidentate (bridging or chelating) species. In the case of 14LA and Ni14LA samples, the bands of hydrogencarbonate species are still present but much lowered in intensity; in particular, a weak feature at 1229 cm^{-1} is still evident. This suggests that a small fraction of alumina is still exposed at the surface. However, additionally, strong bands due to carbonate species are also observed. Two couples are observed, i.e. at 1610, 1380 cm^{-1} and at 1540, 1435 cm^{-1}. Outgassing at r.t. (data not reported) shows that the former couple is associated with a more weakly adsorbed species while the latter is associated with a stable species. The former couple decreases in intensity by further adsorbing Nickel, while the latter does not seem to be modified by nickel addition.

The above data suggest that in the case of Ni4LA the addition of Nickel mostly shifts a large part of lanthanum from the strongest alumina sites (where they do not form basic sites) to weaker ones, generating La-O basic sites adsorbing CO_2 as carbonates. On 14LA, a large part of lanthanum forms basic sites where CO_2 is adsorbed as carbonate species. Addition of Nickel on 14LA producing Ni14LA causes the decrease of the number of the La-O sites producing carbonates species not stable at the surface. This suggests that Ni displaces lanthanum from alumina sites where it produces weak basic sites, causing its agglomeration.

6.2.1.6 H_2-Temperature Programmed Reduction (H_2-TPR).

H_2-TPR data are reported in Fig.6.8 and the obtained H_2 consumptions are included in Table 6.1. In all cases, with the exception of Ni37LA, only one peak is present and it is centered at 1073 K corresponding to a complete reduction of well dispersed Ni oxidized species to the metallic state. A careful look to H_2/Ni ratio (Table 6.2) points out a slight apparent excess of hydrogen consumption with respect to the expected 1:1 stoichiometry (assuming Ni as Ni^{2+}), that might be due to possibly adsorbed (on Ni) and spillover hydrogen [43]. For NiØLA, Ni4LA and Ni14LA, the reduction onset is observed near 740 K. The high reduction temperature identified in these samples indicates the presence of poorly reducible Ni species, strongly interacting with the support, in accordance with

the XRD and UV-vis findings. This is typical of Ni/Al_2O_3 systems [17]. Only in the case of Ni37LA, the quite complex peak associated with reduction of free NiO, typically centered at 500-800 K, is observed even if it could be partially overlapped with the one arising from methane production by reduction of surface carbonate species [44].

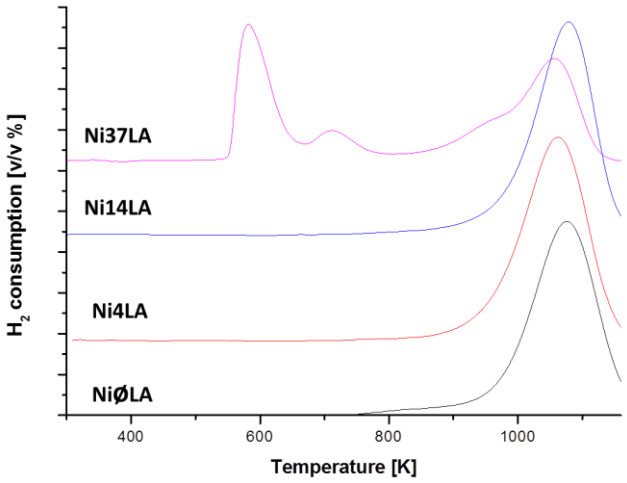

Figure 6.8. H_2-TPR profiles of the investigated NixLA catalysts.

6.2.1.7 FE-SEM of reduced catalysts.

The reduced catalysts were characterized by means of FE-SEM equipped with EDX microanalysis. Catalyst composition was determined by EDX at very low magnification and the results are summarized in Table 6.2. Ni, La and Al loadings, determined experimentally, are in line with those designed and expected for the prereduced catalysts, although Al compositions are usually underestimated respect to nominal bulk composition values, especially at increasing La_2O_3 loading.

The images obtained with backscattered electrons (BSE) show that the heavier elements, Ni and La, are homogeneously distributed in the case of unreduced NiØLA, Ni4LA and Ni14LA (pictures are not shown here, because there is no contrast in the images). In contrast, as depicted in Figure 6.9, the images of prereduced catalysts show clearly small bright particles of metallic Ni nanoparticles with a narrow particle size distribution and an average diameter lower than 10 nm, whose size agrees with that calculated from the XRD peaks using the Scherrer method. Lanthanum also is homogeneously distributed on catalysts surface; in fact, particles morphology and dimensions do not change passing from NiØLA to Ni14LA. A completely different situation is observed for the

sample with the highest La_2O_3 loading, i.e. Ni37LA, where the catalyst morphology is completely changed from a globular-like structure to a sponge like one (Figure 6.9, secondary electron micrograph (SE) and in the inset BSE one). In this case, a La-rich globular phase, with an average diameter of 10-30 nm, covered quite completely the sample surface. For this reason, the EDX analyses of this sample quantify a lower Al content than the expected.

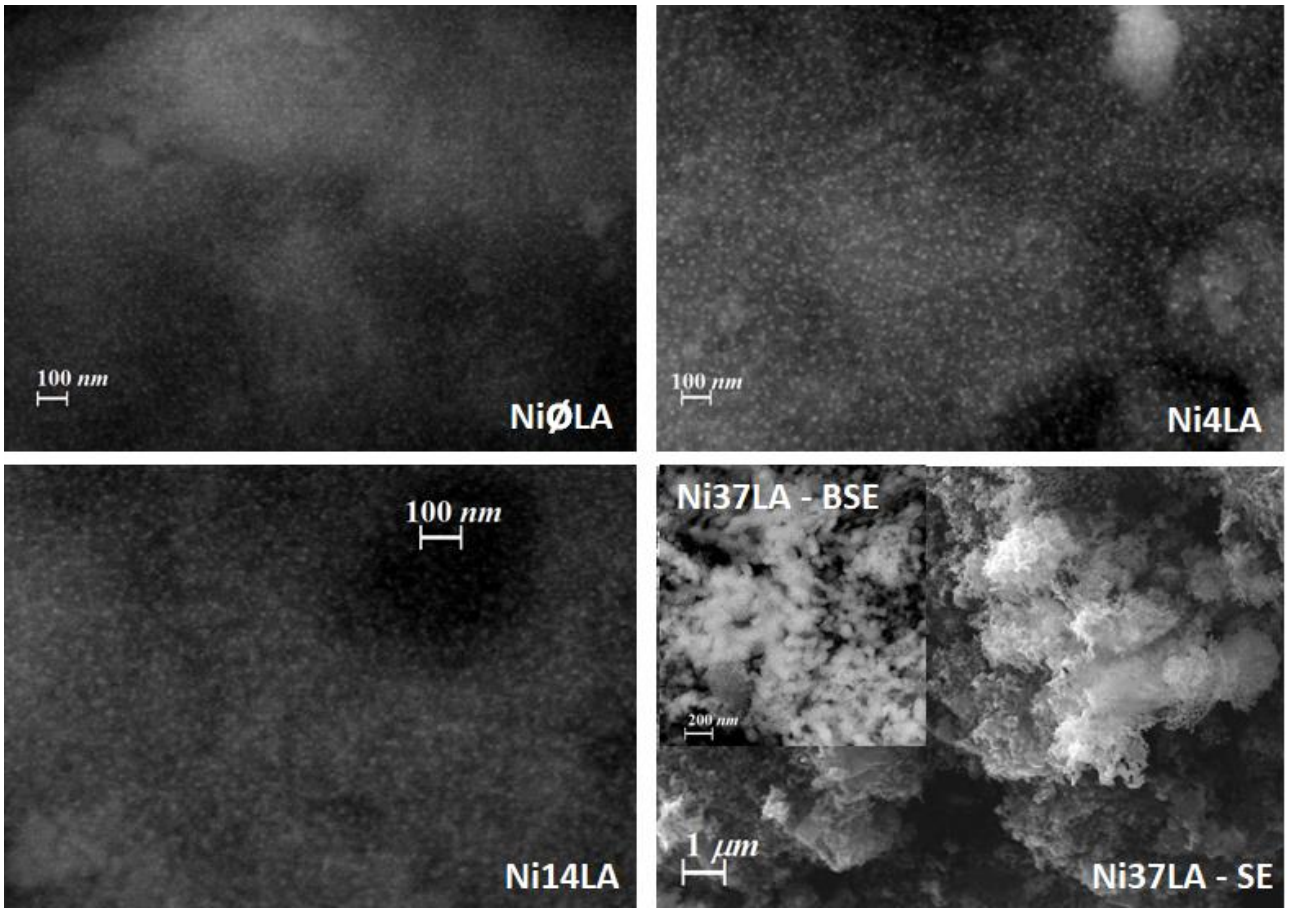

Figure 6.9. FE-SEM micrographs acquired in BSE electrons for NixLA catalysts (x= 0, 4 and 14). In Ni37LA secondary electron images is reported and correspondingly the BSE image in the bright region is included in the inset.

6.2.2 Catalytic activity studies

6.2.2.1 Catalytic activity in CO_2 methanation

In Figure 6.10, the catalytic activity in terms of CH_4 and CO yields for all the investigated catalysts is reported. In the same figure, the values corresponding to thermodynamic equilibrium are as well included. No other C-containing products are observed. The thermodynamic equilibrium has been

evaluated in the applied experimental conditions by using a Gibbs reactor and Soave – Redlich – Kwong equation of state.

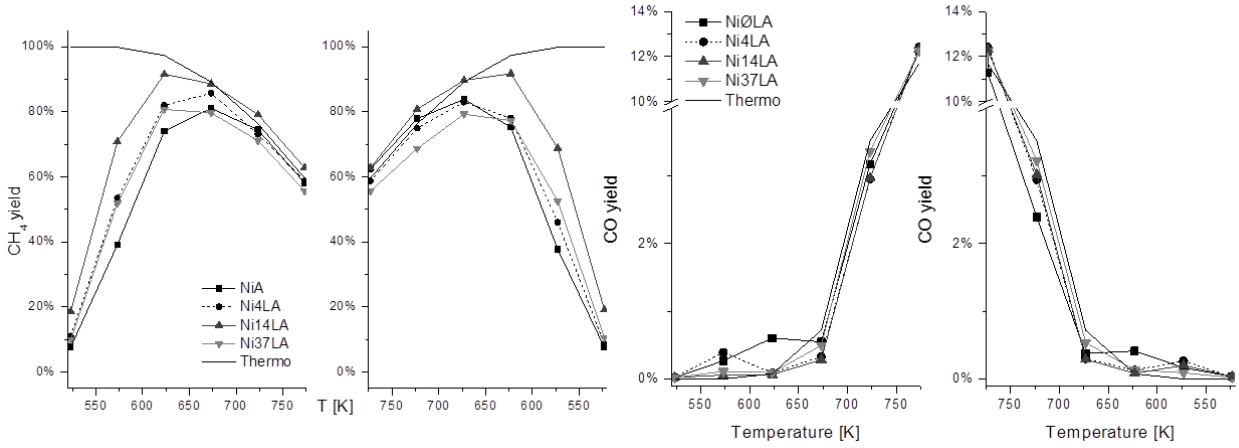

Figure 6.10 Methane and CO yields obtained in CO_2 hydrogenation for prereduced NixLA catalysts (symbols) in the 523-773 K temperature region with the comparison of thermodynamic equilibrium values. Experiment conditions: 6% CO_2, 30% H_2, N_2 balance and a total flow rate of 80 Nml/min, atmospheric pressure.

It has been verified that, in our conditions, no carbon deposition is expected by thermodynamics. At temperatures lower than 623 K, the observed CO_2 conversion and CH_4 yields are much lower than that allowed by thermodynamics, and significant differences in between the investigated catalysts can be observed. This agrees with a kinetically controlled regime. Instead, above 673 K the regime is roughly thermodynamically- controlled in all cases. At the same temperature in increasing and decreasing temperature experiments, CO_2 conversion is nearly constant for NiØLA, Ni4LA and Ni14LA, thus excluding detectable deactivation and/or conditioning effects. In the kinetically-controlled regime the activity follows the order: Ni14LA >Ni4LA ≈ Ni37LA >NiA suggesting that lanthanum addition is beneficial for CO_2 hydrogenation activity, with the best composition of near 14 wt.% La_2O_3. Ni14LA is also the catalyst that reaches thermodynamic equilibrium at the lowest temperature (673 K). Methane is found as the main product at low temperature, where the reaction is under kinetic control, with a selectivity approaching 100% at $T \leq 623$ K in particular on the most active Ni14LA catalyst, where the methane yield is around 90 % at 623K (with undetectable CO amount). Thus, in these conditions, only the Sabatier reaction (reaction 1) is observed

$CO_2 + 4H_2 \rightarrow CH_4 + 2H_2O$ (1)

CO production is nearly zero at low temperatures over the La-containing catalyst, but is non-negligible over the La-free catalyst. At higher temperatures (> 700 K), where the reaction is under thermodynamic control CO is also detected as a by-product in amounts approaching those expected by thermodynamics over all catalysts.

It must be considered that the reverse water gas shift reaction (reaction 2).

$CO_2 + H_2 \rightarrow CO + H_2O$ (2)

producing CO from CO_2 hydrogenation, is an endothermic equilibrium reaction, that, however, may allow significant CO_2 conversion to CO in the range 523-623 K. However, both CO and CO_2 methanation are favored in the same low temperature range, and this is the reason why CO production from CO_2 hydrogenation can be very selective to CH_4 in the presence of very active methanation catalysts. Thus, it is evident that lanthanum addition certainly strongly enhances the methanation rate with respect to La-free catalyst.

6.2.2.2 *Evaluation of reaction order and apparent activation energies*

In Figure 6.11, the determination of reaction orders for CO_2 and H_2 in the condition of a differential reactor with CO_2 conversions generally lower than 13% and where approach to equilibrium can be neglected. The rate data have been fitted with a simple power law expression [45] in the form:

$$r_{CH4} = k * p_{H2}^{\alpha} p_{CO2}^{\beta}$$

and the determined reaction orders are summarized in Table 3. This expression is considered an excellent model in differential studies [46] even though not suitable in the entire range of operation conditions. As a function of the lanthanum loading the reaction order of H_2 (α) slightly increases while for β, reaction order of CO_2, a progressive decrease from 0.20 to 0.14 is observed, suggesting a stronger interaction of CO_2 when lanthanum is introduced in the catalyst formulation, likely due to a stronger adsorption of CO_2 on the catalyst surface. In the case of the most active catalyst, Ni14LA, CO_2 methanation kinetics was investigated at 493 K. The reaction orders, evaluated in this case, are different from those evaluated at 523 K (α=0.28 and β=0.14), suggesting that a non-negligible temperature dependence is present for both reaction orders. The behavior is similar to the one previously reported by Weatherbee and Bartolomew [45] for low-loading Ni/SiO_2 catalysts. In particular, also in this case, the CO_2 order decreases with a temperature increase, while H_2 reaction order increases with a temperature increase.

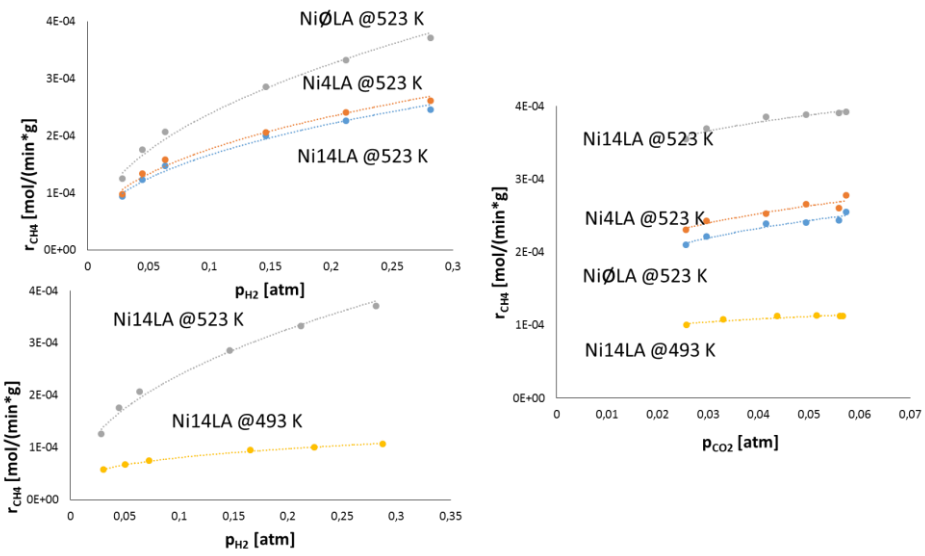

Figure 6.11. (left) Methane production rate as a function of H_2 partial pressure in kinetic evaluations for NixLA catalysts and (right) Methane production rate as a function of CO_2 partial pressure.

In Figure 6.12, the Arrhenius plot for the tested catalysts is reported. In all cases, the apparent activation energies are in the range of 70-85 kJ/mol, proper of a true kinetic regime with a negligible contribution due to diffusional limitations. Those values are in agreement with apparent activation energies reported on Ni/Al_2O_3 (E_a=80 kJ/mol) [2, 8] and more realistic than values reported on a recent paper of Ni modified lanthanum hydrotalcite catalysts where value of 1.4-1.6 kJ/mol were obtained, typical of a diffusion limited regime [47].

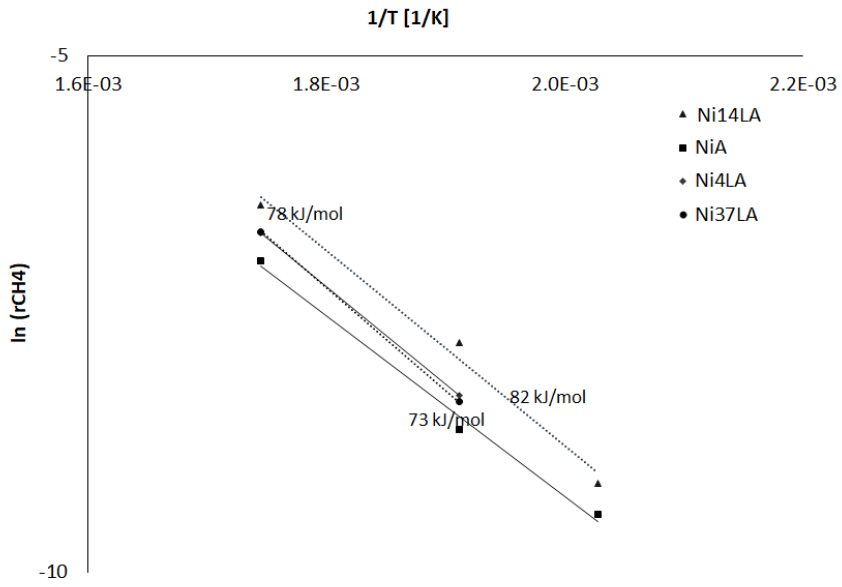

Figure 6.12. Arrhenius plot for evaluation of apparent activation energies.

6.3. Discussion

The data reported here show that all NixLA catalysts are active for the CO_2 hydrogenation at atmospheric pressure and in excess hydrogen conditions. The La-free catalyst tested here is more active than a 20% Ni/γ-Al_2O_3 commercial catalyst tested in the same conditions as reported in our previous work [8] despite the lower nickel content in our preparation. However, it must be taken into account that while our material was prepared by incipient wetness impregnation on the support powder, industrial catalysts preparation can be made by impregnation of support extrudates. Thus, in the industrial case, Ni loading may be higher at the surface of the pellet and lower in the center of it, thus the nominal Ni loading is the average of highly loaded particles and almost pure alumina.

A slight reduction of the activation energy is observed for our catalyst with respect to commercial Ni-γ-Al_2O_3 catalyst further confirming the catalytic activity data. Similarly, small differences are observed in the estimated reaction orders where a slight increase is observed for both the H_2 and CO_2 reaction orders 0.41 for H_2 and 0.20 for CO_2 with respect to the ones determined for commercial Ni/Al_2O_3 catalyst [8]. Our values are also higher than those reported for coprecipitated Ni/Al_2O_3 catalysts [46].

Moderate lanthanum addition (4 and 14 wt.% La_2O_3) does not modify the Ni reduction profile. This suggests that, still, a strong interaction between metal and support is present as suggested also from the UV-vis data where the typical components of Ni^{2+} species were found. Moreover, the stable high surface area, compared to the support, confirms the beneficial effect of lanthanum addition in increasing the thermal stability of the alumina support. This feature is important due to the high exothermicity of the methanation reaction. In the case of all NixLA catalysts, prereduction gives rise to mainly metallic nickel particles with characteristic diameters lower than 10 nm, comparable to those reported for prereduced Ni16 on a Si stabilized alumina support [2**Errore. Il segnalibro non è definito.**] that were found to be extremely selective for methane with no CO coproduction.

Our data show that the introduction of Lanthanum in the catalyst formulation even at low loadings strongly increases the catalytic activity in the 500-630 K temperature region, with a simultaneous increase in methane selectivity to ~ 100%. These data roughly agree with the recent results reported by Rivero -Mendoza et al. [48] but disagree with those reported by Rahmani et al. [49] where

deactivation was observed for 2%La_2O_3-Ni/Al_2O_3 catalyst in CO_2 methanation. They are also in line with studies of CO methanation studies that reported an activation effect of lanthanum on Ni/Al_2O_3 [50] as well as on Ni/Mg-Al_2O_3 ex hydrotalcite catalysts [51]. The data also show a slight increase in the reaction order of CO_2, which can be attributed to an increased basicity, hence an increased adsorption strength of CO_2, on the support. This is in line with the data discussed by some of us years ago [52] and reported by recent authors for CO_2 methanation on alumina-supported metals [53, 54], suggesting that CO_2 adsorption takes primarily occurs on the alumina support. Additionally, a slight decrease is found of the reaction order of H_2 by addition of lanthanum, which may be in line with the easier hydrogenation of more strongly adsorbed CO_2, or with some effect of lanthanum on nickel in making easier the activation of hydrogen, that certainly occurs on the metal.

Previous studies from our laboratory [9, 10] have shown that the addition of lanthanum to alumina reduces the number of very active Al^{3+}-O^{2-} acido-basic surface sites and produces new basic sites probably of the La^{3+}-O^{2-} type [9]. IR data, visible spectroscopy data and Al (2p) XPS data show that, in the case of Ni4LA and Ni14LA, Ni strongly interacts with alumina surface producing a spinel-like surface layer as it does on bare alumina. This occurs by displacing pre-impregnated La-O species from the strongest alumina acido-basic sites to weaker ones, where their acidity is even stronger. However, both UV spectroscopy and Ni (2p 3/2) XPS data provide evidence of some interactions between La^{3+} and Ni^{2+} centers in the case of as prepared catalysts, that could result in some interaction also in the reduced catalysts. On the other hand, the Ni+La loading in Ni4LA is nearly the one needed to complete (theoretically) the monolayer coverage, while in the case of the Ni14LA sample this amount is (theoretically) by larger than that required for a monolayer, at least in the unreduced state. However, IR data of CO_2 adsorption suggest that, in both cases, a small fraction of alumina is still uncovered, thus the Ni species grow in 3-D, leaving some small alumina areas in between, in parallel to the partial recovery of the γ-Al_2O_3 XRD pattern upon reduction. Additionally, nickel species seems to strongly interact with the alumina surface irrespective of the lanthanum loaded.

The addition of lanthana, resulting in the formation of basic sites, which adsorb CO_2 more strongly, could be beneficial for CO_2 methanation because of the stronger adsorption of CO_2 on the support. This can occur because the support can act as a CO_2 reservoir, by adsorbing it as carbonate species, allowing easier spillover of CO_2 from the support to the Ni particles where reaction takes place, or because surface carbonates are hydrogenated by spillover of hydrogen. In any case, a stronger

basicity can explain a stronger adsorption of CO_2 and the (weak) trend to a lower reaction order with respect to CO_2.

On the other hand, as suggested by XPS and UV spectra of the unreduced catalysts, the presence of lanthanum species may also influence Ni particle formation. Wierbizcki et al. [47] proposed that an electronic interaction may occur among La species and Ni particles. In our case, we cannot draw definitive conclusions on the basis of the data available up to now. In any case, the decrease of the adsorption strength of hydrogen (as deduced by the increased reaction order with respect to hydrogen) and the increased methane selectivity are relevant, and may be due to increased hydrogenation activity.

It seems quite interesting that the catalytic activity of our Ni14LA catalyst is nearly the same or even slightly better than the activity of a commercial 3 wt.% Ru/Al_2O_3 catalyst tested in the same conditions: as an example, methane yield is 66% at 573 K on 3 wt.% Ru/Al_2O_3, while nearly 72 % on Ni14LA. While Ru/alumina catalysts can also be improved by promoters, it seems that robust and cheap Ni/alumina catalysts could be competitive with the much more expensive Ru- based catalysts, thus preferable for low-temperature for CO_2 hydrogenation.

6.4. *Conclusions*

The following conclusion points are drawn from the findings of this work:

1. Lanthanum addition strongly increases the activity of $Ni/\gamma\text{-}Al_2O_3$ for CO_2 methanation. In addition, selectivity to methane is increased up to nearly 100% at low temperatures, where the reaction is in the kinetic regime (T < 650K).
2. The CO_2 methanation reaction on La-doped $Ni/\gamma\text{-}Al_2O_3$ occurs with similar activation energies (80 kJ/mol), a slightly higher reaction order for hydrogen and a lower one for CO_2 than undoped $Ni/\gamma\text{-}Al_2O_3$.
3. Characterization data suggest that nickel oxide species interact with the alumina surface more strongly than lanthanum oxide. Thus, the impregnation of Ni species over lanthanum-alumina shifts lanthanum from the strongest acido-basic sites of the alumina surface (where they do not form basic sites) to weaker alumina sites (where they form stronger La-O basic sites).

4. It is proposed that lanthanum acts as a promoter because of the stronger basicity of the lanthana-alumina support allowing stronger adsorption of CO_2 as carbonates acting as reactant reservoirs, while activation of hydrogen on nickel is also slightly improved by the presence of La .
5. La-doped Ni/γ-Al_2O_3 catalysts are competitive with Ru/alumina catalysts for the selective CO_2 methanation at low temperatures and atmospheric pressure.

6.5. *References*

[1] C. Vogt, E. Groeneveld, G. Kamsma, M. Nachtegaal, Li Lu, C. J. Kiely, P. H. Berben, F. Meirer, B. M. Weckhuysen , Nature Catalysis, 1 (2018) 127–134.

[2] G. Garbarino, P. Riani, L. Magistri, G. Busca, Int. J. Hydrogen Energy 39 (2014) 11557-11565

[3] G. Garbarino, C. Wang, I. Valsamakis, S. Chitsazan, P. Riani, E. Finocchio, M. Flytzani-Stephanopoulos, G. Busca, Appl. Catal. B: Environ. 174 (2015) 21-34.

[4] S. Presto, A. Barbucci, M. P. Carpanese, M. Viviani, R. Marazza, J Appl Electrochem 39 (2009) 2257–2264 DOI 10.1007/s10800-009-9857-7

[5] S. Kang, D. Lee, S. Kwon, Aerospace Sci. Tech. 46 (2015) 197–203

[6] P. Alphonse, B. Faure, Micropor. Mesopor. Mat. 196 (2014) 191–198

[7] I. Valsamakis, M. Flytzani-Stephanopoulos, Appl. Catal. B: Environ. 106 (2011) 255-263.

[8] G. Garbarino, D. Bellotti, P. Riani, L. Magistri, G. Busca, Int. J. Hydrogen Energy 40 (2015) 9171-9182.

[9] G. Garbarino, C. Wang, I. Valsamakis, S. Chitsazan, P. Riani, E. Finocchio, M. Flytzani-Stephanopoulos, G. Busca, Appl. Catal. B: Envir. 200 (2017) 458–468

[10] G. Garbarino, R.P, Parameswari Vijayakumar, P. Riani, E. Finocchio, G. Busca, Appl. Catal. B: Environ. 236 (2018) 490-500

[11] “Pearson Crystal Data: Crystal structure database for inorganic compounds”, Release 2009/2012, ASM International, The Material Information Society

[12] G. Busca , V. Lorenzelli, V. Sanchez Escribano, Chem. Mater. 4 (1992) 595-605

[13] G. Garbarino, P. Riani, A. Infantes-Molina, E. Rodríguez-Castellón, G. Busca, Appl. Catal. A: Gen. 525 (2016) 180-189

[14] G. Busca, P. Riani, G. Garbarino, G. Ziemacki, L. Gambino, E. Montanari, R. Millini, Appl. Catal. A: Gen. 486 (2014) 176-186.

[15] G. Garbarino, S. Campodonico, A. Romero Perez, M. M. Carnasciali, P. Riani, E. Finocchio, G. Busca, Appl. Catal. A: Gen., 452 (2013) 163-173.

[16] G. Busca, Heterogeneous Catalytic Materials, Elsevier, 2014, pp. 318-321.

[17] G. Garbarino, I. Valsamakis, P. Riani, G. Busca, Cat. Comm. 51 (2014) 37-41

[18] A.M. Hofmesiter, E. Keppel, A.K. Speck, Mon. Not. R. Astrom. Soc. 345 (2003) 16-38.

[19] M. Andrés-Vergés, C.J. Serna, J. Mater. Sci. Lett. 7 (1988) 970-972

[20] V. Biju, M. Abdul Khadar, Spectrochim. Acta Part A 59 (2003) 121-134

[21] M. Daturi, G. Busca, R.J. Willey, Chem. Mater. 7 (1995) 2115-2126.

[22] B. Klingenberg, M.A. Vannice, Chem. Mater. 8 (1996) 2755–2768

[23] R. Sarbajna, A.S. Devi, K. Purandhar, M.V. Suryanarayana. Int. J. ChemTech Res. 5 (2013) 2810-2820.

[24] M. Gil-Calvo, C. Jiménez-González, B. de Rivas, J. I. Gutiérrez-Ortiz, R. López-Fonseca, Appl. Catal. B: Environ. 209 (2017) 128-138.

[25] A. Tirsoaga, D. Visinescu, B. Jurca, A. Ianculescu, O. Carp, J. Nanopart. Res. 13 (2011) 6397-6408.

[26] Y. Li, S. Yao, W. Wen, L. Xue, Y. Yan, J. Alloys Compounds 491 (2010) 560–564

[27] C.E. Moffatt, B. Chen, D.M. Wieliczka, M.B. Kruger, Solid State Commun. 116 (2000) 631-636.

[28] Y. Kameshima, A. Yasumori, K. Okada, J. Surf. Sci. Soc. Jpn, 21 (2000) 481-487.

[29] F. S. Ohuchi, S. Ghose, M. H. Engelhard, D.R. Baer, American Mineralogist, 91 (2006) 740-746.

[30] R. Lizarraga, E. Holmstrom, S. C. Parker, C. Arrouvel, Physical Review B 83 (2011) 094201.

[31] F. El Gabaly, K. F. McCarty, H. Bluhm, A. H. McDaniel, Phys. Chem. Chem. Phys., 15 (2013) 8334-8341.

[32] Xingkun Ning, Zhanjie Wang & Zhidong Zhang, Scientific Reports 5, Article number: 8460 (2015)

[33] G. Vovk, X. Chen, C. A. Mims, J. Phys. Chem. B 109 (2005) 2445-2454.

[34] M. Ferrandon, E. Björnbom, J. Catal. 200 (2001) 148–159.

[35] S. Mickevi˘cius, S. Grebinskij, V. Bondarenka, B. Vengalis, K. Sliuziene, B.A. Orlowski, V. Osinniy, W. Drube, J. Alloy. Compd. 423 (2006) 107–111

[36] Z. Boukha, L. Fitian, M. López-Haro, M. Mora, J.R. Ruiz, C. Jiménez-Sanchidrián, G. Blanco, J. J. Calvino, G. A. Cifredo, S. Trasobares, S. Bernal, 272 (2010) J. Catal. 121-130

[37] J. Zheng, X. Ren, Y. Song, X. Ge, React. Kinet. Catal. Lett. 97 (2009) 109-114.

[38] K. Ikkour, D. Sellam, A. Kiennemann, S. Tezkratt, O. Cherifi, Catal. Lett. 132 (2009) 213-217.

[39] Ke Zhang, G. Zhou, J. Li, K. Zhen, T. Cheng, Catal. Lett. 130 (2009) 246–253.

[40] E. Heracleous, A.F. Lee, K. Wilson, A.A. Lemonidou, J. Catal. 231 (2005) 159-171

[41] P. Salagre, J.L.G Fierro, F. Medina, J.E. Sueiras, J. Mol Catal A: Chem 106 (1996)125-134

[42] M.F. Sunding, K. Hadidi, S. Diplas, O.M. Løvvik, T.E. Norby, A.E. Gunnæs, J. Electr. Spectr. Related Phenomena 184 (2011) 399–408

[43] K. Polychronopoulou, A.M. Efstathiou, Catal. Today 116 (2006) 341-347.

[44] T.K. Phung, G. Garbarino, J. Ind. Eng. Chem. 47 (2017) 288-296

[45] G.D. Weatherbee, C.H. Bartolomew, J. Catal 77 (1982) 460-472

[46] F. Koschany, D. Schlereth, O. Hinrichsen Applied Catalysis B: Environmental 181 (2016) 504–516

[47] D. Wierzbicki, R. Baranc, R. Dębek, M. Motak, M. E. Gálvez, T. Grzybek, P. Da Costa, P. Glatzel, Appl. Catal. B: Environ. 232 (2018) 409–419

[48] D. E. Rivero-Mendoza, J.N. G. Stanley, J. Scott, K.-F. Aguey-Zinsou, Catalysts 6 (2016) 170; doi:10.3390/catal6110170

[49] S. Rahmani, M. Rezaei, F. Meshkani, J. Ind. Eng. Chem. 20 (2014) 4176–4182

[50] M. R. Gelsthorpe, K. B. Mok, J. R. H. Ross, R.M. Sambrook, J. Mol. Catal. 25 (1984) 253 - 262

[51] D. Wierzbick, R. Debek, M. Motak, T. Grzybek M.E. Gálvez, P. Da Costa Catal. Commun. 83 (2016) 5–8

[52] V. Sanchez-Escribano, M.A. Larrubia Vargas, E. Finocchio, G. Busca, Appl. Catal. A: Gen. 316 (2007) 68–74.

[53] X. Wang, Y.Hong, H. Shi, J. Szanyi, J. Catal. 343 (2016) 185–195

[54] L. Falbo, M. Martinelli, C. G.Visconti, L. Lietti, C. Bassano, P. Deiana, Appl. Catal. B: Environ. 225 (2018) 354-363

Chapter 7

Commercial calcium alumina supported nickel catalyst catalytic activity in CO_2 methanation and Methane Steam Reforming

As already mentioned in Chapter 1, Hydrogen is mostly produced today through steam reforming of natural gas [1, 2]. The main reaction is assumed to be represented by methane steam reforming (MSR), an endothermic equilibrium reaction:

$CH_4 + H_2O \leftrightarrows CO + 3H_2$ $\Delta H°_{298} = +206.63$ kJ/mol (1)

establishing together with the water gas shift (WGS) equilibrium

$CO + H_2O \leftrightarrows CO_2 + H_2$ $\Delta H°_{298} = -41.16$ kJ/mol (2)

resulting, at least formally, in a formal "global reforming reaction" (GRR)

$CH_4 + 2H_2O \leftrightarrows CO_2 + 4H_2$ $\Delta H°_{298} = +165.47$ kJ/mol (3)

thus producing a "syngas" containing H_2, CO, CO_2 and unreacted CH_4. Although most authors suppose that the reaction path implies MSR being the first step followed by WGS to give the "formal" GRR reaction, is also possible that GRR is the first real step followed by the reverse of WGS (rWGS) to give the "formal" MSR reaction. The reaction is usually realized at 773-1173 K, 30-50 bar. Typical methane steam reforming catalysts [3] contain 10-25 % wt Ni supported over a low-surface-area refractory oxide such as alpha-alumina, Mg aluminate spinel $MgAl_2O_4$, calcium aluminates and calcium-potassium aluminate $CaK_2Al_{22}O_{34}$. A typical effect of this reaction consists in the production of carbon residue, in particular "carbon whiskers" or nanotubes, which are cause of pressure drop and deactivation. The presence of additives in some commercial catalysts allows the reduction of the formation of carbon residues. In particular, potassium has a very positive effect in reducing the formation rate of carbon species, with the drawback of reducing slightly the catalytic activity of the catalyst [4].

Hydrogenation of CO_2 (H_{CO_2}) can produce several different products, among which methane and CO. Methanation reaction consists in the synthesis of methane from hydrogenation of CO_x. Formally, methanation of carbon monoxide (M_{CO}) is the reverse of MSR

$CO + 3H_2 \leftrightarrows CH_4 + H_2O$ $\Delta H°_{298} = -206.63$ kJ/mol (-1)

while methanation of CO_2 (MCO2) is formally the reverse of GRR

$CO_2 + 4H_2 \leftrightarrows CH_4 + 2H_2O$ $\Delta H°_{298} = -165.47$ kJ/mol (-3)

The M_{CO_2} reaction could result from the previous conversion of CO_2 into CO with the reverse water gas shift (rWGS)

$CO_2 + H_2 \leftrightarrows CO + H_2O$ $\Delta H°_{298} = -41.16$ kJ/mol (-2)

followed by CO methanation. Also for methanation, the real reaction path is still not fully established. It is still not clear whether gas-phase CO is an intermediate in M_{CO_2} (thus the reaction sequence is rWGS+MCO) or a final product (thus the M_{CO_2} reaction would be parallel to the rWGS+MCO sequence).

Methanation of CO-rich mixtures is performed industrially today to destroy carbon oxides impurities in hydrogen (low temperature methanation [5]) or to produce Substitute or Synthetic Natural Gas (SNG) [6,7] using syngases rich in carbon oxides, like those arise from coal gasification. Ni–based catalysts supported on high-surface-area Al_2O_3 [8,9,10] are largely used for these applications. These catalysts have also been reported to be active for methanation of CO_2-rich carbon oxides mixtures as well as for pure CO_2 methanation. In fact Ni metal catalysts are active for both steam reforming and methanations, according to the "micro-reversibility principle" [11], the difference in catalyst formulations being essentially associated to the different stability requirements, associated to the very different reaction conditions. While endothermic steam reforming must be realized at very high temperature (750-900 °C) with large excess of steam, hexothermic methanations are performed at much lower temperature (463-773 K) with hydrogen excess.

The methanation of CO_2-rich gases or of pure CO_2 in the presence of excess hydrogen is still not realized industrially [12]. It can be of interest in the future for the production of methane or methane-hydrogen blends from captured CO_2 as an element of "CO_2 Capture and Storage technologies" (CCS) to reduce the emissions of greenhouse gases, with producing useful compounds.

On the frame of our research group studies on hydrogen production and CO_2 methanation we wanted to test industrial steam reforming catalysts, both without and with potassium, as well as an home made methanation catalyst (HMMC), in both steam reforming of methane and methanation of CO_2. We also attempted modellization of our laboratory reactor for both reactions. Modellization of laboratory reactor can be viewed as a first step in developing a useful model to be applied to industrial reactors.

7.1 Experimental

7.1.1 Catalytic materials.

Commercial Catalysts A and B for MSR, both from XX, have been used. According to the literature [3,4,13], Commercial sample A catalyst contains ~13 % Ni wt over a calcium aluminate cement, probably with a Ca:Al ratio of about 1:5 [14].The surface area is 29 m^2/g. commercial sample B catalyst is a slightly alkalized version, doped with small amounts (1.8 % wt) of K_2O [3]. As a reference, a "home-made methanation catalyst" (HMMC) has been prepared. Siralox 5/170 (5% SiO_2 and 95% Al_2O_3) was used as the support with previous calcination at 1073 K for 5 h. The composition of this catalyst is also comparable with those of "pre-reforming" catalysts [3,15]. Nickel 39% wt was deposited through wet impregnation of an aqueous solution of $Ni(NO_3)_2*6H_2O$. The powder was dried at 363 K for 5 h and calcined at 1073 K for 5 h. XRD of the resulting catalyst, which has a surface area of 80 m^2/g, shows the feature of a nearly cubic spinel and of NiO. Characterization data on this catalytic material were reported previously [16].

7.1.2 *Catalytic experiments*

All catalytic experiments have been performed in steady state conditions on a tubular quartz flow reactor by loading 88.2 mg of catalyst diluted in silica glass particles 0.25–0.21 mm (corresponding to 60-70 mesh sieved, 440 mg for SR and 700 mg for methanation). .

The following feed gas composition has been used for MSR experiments: 5% CH_4, 20% H_2O, He balance, total flow rate 120 Nml/min, corresponding to GHSV = 81000 h^{-1} calculated on the catalyst volume. MSR product analysis was performed with a gas-chromatograph Agilent 4890 equipped with a Varian capillary column "Molsieve 5A/Porabond Q Tandem" and TCD and FID detectors in series. Between them, a nickel catalyst tube was employed to reduce CO_x to CH_4. Products analysis was also performed on GC/MS (FOCUS and ISQ from Thermo-Fisher), in order to have a precise identification of the compounds. The conversion of the reactants is defined as follows:

$$X_{reactant} = \frac{nreact.\,in - nreact.\,out}{nreact.\,in}$$

while selectivity to C-product i is defined as:

$$S_i = \frac{n_i}{\nu_i(nreact.\,in - nreact.\,out)}$$

where n_i is the number of moles of compound i, and ν_i is the ratio of stoichiometric reaction coefficients. The hydrogen yield, calculated on the basis of the GRR stoichiometry, is defined as:

$$Y_{H_2} = \frac{n_{H_2\ out}}{4 * (n_{methane\ in})}$$

For CO_2 hydrogenation the feed gas composition was: 6% CO_2, 30% H_2, N_2 balance, with 80 Nml/min total flol rate, 55000 h^{-1} GHSV calculated on the catalyst volume. In order to follow any hysteresis, activation or deactivation effects, CO_2 hydrogenation experiments were performed both in ascending and in descending reaction temperature steps (523 K, 573 K, 623 K, 673 K, 723 K, 773K and reverse). Temperature was controlled through a furnace.

Online products analysis was performed using a Nicolet 6700 FT-IR instrument. Frequencies where CO_2, CH_4 and CO molecules absorb weakly have been used (2293 cm^{-1} for CO_2, 2170 cm^{-1} for CO, 1333 cm^{-1} for CH_4, after subtraction of baseline water absorption) with previous calibration using gas mixtures with known concentrations, in order to have quantitative results. Produced water was condensed before the IR cell. From the inlet and outlet concentrations calculated from the absorbances of CO, CO_2, CH_4 and the measured inlet and outlet total flows (which allow to take into account the variation of the number of moles during the reaction), CO_2 conversion (X_{CO2}), selectivities and yields to products, S_i and Y_i, have been calculated [17]. They are defined as:

$$X_{CO2} = \frac{F_{CO2\ in} - F_{CO2\ out}}{F_{CO2\ in}} \quad (4);$$

$$S_i = \frac{F_i}{F_{CO2\ in} - F_{CO2\ out}} \quad (5);$$

$$Y_i = \frac{F_i}{F_{CO2\ in}} \quad (6);$$

where F_i is the molar flow rate of i (i.e. CO and CH_4), while F_{CO2} is the molar flow rate of CO_2 and they were all expressed in mol/min.

7.2 Results

In figure 7.1 the XRD patterns of the two commercial catalysts and the HMMC are reported.

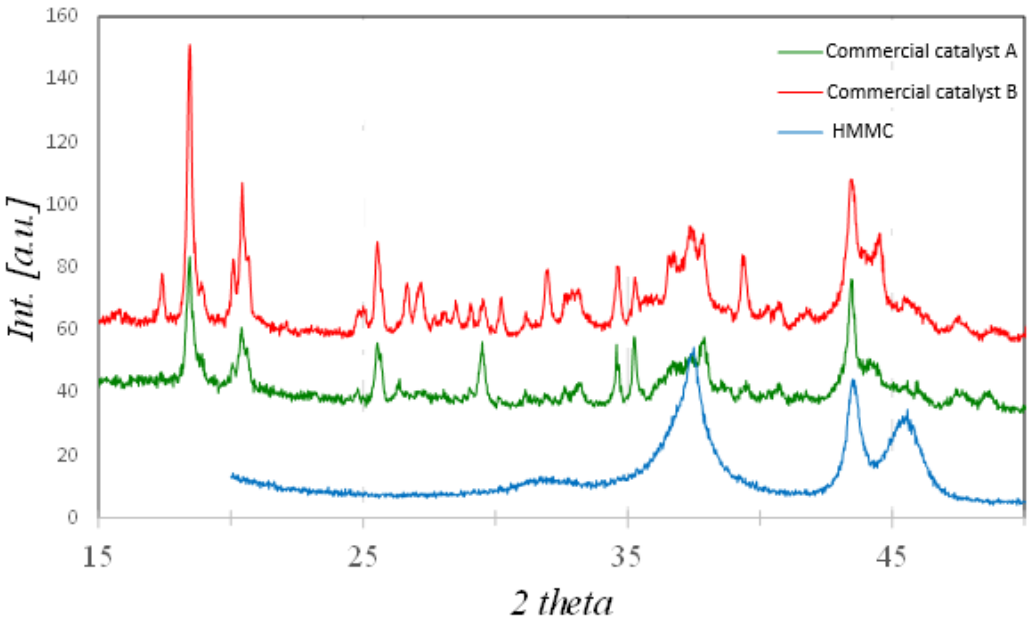

Fig.7.1: XRD patterns of the fresh catalytic materials.

The patterns of the two commercial catalysts are dominated by the features of a number of different calcium aluminate phases. Instead, that of the HMMC is typical of Ni-rich NiO-Al_2O_3 system.

7.2.1 Methane steam reforming.

In Fig. 7.2 the results of methane steam reforming experiments over the commercial catalyst A are reported.

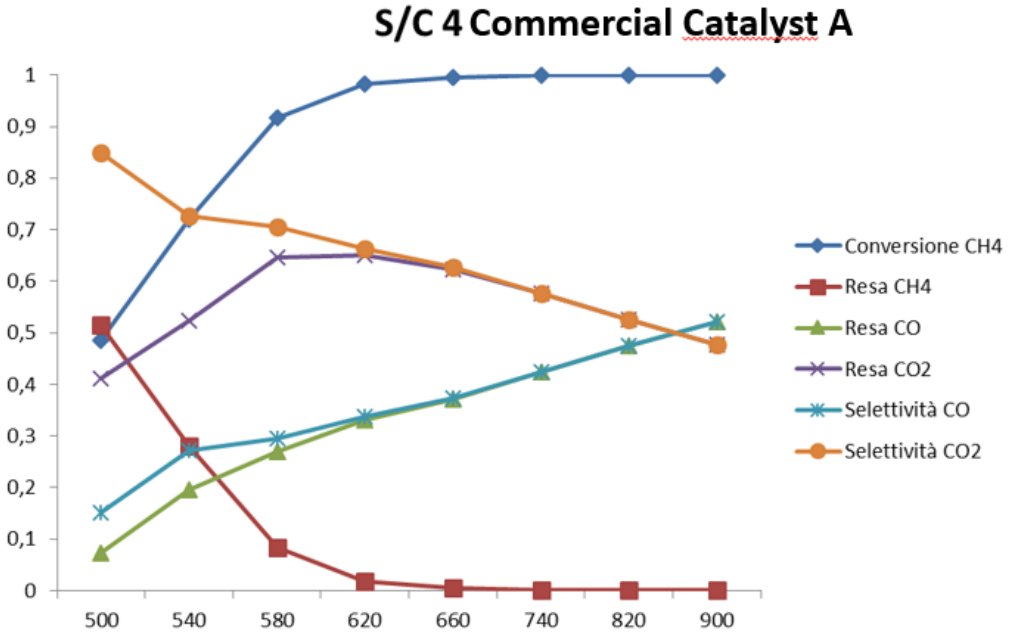

Fig.7.2: Methane Steam Reforming with descending ramp for the commercial catalyst A

Methane conversion is around 50 % at 773 K while approaches totality at 900 K and above.CO_2 selectivity declines progressively from 86 % at 773 K down to 66 % at 990 K and 50 % at 1173 K, with a corresponding increase of CO selectivity. As a result, hydrogen yield has a maximum of near 90 % around 900 K. No other products have been detected in significant amount. Comparison with thermodynamics shows that equilibrium conditions are approached at 573 K and nearly fulfilled at 623 K and above. At 500 and 543 K the reaction is certainly under kinetic control.

Conversion of methane over the K-doped catalyst, reported in Fig. 7.3, commercial catalyst B is lower than over the K-free catalyst below 1000 K, but with higher CO_2 selectivity (92 % at 773 K, 71 % at 990 K) and lower CO selectivity.

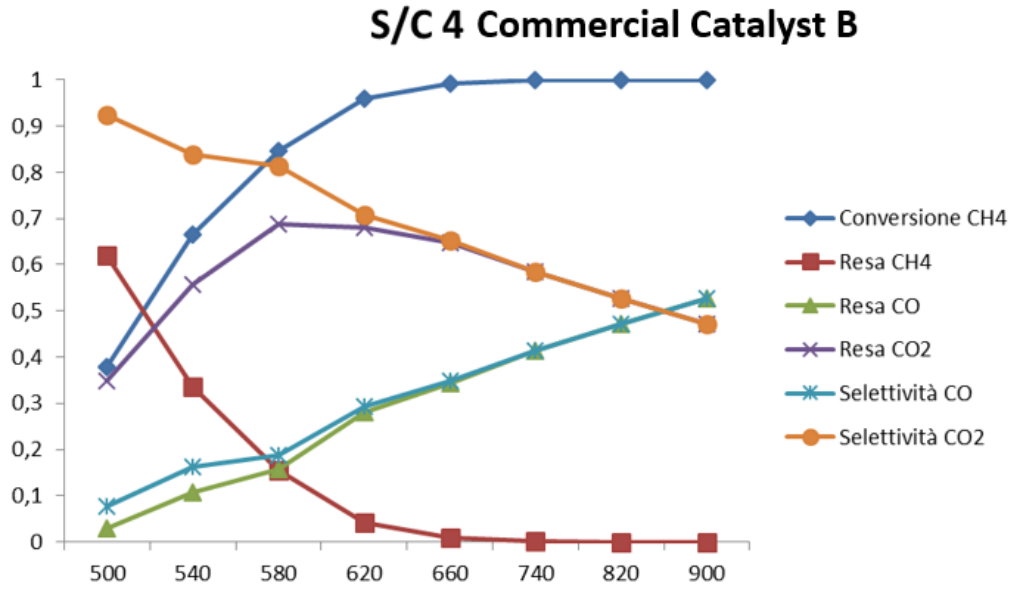

Fig. 7.3: Methane Steam Reforming with descending ramp for the commercial catalyst B

Hydrogen yield. Equilibrium conditions are approached at 623 K and above.

The reaction over the HMMC catalyst is faster in the temperature region, results of the MSR process for this catalyst are reported in Fig. 7.4.

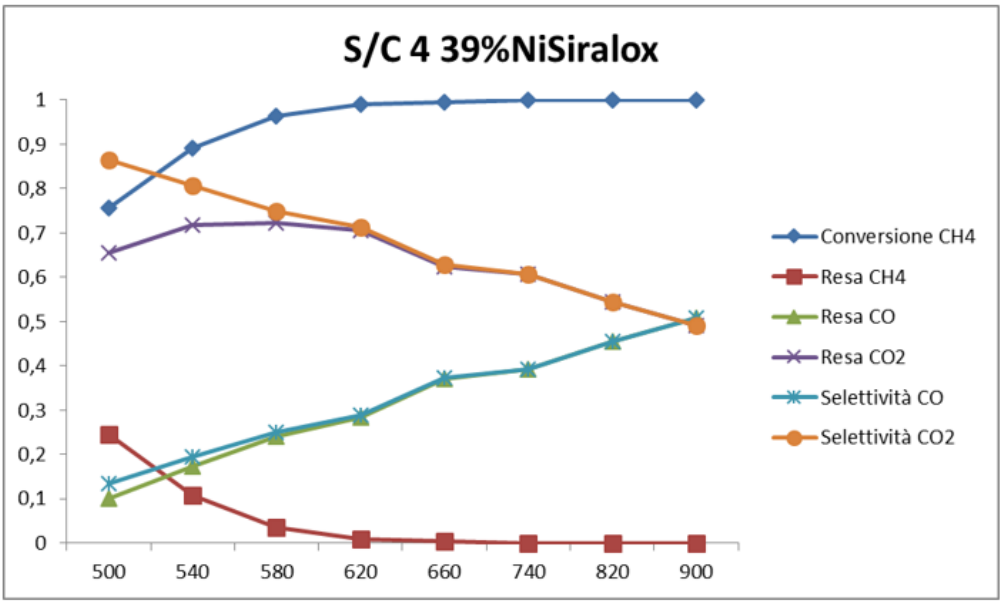

Fig. 7.4: Methane Steam Reforming with descending ramp for the HMMC.

Over this catalyst equilibrium conditions are already fulfilled at 773 K, where methane conversion is 76 %, and remains at equilibrium at the end of the experiment at 1173 K. The maximum hydrogen yield is that allowed by thermodynamics at 623 K, 95 %.

7.2.2 CO_2 methanation

The results obtained on methanation experiments are summarized in Fig.s 7.5-7.7. In the left sections, data obtained in stationary state upon increasing temperature, step by step, are reported, while in the right sections of the figures those data obtained in the same conditions but under step by step cooling are reported. In all cases, the trend of the concentrations of the products in the outflowing gas is constant at constant temperature, and a close correspondence occurs between the data recorded at the same temperature during the increasing and the decreasing temperature run. Thus, neither deactivation nor conditioning phenomena occur, in spite of the absence of any pretreatment.

The conversion of CO_2 over the K-free commercial catalyst A increases with increasing temperature up to T = 673 K (81 %) and then decreases. Selectivity to methane is total up to 773 K while CO is also increasingly coproduced at higher temperatures.

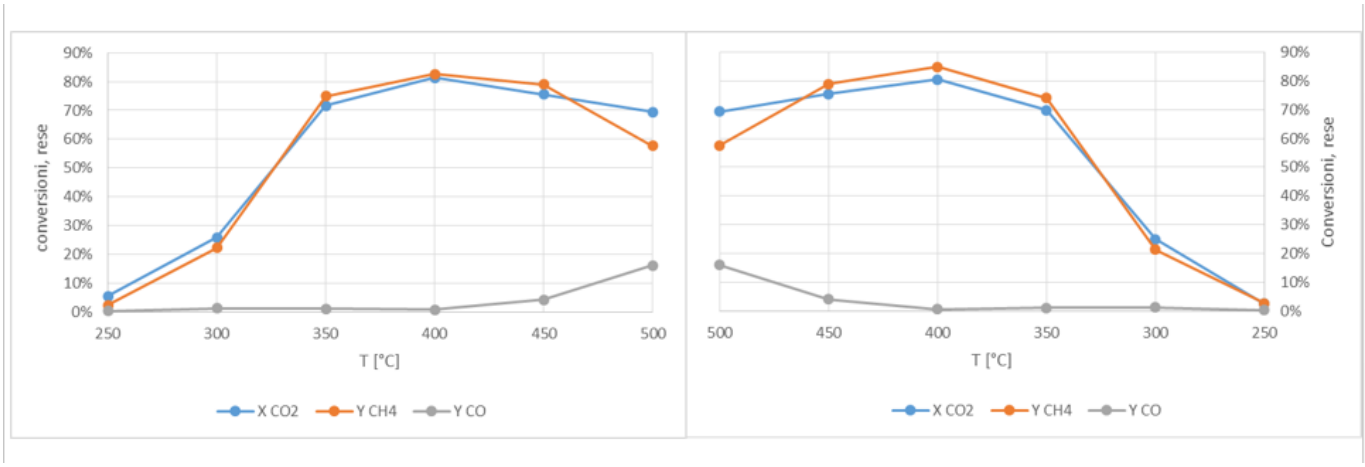

Fig. 7.5: CO_2 hydrogenation process results in terms of CO_2 conversion and CH_4, CO yield obtained using Commercial catalyst A

The comparison with the calculated thermodynamic equilibrium conditions [18], shows that reaction is near to thermodynamic control at 723 and 773 K, while conversion is under kinetic control at lower temperatures, when it increases with increasing temperature. The behavior is practically inversed by decreasing temperature showing that the catalyst does not undergo significant deactivation under these conditions.

The experiments have been repeated with the K-doped commercial catalyst B.

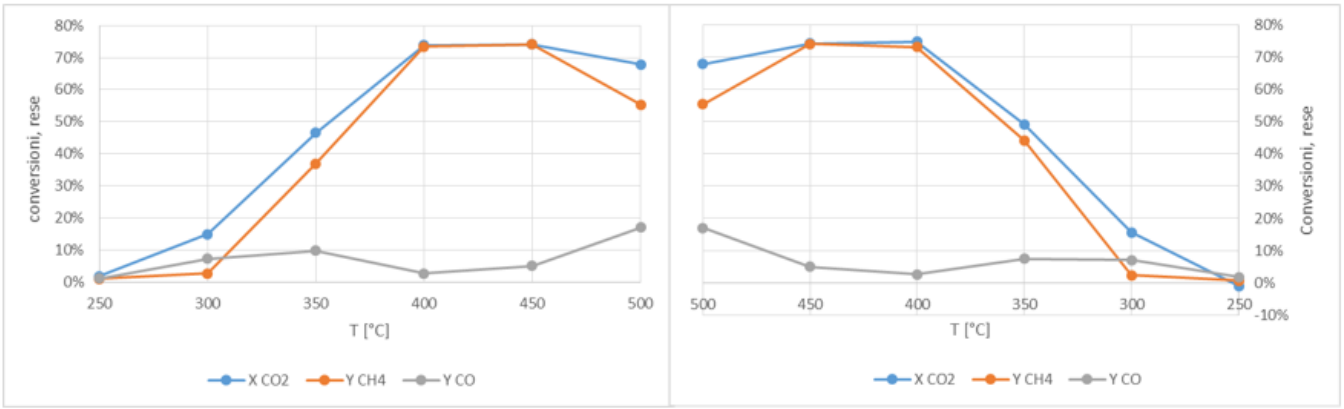

Fig. 7.6 CO_2 hydrogenation process results in terms of CO_2 conversion and CH_4, CO yield obtained using Commercial catalyst B

With this catalyst equilibrium is approached at 773 K but the system is under kinetic control at lower temperature. In this range, lower conversions are obtained at any temperature and also lower selectivity to methane is observed, CO being always coproduced. Over the HMMC catalyst equilibrium is approached again at 723 and 773 K. At lower temperatures (673 and 623 K) the CO_2

conversion is higher on HMMC than on the commercial catalysts and selectivity to methane is total.

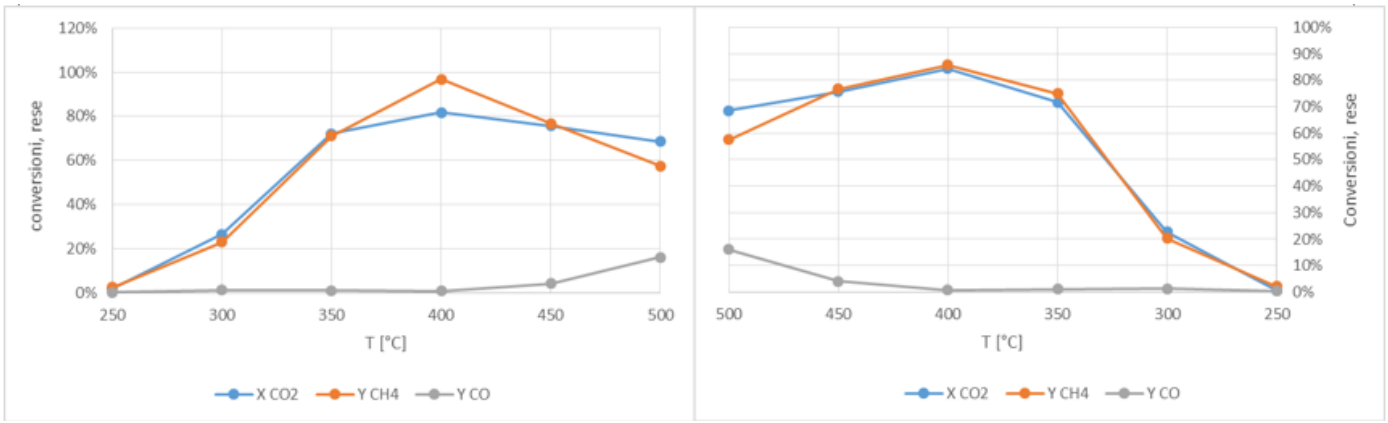

Fig. 7.7 CO_2 hydrogenation process results in terms of CO_2 conversion and CH_4, CO yield obtained using HMMC

The higher conversion obtained on HMMC than on B catalyst can be mainly associated either to the higher Ni loading or to the different support chemical composition.

In Table 7.1 the product compositions of the HCO_2 and MSR experiments both with 80 Nml/min feed follow rate are compared at 773 K. We indeed can see that while after HCO_2 over the three catalysts the reaction is very near equilibrium (taking into consideration experimental error), from SMR also at 80 Nml/min flowrate the reaction approaches equilibrium only over HMMC, while it is far from equilibrium over commercial catalyst A and, even more, over commercial catalyst B.

Table 7.1 catalytic results in MSR and CO_2 hydrogenation at 773K.

	Methane steam reforming					CO_2 hydrogenation			
	A	B	HMMC	Thermodynamic eq		A	B	HMMC	Thermodynamic eq
COout	0,3%	0,1%	0,5%	0,1%	COout	1,1%	1,1%	1,1%	0,8%
CO_2out	1,9%	1,7%	3,0%	3,0%	CO_2out	2,1%	2,1%	2,1%	1,9%
CH_4out	2,5%	3,1%	1,1%	1,3%	CH_4out	3,9%	3,6%	3,8%	3,8%
H_2out	8,7%	7,0%	13,5%	12,2%	H_2out	15,4%	16,2%	15,8%	16,2%
H_2Oout	15,3%	16,3%	12,2%	13,5%	H_2Oout	8,8%	8,4%	8,6%	8,5%

7.3 Discussion

The data reported in catalytic experiments show that the investigated catalysts are all active in both MSR and in CO_2 hydrogenation reactions. The data show that the HMMC catalyst is more active than both K-free and K-doped industrial MSR catalysts. The better activity of the HMMC catalyst is likely associated, for both reactions, to the definitely higher nickel loading, as well as, maybe, to the different support. It is evident that the composition of the industrial MSR catalysts are determined by the need of a very prolonged stability, both in terms of reduced sintering of both the nickel active phase and the support, and on a limited formation of carbon residues. Calcium aluminates are stable and refractory materials allowing to stabilize nickel particles in the SR reaction conditions, even if they can in some way slightly reduce the activity of nickel with respect to alumina. In any case, we remark that the HMMC catalyst does not show any deactivation in a one-day-long experiment in MSR in our conditions.

Our data confirm, also in our conditions, the slightly lower activity of the K-doped commercial SMR catalyst with respect to the K-free catalyst [4] in the MSR reaction. As said, K-doping is useful to reduce carbon residue formation, in particular when natural gas treated contains significant amounts of higher hydrocarbons, propane and butane. The formation of carbon is in fact much more pronounced when higher hydrocarbons are treated. For this reason, in industrial plants a pre-reforming reactor is frequently used [15], working at lower temperature (~ 773 K), to steam reform higher hydrocarbons before the tubular reactor. As remarked above our HMMC catalyst has a composition, which is comparable with that of pre-reforming catalysts. It seems interesting to remark that this catalyst, richer in nickel, is more active with respect to MSR even at 773 K, thus at a temperature where pre-reforming is usually conducted. Indeed, at this low temperature SR of propane and butane can already occur with high conversion and are much faster and favored than MSR.

It is however to be remarked that the selectivity to CO_2 is significantly higher, at low temperature when the SR reaction is under kinetic control, over the K-doped catalyst than over the others. This either indicates that K-containing catalysts are more active in water gas shift reaction (supposing CO is the primary product of the steam reforming process) or, in contrast, K-doping also poisons retro-water gas shift reaction (supposing CO_2 is the primary product of the reaction, and CO is the final product).

The three catalysts tested in MSR have also been tested in the reverse reaction, i.e. MCO_2. The trend of catalytic activity is the same for CO_2 hydrogenation and MSR, i.e. HMMC >

Commercial catalyst A > Commercial catalyst B, as it might be expected from the "micro-reversibility principle" [11]. In the cases of K-free catalysts, HCO_2 reaction is highly selective to methane (approaching 100 %) until 673 K, when the maximum conversion is reached, allowing a methane yield near 85 %. In these conditions, the reaction is still under kinetic control in our experiments, being CO_2 conversion still lower than that allowed by thermodynamics. At higher temperatures, however, when the reaction is, over these catalysts, already under thermodynamic control, CO is produced in significant amounts, as expected indeed by thermodynamics. A different situation is found over the K-doped catalyst, where conversion of CO_2 is significantly lowered with respect to undoped catalyst, and 10% amounts of CO is formed upon CO_2 methanation also at low temperature (i.e. when thermodynamics allows complete CO hydrogenation). This behavior shows that the rate of the "methanation" steps (CO_2 hydrogenation and CO hydrogenation) are both lowered by K-doping. However, the reduced CO_2 conversion implies that either also the rate of the rWGS activity is reduced by potassium doping (supposing CO_2 hydrogenation as the sequence rWGS+MCO) or CO_2 hydrogenation is mainly parallel to rWGS. These data can be taken into consideration in parallel with the effect of K-doping on the selectivity to CO_2 in MSR (see above). These data support the idea that a direct reversible way from CO_2 to CH_4, without the intermediacy of gas-phase CO, indeed exists and is predominant in both senses. Thus, CO_2 hydrogenation and GRR ((3) and (-3)) are real inverse reaction whose reaction rates are both slowed down by K doping in both directions. The increased selectivity to CO by the hydrogenation side and to CO_2 from the steam reforming side by K doping is a secondary effect: it indicates that rWGS reaction (-2) is both parallel to CO_2 methanation and consecutive to CH_4 steam reforming, and is hindered at least at high temperature by K doping.

On the other hand, it can be interesting to remark that we performed experiments in closely similar conditions at 773 K both feeding methane + water and feeding CO_2 + hydrogen. At this temperature, the reaction is under (or near) equilibrium conditions from both sides only on the HMMC catalyst. With the two industrial catalysts, at 773 K the reaction is, in our experiments, near equilibrium from the hydrogenation side, while is far from equilibrium from the steam reforming side. This is apparently in contrast with the "microreversibility principle". The easier explanation is that the state of the catalyst is not exactly the same in the two experiments. We can remind that the MSR have been recorded upon decreasing step-by-step the reaction temperature in a high steam feed, while HCO_2 reaction has been done by increasing step-by-step the reaction temperature. In this hypothesis it should be concluded that the two commercial catalysts would

be somehow deactivated during the higher temperature runs, in contrast to the HMMC catalyst that would be not. This is actually unlikely. An alternative possibility is that the two commercial catalysts suffer competition by water more than the HMMC catalyst. Thus, the excess of water could inhibit kinetically the reaction only over the commercial catalysts.

7.4 Conclusions

The data reported above, show that our HMMC is more active than industrial catalysts in the laboratory conditions, for both CO_2 methanation and MSR. This is likely associated to the higher Nickel content of the HMMC. It is however clear that the commercial catalysts are designed and optimized for very long time on stream processes in MSR, where catalyst stability is a dominant factor. The experiments are anyway in good agreement with the microreversibility principle showing that a catalyst which catalyze an equilibrium reaction, also catalyze the reverse reaction. However the data suggest that for the commercial catalyst the amount of water vapor in the reaction medium is critical and may affect reaction rate.

The data on commercial catalysts show that the presence of potassium decreases activity in both Co_2 methanation and steam reforming, but may also have an effect on the reaction rate relative to WGS/rWGS equilibrium.

7.5 References

[1] J.R. Rostrup Nielsen, J. Sehested, J.K. Nørskov, Hydrogen and synthesis gas by steam- and CO_2- Reforming, Advan. Catal. **47**, 66-141 (2002).

[2] K. Aasberg-Petersen, I. Dybkjær, C.V. Ovesen, N.C. Schjødt, J. Sehested, S.G. Thomsen Natural gas to synthesis gas - Catalysts and catalytic processes, J. Nat. Gas Sci. Eng. **3**, 423-459 (2011)

[3] C. H. Bartholomew, R.J. Farrauto, Fundamentals of Industrial Catalytic Processes, Wiley, 2006, p. 357.

[4] M. Carlsson, Carbon Formation in Steam Reforming and Effect of Potassium Promotion, Johnson Matthey Technol. Rev., 59, 313-318 (2015)

[5] http://www.topsoe.com/business_areas/ammonia/processes/methanation.aspx

[6] J. Kopyscinski, T.J. Schildhauer, S.M.A. Biollaz, Fuel, 89 (2010) 1763-1783.

[7] J. Gao, Q. Liu, F. Gu, B. Liu, Z. Zhong, F. Su, Recent advances in methanation catalysts for the production of synthetic natural gas, RSC Adv. **5,** 22759–22776 (2015)

[8] I. Wender, Fuel Proc. Technol. 48 (1996) 189-297.

[9] B.B. Pearce, M.V. Twigg, C. Woodward, in M.V. Twigg ed., Catalyst Handbook, 2nd ed., Wolfe pub. London, 1989, p. 340-383.

[10] J.Gao, Q. Liu, F. Gu, B. Liu, Z. Zhong, F. Su, Recent advances in methanation catalysts for the production of synthetic natural gas, RSC Adv., 5 (2015) 22759–22776

[11] R. Mauri, Non-equilibrium thermodynamics in multiphase flows, Springer, 2013, pp. 13-24.

[12] W. Wang, J. Gong, Methanation of Carbon Dioxide: An Overview, Front. Chem. Sci. Eng. 2011;5:2-10

[13] A. Adrados, A. lopez-Urionabarrenechea, E. Acha, J. Solar, B.M. Caballero, I. de Marco, Hydrogen rich reducing gases generation in the production of charcoal from woody biomass carbonization, Energy Conv. Manag. 148 (2017) 352-359.

[14] S.J.K. Forrest, J.G. Oliver, S. A. French, M. P. U. Carlsson, Catalyst preparation method, US patent application 2016/0375426 A1, to Johnson Matthey, 2016

[15] J. Cross, G. Jones, M. A. Kent, An introduction to pre-reforming catalysis, Nitrogen+Syngas 341 (May-June 2016) 40-48.

[16] G. Garbarino, S. Chitsazan, T.K. Phung, P. Riani,, G. Busca, Preparation of supported catalysts: A study of the effect of small amounts of silica on Ni/Al_2O_3 catalysts, Appl. Catal. A: Gen. 505 (2015) 86–97

[17] O. Levenspiel, Chemical Reaction Engineering, 3rd ed., Wiley, New York, 1999, p.87.

[18] G. Garbarino, Methanation of carbon dioxide on Ru/Al_2O_3 and Ni/Al_2O_3 catalysts at atmospheric pressure: Catalysts activation, behaviour and stability, Int. J. Hydr. En. 40 (30) (2015) 9171-9182

Chapter 8

Conclusions

From the experiments above described, we can draw the following conclusions:

- Both Nickel and Cobalt based catalysts are very active in Ethanol Steam Reforming (ESR) at 773K and above. However, the catalytic activity is affected by the presence of boron impurities, residual from the preparation methods (metal reduction with $NaBH_4$) for unsupported metal nanoparticles. In particular, the presence of borate species give rise to weak but stable catalytic activity, while the presence of borides give rise to very active catalysts that loose activity upon aging. The addition of Nickel to Cobalt improves the catalytic activity allowing yields in H_2 of 83% at 773K and GHSV 324000h^{-1}. The performances of unsupported (Co,Ni) bimetallic NPs, appears to be even better than those conventional supported catalysts. However, carbonaceous materials are present both as carbon nanotubes and graphitic carbon after catalytic reaction.

- Silica supported Co catalysts also shows high activity in ESR but may deactivate forming large Co containing particles partially embedded in the silica/cobalt silicate surface. This species are not active in ESR but are also not active in producing carbon nanotubes in any case silica gel is shown to be not an efficient support for Co ESR catalysts.

- It is confirmed that Nickel alumina is a good catalyst for CO_2 methanation. I have shown here that Lanthanum doping of the alumina support increases significantly the activity of Nickel alumina for CO_2 methanation as showed before also for ESR. The Ni@La_2O_3/Al_2O_3 catalyst appear to be competitive with the more active but also more expensive Ru @Al_2O_3 catalyst and result to be substantially stable in our laboratory conditions and upon times on stream on the order of 8 hours. The higher catalytic activity of La_2O_3 doped γ-alumina is attributed to the stronger basicity of the L a_2O_3 doped alumina support resulting in a stronger and more extensive adsorption of CO_2.

- Boron-free unsupported Co NPs as well as silica-supported Co are also active in CO_2 hydrogenation but produce both CO and methane. In particular, methanation activity is strongly reduced upon time on stream due to the formation of encapsulating carbon species. Instead, the production of CO through the RWGS reaction shows only weak

deactivation and this apparently associated to the activity of unreduced cobalt in the form of CoO and/or Co silicates. Boron impurities fully deactivate Co NPs for methanation. It seems in any case confirmed that Co both unsupported and supported on silica, is not a suitable catalyst for CO_2 methanation.

- Data obtained with cobalt catalyst, suggest that, at least in this case, methanation and RWGS follow two parallel ways, active in different sides. Due to the low activity of Co in methanation, it is also concluded that the formation of methane during ESR, which lowers H_2 selectivity, is due to ethanol cracking more than to methanation.

- Homemade Ni-Al_2O_3 catalyst (with 39% Ni), result to be more active than commercial methane steam reforming catalysts (Ni on Calcium aluminate), both in CO_2 methanation and methane steam reforming. This is mainly attributed to the higher amount of Nickel. It is supposed that the composition of the commercial catalyst is optimized for very long time on stream applications. In any case the data obtained which will be used for kinetic modeling, confirm the validity of micro reversibility principle showing that the catalyst is active in catalyzing an equilibrium starting from both sides.

List of publications on ISI Journals:

1. **Cavattoni ,T**.; Garbarino, G.; Catalytic abatement of biomass tar: a technological perspective of Ni-based catalysts, ***Rendiconti Lincei*** *2017*, **28**; 68-85;
2. Garbarino G., Wang C., **Cavattoni T.**, Finocchio E., Riani P., Flytzani-Stephanopoulos M., Busca G.:A study of Ni/La-Al_2O_3 catalysts: a competitive system for CO_2 Methanation; ***Applied Cat. B: Environmental***, in press.
3. Garbarino G., **Cavattoni T**., Riani P., Brescia R., Canepa F., Busca G.: Nickel-Cobalt alloy nanoparticles: effect of preparation procedure in the catalytic activity in ethanol steam reforming; submitted to ***Molecular Catalysis.***
4. **Cavattoni T**., Garbarino G., Riani P., Busca G.: Deactivation and selectivity switches during CO_2 methanation and Ethanol Steam reforming over Co/SiO_2 catalysts; submitted to ***Applied Catalysis B: Environmental.***
5. Garbarino G., Pugliese F., **Cavattoni T**., Riani P., Busca G., Costamagna P.: Methane steam reforming and CO_2 methanation over commercial nickel/calcium aluminate catalysts: experimental study and laboratory reactor modelling; in preparation, to be submitted to ***Chemical Engineering Journa***l

Communications at Conferences

- **T. Cavattoni**, G. Garbarino, G. Busca, F. Canepa, P. Riani, «Mono- and bimetallic nanoparticles as catalysts in ethanol steam reforming», **(O)** Giornata della Chimica Ligure 2017: Le attuali tendenze della ricerca chimica in Liguria, 20 ottobre 2017, Genova.
- G. Garbarino, **T. Cavattoni**, F. Canepa, Brescia R., G. Busca, P. Riani; "Co and (Co, Ni) Nanoparticles: effect of preparation procedure on catalytic activity in ethanol steam reforming and CO_2 methanation"; **(O)** XI INSTM Conference, Luglio 12-15 2017, Ischia (NA)
- Co/SiO_2 based catalysts: effect of preparation procedure on catalytic activity in ethanol steam reforming and CO_2 methanation. G. Garbarino, **T. Cavattoni**, P. Riani, G. Busca; **(P)** XI INSTM Conference, Luglio 12-15 2017, Ischia (NA)
- Metal based nanoparticles as heterogeneous catalysts, **T. Cavattoni**, G. Garbarino, F. Canepa, G. Busca, P. Riani, "Programma PhD: La formazione post lauream e il mondo del lavoro - Nell'Industria Chimica, chi fa Ricerca… fa Carriera?" **(P)** Workshop FEDERCHIMICA, 24 Maggio 2017, Genova
- Co and Ni Mono- and bimetallic nanoparticles for catalysis applications, **T. Cavattoni**, G. Garbarino, R. Brescia, P. Riani, F. Canepa, G. Busca; **(P)** Europacat, 13° European Congress on Catalysis, 27-31 Agosto 2017, Firenze

- Methane Steam Reforming and CO_2 methanation over commercial Nickel/Calcium Aluminate catalysts: experimental study and laboratory reactor modelling, G. Garbarino, F. Pugliese, **T. Cavattoni**, P. Riani, G. Busca, P. Costamagna; **(P)** International Conference on Chemical Reaction Engineering, P263, Firenze 20-23 Maggio 2018.

Appendix – Characterization Techniques

a.1 xRay Diffraction on powders samples

X-ray diffraction (XRD) is a method based on elastic scattering of X-ray radiation from target materials. This kind of scattering take place when the analyzed sample has a long-range organized structure that may interact with the X-ray's wavelength, having the same order of magnitude (10^{-3} nm < λ < 1 nm). The radiation focused on crystalline samples interacts with the atoms generating a new series of waves characterized by the same energy of the incident beam. The outgoing waves may interact between themselves and, depending on the optical path and then on the atom's distance, it will be possible observe high intensity of the diffracted radiation just on particular directions. This effect may be described with the Bragg equation, considering the X-ray reflection on the lattice planes (Fig. a.1). In this example the constructive interaction between the arising waves, is obtained just if the path of the radiations is:

$$2d_{hkl}\sin\vartheta = n\lambda$$

Where d_{hkl} represent the distance between the crystal's planes; *hkl* are the Miller's indexes of the considered planes and ϑ is the angle of incidence of the incoming radiation. With this equation it is possible to correlate the distance between the planes generating a particular reflection with the angle at which we observe diffraction peaks.

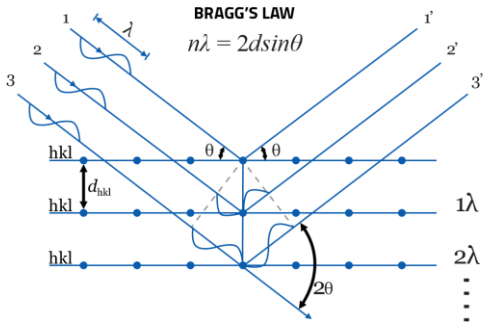

Fig. a.1

In particular, X-ray diffraction pattern from powder samples have been collected using a θ-2θ Bragg-Brentano diffractometer (Fig. a.2).

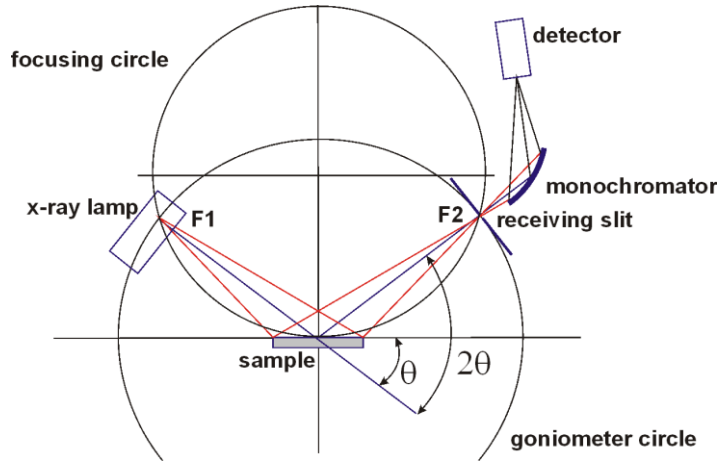

Fig. a.2

In this configuration, the sample holder is in the center of the goniometric circle and rotates around the axis perpendicular to the direction of the beam. This rotation, combined with both X-ray source and detector's rotations allows the inspection and the collection of all the diffraction peaks.

a.2 Infrared Spectroscopy.

Infrared spectroscopy is a technique based on the vibrations of the atoms of a molecule. An infrared spectrum is collected using an infrared radiation and checking how much of the incident energy is absorbed at a certain wavenumber, that correspond to a certain energy. This energy could be directly related to a vibration frequency of a part of the molecule took in consideration. Infrared spectroscopy has the following selection rule: an electric dipole moment of the molecule must change during the vibration to have an infrared absorption. It is easy to understand, with this selection rule, that the interactions of infrared radiation with matter can be explained in terms of changes in molecular dipoles associated with vibrations and rotations. One of the easiest model is to think to a molecule made up as a system of masses joined by bonds with spring-like properties. The easiest example is a diatomic molecules, that have three degrees of translational freedom and two degrees of rotational freedom. The atoms of the molecules can also move relative one to the other, that is, bond lengths can vary or one atom can move out of its present plane. This is a description of stretching and bending movements. For a diatomic molecule, only one vibration that corresponds to the stretching and compression of the bond is possible. This accounts for one degree

of vibrational freedom. Polyatomic molecules containing many (N) atoms will have 3N degrees of freedom as schematized in Table a.1.

Table a.1

Type of degrees of freedom	Linear	Non-linear
Translational	3	3
Rotational	2	3
Vibrational	$3N-5$	$3N-6$
Total	$3N$	$3N$

Fourier-transform infrared (FTIR) spectroscopy is based on the idea of the interference of radiation between two beams giving an interferogram. The latter is a signal produced as a function of the change of path length between the two beams. The two domains of distance and frequency are interconvertible by the mathematical method of Fourier-transformation. The radiation merging from the source passes through an interferometer and then to the sample before going to the detector. After an amplification of the signal and the elimination of the high- frequency contribution by a filter, the data are converted in a digital form and then transferred to the computer for Fourier-transformation.

Infrared spectroscopy is an extremely versatile technique so we can analyze, liquids, solids and gases; moreover in the heterogeneous catalysis field it is extremely important for the following characterization:

- to know the catalysts properties and in particular the framework vibration, surface species, acidity, oxidation state of the ion, metal dispersion
- definition of the interactions between the sorbent and the catalysts and particularly the properties of the surface groups, adsorption of acid or basic molecules, adsorption of reagent and products, intermediate species and modification of the oxidation state.

In order to carry out the analysis, the material is assembled as a self-supported disk. Depending on the analysis that has to be done, two different preparation are available: the first one is the dilution of the catalyst in a material that is transparent to the IR window, as those reported in Table a.2. The latter one consists in the preparation of a pure powder thin disk that diffuses a little of the radiation and possesses a good transmission to IR, with good mechanical properties.

Table a.2

Window material	Useful range (cm^{-1})	Refractive index	Properties
NaCl	40 000–600	1.5	Soluble in water; slightly soluble in alcohol; low cost; fair resistance to mechanical and thermal shock; easily polished
KBr	43 500–400	1.5	Soluble in water and alcohol; slightly soluble in ether; hygroscopic; good resistance to mechanical and thermal shock
CaF_2	77 000–900	1.4	Insoluble in water; resists most acids and bases; does not fog; useful for high-pressure work
BaF_2	66 666–800	1.5	Insoluble in water; soluble in acids and NH_4Cl; does not fog; sensitive to thermal and mechanical shock
KCl	33 000–400	1.5	Similar properties to NaCl but less soluble; hygroscopic
CsBr	42 000–250	1.7	Soluble in water and acids; hygroscopic
CsI	42 000–200	1.7	Soluble in water and alcohol; hygroscopic

The position of metal-oxygen stretching bands depends on the nature of M-O bond (more is covalent, higher will be the stretching frequency) and on the weight of the metal atom (heavier, lower the stretching frequency). Metal oxygen bond are weaker than the corresponding bulk bond and some feature can be observed in the spectra of pressed disks of metal oxides, just above or near the cut-off due to bulk vibrations. In KBr, bulk vibrations will be detected in the region 1600 cm^{-1}-400 cm^{-1}. The surface properties of a catalyst can be studied observing the IR spectrum of internal probe molecules, such as hydroxyl groups (-OH). In many other cases, we need external probe molecules in order to identify these sites, because the adsorption of a probe molecule on these sites induces a wavenumber variation, which can be related with the nature of the sites. This method is used to study the acidity of a material (Lewis and Brønsted acid sites) and the surface properties of metal particles.

a.3 UV-vis-NIR (Ultraviolet, Visible and Near Infrared Spectroscopy)

As all the spectroscopies, UV-Vis spectroscopy is based on the absorption of a particular wavelength from a sample due to the interaction between the incoming radiation and the energetic level characteristics of the absorbing species. The absorption bands occurring in the visible and near

ultraviolet region gives information on the electronic structure of a heterogeneous catalyst. The observed bands are related to different transitions between the electronic levels of the atoms, complexes, ion or molecules. In the study of catalysts and oxides, this technique is commonly used in diffuse reflectance. The molecular spectra are characterized by absorption bands with a wide wavelength range; for each state a large number of rotational and vibrational energy states exist, thus for each electronic state there are different energy values (E) that differ in small variation in rotational o vibrational energy as reported in Figure a.3.

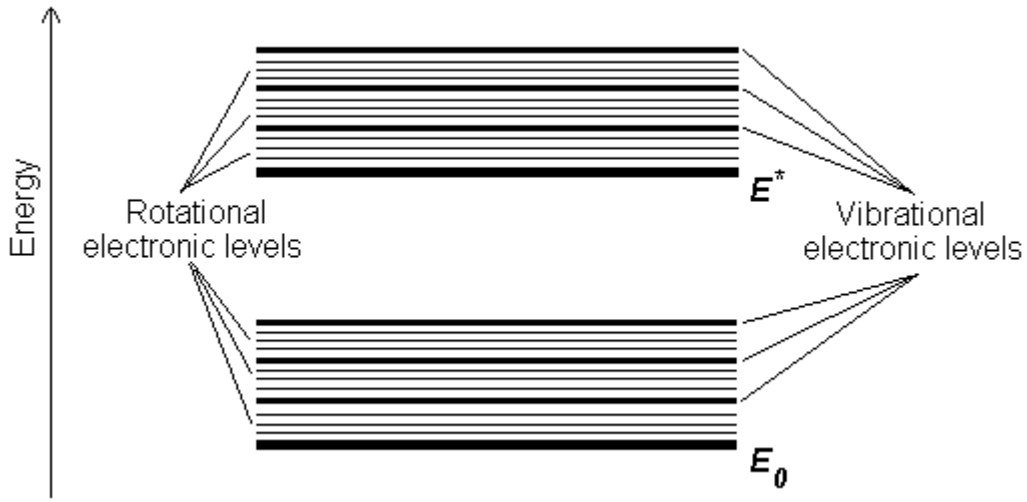

Fig. a.3

This technique could be operated in transmission (for liquid, gases or transparent solids) or, as in the case of heterogeneous catalysts, in reflectance. In particular the radiation reflected from a crystalline powder is formed by two components: the former one is the reflected radiation without transmission, the latter one is the diffuse component, absorbed by the material, that reappears at the surface of the sample after multiple scattering. The commercial spectrophotometers reduces the former component and, using an integrating sphere, maximize the signal of the diffused component that is weaker than the incident beam. This sphere is coated with a high reflecting layer, like MgO or $BaSO_4$ that reflects the diffuse light allowing the collection of a greater percentage of the diffuse radiation. Three different electronic transition should be taken into account;

i. d-d transitions of transition metal complexes. The transition metal ions are characterized by a configuration 3dn or 4dn or 5dn. These orbitals are partially occupied so the incident beam allows the transitions of an electron from a d orbital to another. The energy of this transition

is a function of the symmetry of the complex, of the valence of the central metal of the nature of the ligand. These transitions are found in the UV range and more often in the visible part of the spectrum, and are responsible for the colors of many transition metal complexes.

ii. Charge transfer. In this case, an electron transfers from an occupied orbital of a donor to an unoccupied orbital of an acceptor for organic molecules. In inorganic chemistry charge transfer happens when there is a transfer of an electron from an orbital mainly localized on the metal to an orbital mainly localized on the ligand (M→ L), or a transfer in the opposite direction (L → M). The absorption band that results from this transition is usually at higher energy than those of d-d transition, so they are found mainly in the ultraviolet region of the spectrum.

iii. Electronic transitions across the forbidden energy gap like TiO_2 and ZrO_2, with absorption bands in the UV region.

iv. Absorption in the visible region: promotion of the electrons of the same atom from low energy orbital to those at higher energy.

v. π→π* and n→π * transitions. These involve respectively jump of π or n electrons between the molecular orbital of organic molecules. These transitions occurs in the UV range.

a.4 Scanning Electron Microscopy and Energy-dispersive X-ray spectroscopy

The Scanning Electron Microscopy (SEM) equipped with an Energy Dispersive X-ray Spectrometer is a very important and useful technique that allows the direct observation of the sample and the evaluation of its chemical composition.

Being an electron microscopy, this technique is based on the interaction between an electron beam and the sample; the use of this kind of beam enable to achieve a much higher resolution than that obtainable with other techniques.

In SEM instruments, the electron beam is generated by thermionic effects or, as in our case, by field emission guns. The Field Emission SEM, where a field emission gun is adopted, presents different advantages respect the thermionic source, mainly related to the stability and brightness of the produced beam. The electron beam generated, passes through the optical column where it

is narrowed and focused on the sample. In the following Fig. a.4, a schematic view of a FE-SEM is represented.

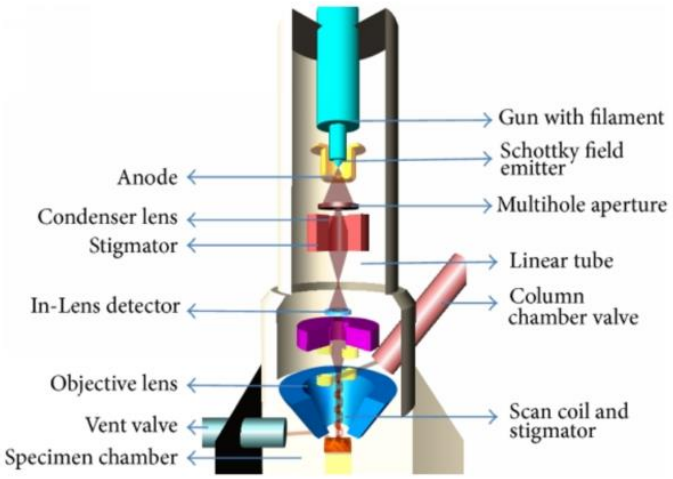

Fig. a.4

The interaction between the electron beam and the sample generates different kind of signals, as shown in Fig. a.5 but two of them are the most important to obtain different information about the sample: Backscattered electrons (BSE) and secondary electrons (SE).

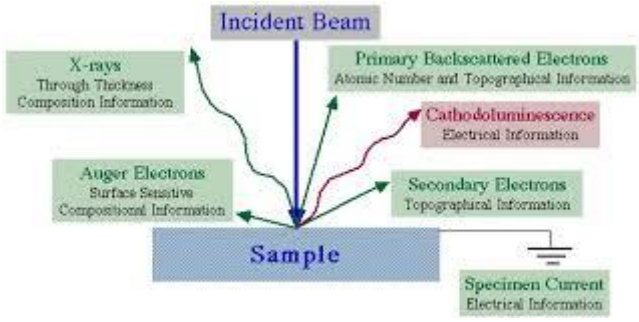

Fig. a.5

The Backscattered electrons signal is generated when the incident beam strikes the target sample and then a series of elastic scattering happens inside the sample itself. Finally, a percentage of the incident electrons, about the 30% of incident beam, arises from the surface and can be detected. The signal generated by the BSE allows obtaining compositional contrast since the number of the backscattered electrons reflected is strongly related to the atomic number of the sample.

Secondary electrons are generated instead by inelastic scattering phenomena. In fact, when an electron hits the sample, also inelastic scatter can have place and electrons of the sample itself may be ejected. The signal generated is a low energy electrons signal, due to weakly bounded conduction or outer valence shell electrons, and present a narrow peak distribution at very low energy, lower than 50 eV. Since their low-energy value, these electrons are emitted only if it happens close to the surface of the sample; therefore the signal obtained will be strongly related to the morphology of the sample itself.

Signals detection requires different and specific detectors (Fig.a.5); high energy BSE are mainly collected throughout a solid-state detector, collocated usually at the exit of the optical column, low energy SE detection present instead different possibility. The most common detector for this signal capture is a detector directly placed in the sample chamber, named Everhart-Thornley detector, a combination of a scintillator and a photomultiplier with a Faraday cage acting as a filter; in fact its potential controls the fraction of electrons that will be detected. However, this detector is affected by different problems: it is impossible to remove the contribution arising from BSE emitted by the sample, and furthermore SE generated by the interaction between BSE and the walls of the chamber can be detected as well. So, to obtain a cleaner SE signal, and then a higher resolution of the morphology of the sample, it might be used an In-Lens detector. This kind of detector is placed inside the optical column, thus it is needed to force the SE signal in that direction. This is possible due to electromagnetic lenses, snorkeling lenses, which focus the signal coming from the sample's surface to the detector. It is noteworthy that the use of In-Lens detector needs a very low working distance, i.e. distance between the exit of the optical column and the sample. This is a limitation since it does not allow using simultaneously the In-Lens detection and the EDX analysis

Another very powerful technique coupled with a scanning electron microscope, is the Energy-dispersive X-ray spectroscopy (EDX). This kind of technique allows both qualitative and quantitative analysis of a sample. In fact the high energy beam can create vacancies in the inner atom's levels. Those vacancies are filled by the outer levels electrons, followed by the emission of element's characteristic x-ray radiation that, according to Mosely's law, allows the qualitative analysis and, subsequently, the qualitative ones.

The FE-SEM and EDX analysis have been carried out on all the samples tested, since it allows to investigate directly both the particles dimension and morphology. The typical sample preparation depends on the nature of the sample itself. The fresh metal catalysts have been characterized by

dispersion of the powder in an appropriate solvent, followed by ultrasonic sonication, then few drops were dropped on the support. For what concern the supported catalysts, the sample was collected on an aluminum stab, stuck through a conductive adhesive tape, in order to obtain a good image.

a.5 Adsorption and desorption of N_2

Specific Surface Area (SSA) is defined as the external surface of a solid available for the interaction with the environment. This parameter is particularly important from technologic applications since it gives an idea of the number of available active sites on the surface of a sample.

A convenient way to determine the Specific Surface Area of a sample is based on the adsorption of gases on the surface. The adsorption is brought about by the forces acting between the solid and the molecules of the gas. These forces are of two main kind -physical and chemical- and they give rise to physical (or Van der Waals) adsorption and chemisorption, respectively. It is convenient to note that the physical forces are the same nature as the Van der Waals forces bringing about the condensation of a vapor to the liquid state.

The quantity of gas taken up by a sample of solid is proportional to the mass *m* of the sample and it depends also, on the temperature *T*, the pressure *p* of the vapor and the nature of both the solid and the gas. If *n* is the quantity of gas adsorbed expressed in moles per gram of solid:

$$n=f(p,T,gas,solid)$$

For a given gas adsorbed on a particular solid maintained at a fixed temperature, below the critical temperature of the gas, we can rewrite the equation as:

$$n=(p/p_0)_{T,gas,solid}$$

being p_0 the saturation vapor pressure of the adsorptive. This last equation is expression of the adsorption isotherm, i.e. the relationship, at constant temperature, between the amount of gas adsorbed and the pressure, or relative pressure, respectively.

Gas adsorption is the most used techniques to evaluate the specific surface area and the pore size distribution. Among the different parameters useful to define the morphology of a material, in particular of a catalyst, we have:

- Specific surface area: surface for unit of material mass [m^2/g]
- Specific pore volume: volume of the pores for unit of mass [ml/g]
- Pore diameter: this represent the diameter of the transversal section of each pore, making the approximation of a cylindrical pore that behaves, for catalytic effect, in the same way as the real pore.

The description of the catalyst pore structure is obtained making the distribution of pore size that evaluate the pore volume for each pore diameter. The pore size could be classifies in different families in function of the diameters [1]:

Micropores 0-2 nm

Mesopores 2-50 nm

Macropores 50 nm

In order to obtain this pore size distribution, we do the adsorption desorption isotherm of N_2 at 78 K (nitrogen boiling point). In this way, we obtain the volume of adsorbed nitrogen for unit of mass at the equilibrium pressure, normally given as relative pressure P/P_0, where P_0 is the saturation pressure of N_2 at 78 K. The amount of adsorbed gas at the equilibrium pressure P is given by the difference between the initial amount of N_2 and the required amount to fill a part of the pore volume of the material. This isotherm is obtained point by point adding doses of gas to the material and measuring the N_2 adsorbed amount with the help of a volumetric or gravimetric technique. In order to have a correct analysis of the pore volume, the material is pretreated in temperature (473 K in vacuum), in order to desorb the species eventually present. This mild temperature allows us to avoid modification of the surface area of the samples. The first obtainable value is surface area following the Brunauer- Emmett and Teller method (BET); this consist in an estimate of the nitrogen volume necessary to have a monolayer of adsorbed nitrogen (Vm). This equation is valid in the P/P_0 range between 0.05 and 0.35. In reality during the development of the present work were used two method of extimation of the surface area and in particular the Single Point method and the Multipoint Method. It is easy to understand that the two methods differ each other for the number of points taken to get the surface area value [2]. The single point method, easy to be carried out, allows the calculation of the surface area from the following equation a.1

$$S_{BET} = \left(1 - \frac{p}{p_0}\right)\frac{N_A}{M}A \qquad \text{Equation a.1}$$

Where:

P is the equilibrium pressure [kPa]

P_0 is the vapor pressure of N_2 at its boiling temperature [kPa]

M molecular weight [g/mol]

N_A Avogadro's number [molecules/mol]

A cross sectional area of the adsorbed molecule (for N_2 A=0.162 nm^2) [nm^2]

The multipoint method allows an evaluation of the BET taking, as suggested by the name, three or four point of the adsorbed volume in the P/P_0 validity range. In this case the unsimplyfied BET equation is used [3]

$$\frac{1}{W\left(\frac{P_0}{P}-1\right)} = \frac{1}{W_m C} + \frac{C-1}{W_m C}\frac{P}{P_0} \qquad \text{Equation a.2}$$

Where

P is the equilibrium pressure [kPa]

P_0 is the vapor pressure of N_2 at its boiling temperature [kPa]

W weight adsorbed [g]

W_m weight adsorbed in a complete monolayer [g]

C is the kinetic constant that in a BET plot represents the intercept in the y axis (W/W_m).

It is important to underline that from a complete adsorption-desorption isotherm different information could be obtained. The adsorption or desorption branches of the isotherm give the pore size distribution while the closing point of the hysteresis gives the total pore volume, as the volume of nitrogen adsorbed. Moreover, the hysteresis suggests the shape of the pores as reported in Figure a.6.

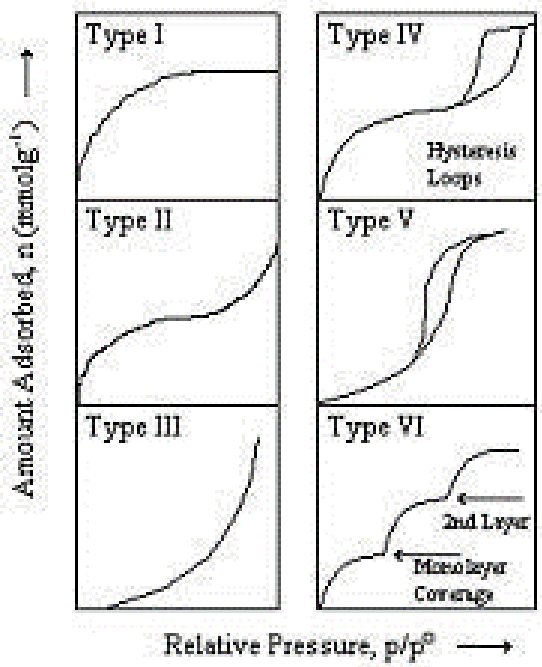

Fig. a.6 - Types of isotherms hysteresis

a.6) H_2-TPR Hydrogen Temperature Programmed Reduction

Temperature programmed reduction tests were used to evaluate the reducibility of metal oxides, mixed metal oxides and also metal oxides dispersed on the support. In this particular case Temperature Programmed Reduction tests (TPR) are used to identify and evaluate the reducibility of nickel species present on the alumina supported catalysts. In a typical H_2-TPR test, the as-calcined catalyst is first purged with helium at 523 K for 30 minutes, and then reduced by a H_2 gas mixture (normally Ar) while the temperature is ramped up from RT to the desired final value at a fixed rate. The TPR method could give a quantitative result if the TCD signal is calibrated so is obtainable the hydrogen consumption of the catalyst surface, as well as its high sensitivity to chemical changes resulting from promoters or metal/support interactions. Therefore, the TPR method is also suitable for quality control of different catalyst charges since deviations in manufacturing methods often result in different reduction profiles. In cyclic TPR-TPO, upon a first reduction, the sample is cooled down to room temperature in helium and then oxidized in a 20% O_2/He gas mixture. The subsequent TPR cycle is conducted following the same procedure.

a.7) X-ray Photoelectron Spectroscopy (XPS)

X-ray photoelectron spectroscopy (XPS) is a particular photoemission spectroscopy where X-rays are used to obtain the chemical composition of the surface region of a material. The goal of photoemission spectroscopy is to determine the kinetic energy of the wavevector of the emitted electrons. This is related to the high probability for the ejection of a core electron into an unbound state if a photon with an energy higher than the binding energy of that electron is absorbed. The kinetic energies of these directly produced photoelectrons can be measured, and give direct information on the sample.

The possibility to produce a photoelectron is strictly related to the energy of the incoming radiation. If the radiation is in the ultraviolet or soft X-ray range, core level electrons can not be ejected; on the other hand, the energy is sufficient to eject valence electrons from bounds states. Elemental and chemical analysis is mainly carried out with energetic X-ray by probing photoelectrons originating from core levels and typically spans the energy range of few hundred to one or two thousands eV. XPS reveals chemical information of the surface region down to a fraction of percent.

XPS spectra are obtained by irradiating a material with a beam of X-rays while simultaneously measuring the kinetic energy and number of electrons that escape from the top 0 to 10 nm of the material being analyzed. XPS requires high vacuum ($P \sim 10^{-8}$ millibar) or ultra-high vacuum (UHV; $P < 10^{-9}$ millibar) conditions

Because the energy of an X-ray with particular wavelength is known, and because the emitted electrons' kinetic energies are measured, the electron binding energy of each of the emitted electrons can be determined by using an equation that is based on the work of Ernest Rutherford (1914):

$$E_{binding} = E_{photon} - (E_{kinetic} + \phi) \qquad \text{Equation a.3}$$

where E_{binding} is the binding energy of the electron, E_{photon} is the energy of the X-ray photons being used, E_{kinetic} is the kinetic energy of the electron as measured by the instrument and ϕ is the work function dependent on both the spectrometer and the material. The work function term ϕ is an adjustable instrumental correction factor that accounts for the few eV of kinetic energy given up

by the photoelectron as it becomes absorbed by the instrument's detector. It is a constant that rarely needs to be adjusted in practice.

Each element produces a characteristic set of XPS peaks at characteristic binding energy values that directly identify each element that exists in or on the surface of the material being analyzed. These characteristic spectral peaks correspond to the electron configuration of the electrons within the atoms, e.g., 1*s*, 2*s*, 2*p*, 3*s*, etc. The number of detected electrons in each of the characteristic peaks is directly related to the amount of element within the XPS sampling volume. To generate atomic percentage values, each raw XPS signal must be corrected by dividing its signal intensity (number of electrons detected) by a "relative sensitivity factor" (RSF), and normalized over all of the elements detected.

a.8) Gascromatography and mass spectrometry analysis (GC-MS)

GC-MS analysis were carried out with a Thermo Focus GC, with capillary column TC-SQC (30m 0.25 mm x 0.25 μm), coupled with a mass spectrometer ISQ (Fig. a.7), consisting in 3 parts, ionic source (ionization chamber), analyzer and a detector.

Fig. a.7 – Gascromatographer and mass spectrometer

The sample (50 μl) is manually injected with a syringe in a cylindrical chamber where, due to the high temperature (500-600K) the compounds are vaporized. La gaseous mixture is then transferred to the column by the carrier gas flux. The spectrometer is connected to the gas cromatographer through a transfer line inside the GC column.

The ionization chamber, as well as the other spectrometer parts, is under high vacuum (about 0.04 mbar), vacuum obtained through a turbomolecular pump coupled with the analyzer.

The gases enter the ionization chamber thanks to the pressure drop, inside the chamber electrons are generated by thermoionic effect (E ≈ 70eV). About 10 eV are enough to ionize the neutral species in the sample, the remaining energy will fragmentize the ionized specimens.

The ionized gas pass through an electric field generated from charged plates where ions are accelerated and pushed to the detector (Fig a.8).

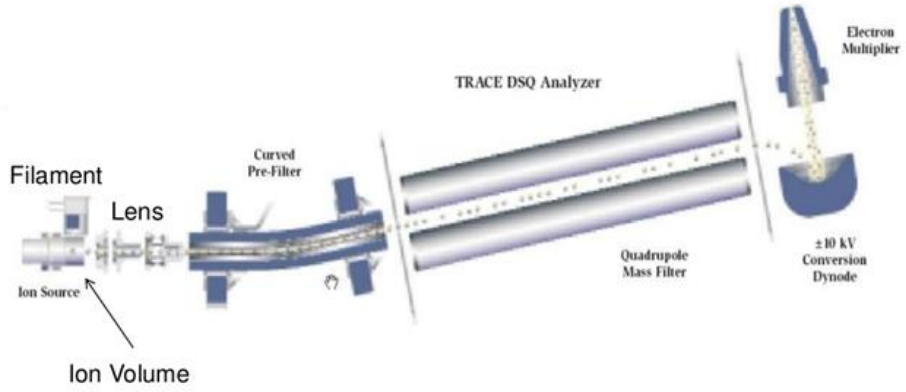

Fig. a.8 – Mass Spectrometer scheme.

Quadrupole magnetic detector consist in four steel cylindrical bars coupled with a electric generator. Ions coming out from the source and then accelerated enter in the detector where they are separated by the ion mass. Each ion is associated by a m/z ratio, for every electronic potential/radiofrequency assumed from the detector. Changing potential and radiofrequency different m/z will be detected.

a.9) References

[1] K. S. W. Sing, D. H. Everett, R. Haul, L. Moscou, R. A. Perotti, J. Rouquerol and T. Siemieniewska, Pure Appl. Chem., 1985, 57, 603
[2] S. Brunauer, P. H. Emmett and E. Teller, J. Am. Chem. Soc., 1938, 60, 309
[3] S. Lowell. Powder Sutface Area, John Wiley and Sons, 1979